Technische Universität München
TUM School of Engineering and Design

Enhancing composite crushing prediction with strain-rate-dependent numerical models

Christian Dieter Pohl

Vollständiger Abdruck der von der TUM School of Engineering and Design der Technischen Universität München zur Erlangung eines

Doktors der Ingenieurwissenschaften (Dr.-Ing.)

genehmigten Dissertation.

Vorsitz:

Prof. Dr.-Ing. Karsten Stahl

Prüfer der Dissertation:

1. Prof. Dr.-Ing. Klaus Drechsler
2. Prof. Dr. Giuseppe Catalanotti

Die Dissertation wurde am 28.11.2023 bei der Technischen Universität München eingereicht und durch die TUM School of Engineering and Design am 08.04.2024 angenommen.

Technische Universität München
TUM School of Engineering and Design
Lehrstuhl für Carbon Composites
Boltzmannstraße 15
D-85748 Garching bei München

Tel.: + 49 (0) 89 / 289 - 15092
Fax: + 49 (0) 89 / 289 - 15097
Email: info.lcc@ed.tum.de
Web: www.asg.ed.tum.de/lcc

Acknowledgement

I want to thank all those who have enriched this academic project and made the achievement of this thesis a reality. My special thank you goes to:

- Prof. Klaus Drechsler and Swen Zaremba for giving me the opportunity to conduct high-level scientific research at the Chair of Carbon Composites, for the inspiring discussions and their constant support throughout my thesis.
- Prof. Giuseppe Catalanotti from the Kore University of Enna for acting as the second examiner.
- Prof. Nik Petrinic and his (former) research associates for the great hospitality and guidance during my research stay at the University of Oxford.
- The German Federal Ministry for Economic Affairs and Climate Action for providing funding within the LuFo project CraCpit (grant number 20E1703B).
- The whole team of Akaflieg Munich and all CraCpit students, in particular Roberto Fillbrandt, Clemens Lippmann, Florian Kloiber, Marvin Hofmann, and Joscha Loewe for their commitment to an intense collaboration, which made our project a great success.
- My four group leaders, Hannes Koerber, Luciano Avila Gray, David Colin, and Dennis Bublitz, for the regular feedback talks and supervision of my scientific actions.
- Dennis Bublitz and Marco Toenjes, for being or becoming my academic sparring partners - and for the proofreading efforts they contributed to this work.
- Marina Ploeckl, for mentoring my research activities and being an academic door-opener.
- My office partners in crime, Dominik Boos and Weili Jiang, for the "dissolute" time ("liederliche" Zeit) in our kitchen office.
- All former and recent staff members of the Chair of Carbon Composites for the exchange, help, and excellent atmosphere in the office, lab, and workshop.
- My brother Michael and his family, my parents Ruth and Dieter, and my girlfriend Lidia: you provided me with the loving and constant backing I needed to pursue this goal for such a long time.

Since all models are wrong the scientist must be alert to what is importantly wrong. It is inappropriate to be concerned about mice when there are tigers abroad.

George Box [1]

Abstract

Fiber-reinforced plastics under crushing failure yield the highest energy absorption capacities per mass of any known engineering material. Crushing refers to axial or off-axis loading of fixed cross-sectional or tapered composite structures. Due to the significance of crushing failure, it has been thoroughly investigated experimentally and numerically in numerous studies. However, the failure process has proven to be notoriously difficult to simulate due to the multitude of failure mechanisms and material properties involved. In particular, the effect of strain rates on composite crushing simulations has yet to be considered in the literature, although most crushing structures are exposed to highly dynamic loading scenarios.

This doctoral thesis aims to improve the prediction of composite crushing using numerical models. Therefore, studies of the compressive failure behavior in specimens with increasing complexity manufactured from the well-studied carbon fiber/epoxy material IM7/8552 were conducted. Based on a property database of the material, the intra- and interlaminar failure behavior was studied. Subsequently, open-hole compression specimens, flat crushing coupons, and crushing tubes were tested, or the results were taken from the literature. The experiments were conducted under two strain rate regimes each: quasi-static experiments and experiments under a high loading rate.

Finite-element shell models of the tested geometries were created in LS-DYNA with different through-thickness discretization to complement the experimental investigations: single-shell, stacked-laminate, and discrete-ply models. Delamination interfaces were introduced as cohesive zone elements or eroding contacts if applicable. A novel framework was used to physically motivate the intralaminar material model. In addition, the selected intra- and interlaminar material models facilitated the consideration of strain rate sensitivities. Additional simulation studies were conducted to quantify parameter influences and numerical effects.

All experimental results show a high replicability and can be applied to validate the numerical models. The predictive quality of stacked-laminate and discrete-ply models is excellent for the open-hole coupons. In contrast, it decreases over the coupon crushing models toward the crushing tube models. This reduction can be attributed to the element erosion scheme, a non-sufficient model discretization in the through-thickness direction, and the lack of a plasticity formulation in the applied intralaminar material model. The shape of the element softening law also shows considerable influence on the results. The coupon crushing studies suggest that rate-induced increases of intralaminar properties provoke excessive delaminations, leading to premature buckling and thus reducing the crushing stress under high

loading rates. Furthermore, numerically adapted interlaminar strength values are not applicable in full-scale crushing problems using coarsely meshed discrete-ply models. However, stacked-laminate models can partly replicate the failure behavior of the crushing tubes in a runtime-efficient way.

Further experimental research of composite behavior under strain rates higher than 5,000 1/s and numerical studies with material models considering plastic deformation are suggested. In conclusion, the significance of rate dependencies in composite crushing is demonstrated by validating a numerical sailplane model against experimental data from a full-scale crash test.

Kurzfassung

Faserverstärkte Kunststoffe weisen bei Versagen im Crushingmodus die höchste spezifische Energieabsorption aller bekannten technischen Materialien auf. Unter Crushing versteht man das Versagen von Faserverbundstrukturen mit konstantem oder sich verjüngendem Querschnitts unter axial oder schräg einwirkender Belastung. Aufgrund der technischen Bedeutung des Crushings wurde es in zahlreichen Studien experimentell und numerisch eingehend untersucht. Allerdings erwies sich der Versagensprozess infolge der Vielzahl beteiligter Mechanismen und Materialeigenschaften als äußerst schwierig zu simulieren. Insbesondere der Einfluss von Dehnraten in Crushingsimulationen von Composites muss in der Literatur erst noch Berücksichtigung finden, obwohl die meisten Crushingstrukturen hochdynamischen Belastungsszenarien ausgesetzt sind.

Ziel dieser Doktorarbeit ist es, die Vorhersage des Crushings mithilfe numerischer Modelle zu verbessern. Daher wurden Untersuchungen zum Verhalten von Proben unter Drucklasten mit zunehmender Komplexität durchgeführt. Die Prüfkörper wurden dafür aus dem in der Fachliteratur umfassend charakterisierten Kohlenstofffaser-Epoxidmaterial IM7/8552 hergestellt. Basierend auf einer Materialdatenbank wurde das intra- und interlaminare Versagensverhalten untersucht. Anschließend wurden gelochte Flachproben, flache Crushingproben und Crushingrohre getestet oder vorhandene Ergebnisse der Literatur entnommen. Die Experimente wurden jeweils unter zwei Dehnraten durchgeführt: quasistatisch und mit hochdynamischer Lastaufbringung.

Zur Ergänzung der experimentellen Untersuchungen wurden in LS-DYNA Finite-Elemente-Schalenmodelle der getesteten Geometrien mit unterschiedlicher Diskretisierung in Dickenrichtung erstellt: Einzelschalenmodelle, Modelle aus geschichteten Laminaten und Modelle mit einer Schale pro Lage. Wenn nötig wurden Delaminationsschichten in Form von Kohäsivzonenelementen oder Kontakten mit Versagensdefinition eingeführt. Um das intralaminare Materialmodell physikalisch zu motivieren, wurde ein neuartiges numerisches Vorgehen gewählt. Darüber hinaus ermöglichten die verwendeten intra- und interlaminaren Materialmodelle die Berücksichtigung von Dehnrateneinflüssen. Zusätzliche Simulationsstudien wurden durchgeführt, um Parametereinflüsse sowie numerische Effekte zu quantifizieren.

Alle experimentellen Ergebnisse zeigen eine hohe Reproduzierbarkeit und können zur Validierung der numerischen Modelle herangezogen werden. Die Vorhersagegüte von geschichteten Laminatmodellen und Modellen mit einer Schale pro Laminatschicht ist für die gelochten Coupons hervorragend. Hingegen nimmt die Prognosequalität über die Coupon-Crushingmodelle hin zu den Modellen der Crushingrohre ab. Diese

Reduktion kann auf das numerische Vorgehen beim Löschen von Elementen, eine unzureichende Modelldiskretisierung in Dickenrichtung und das Fehlen einer Plastizitätsformulierung im verwendeten intralaminaren Materialmodell zurückgeführt werden. Auch die Art des Lastabfalls in der Charakteristik des Materialmodells zeigt erheblichen Einfluss auf die Ergebnisse. Die Studien zum Crushing von Coupons lassen darauf schließen, dass geschwindigkeitsbedingte Erhöhungen der intralaminaren Eigenschaften übermäßige Delaminationen hervorrufen, die zu vorzeitigem Beulen führen und somit die Crushingspannung bei hohen Belastungsgeschwindigkeiten verringern. Darüber hinaus sind numerisch angepasste interlaminare Festigkeitswerte bei großskaligen Crushingproben unter Verwendung grob vernetzter Schalenmodelle nicht anwendbar. Allerdings können geschichtete Laminatmodelle das Versagensverhalten der Crushingrohre teilweise laufzeiteffizient nachbilden.

Weitere experimentelle Untersuchungen des Verhaltens von Faserverbundwerkstoffen bei Dehnraten oberhalb von 5.000 1/s und numerische Studien mit Materialmodellen unter Berücksichtigung plastischer Verformung werden empfohlen. Als Abschluss dieser Arbeit wird die Bedeutung der Geschwindigkeitsabhängigkeiten beim Crushing von Composites durch die Validierung eines numerischen Segelflugzeugmodells anhand experimenteller Daten aus einem Crashtest im Maßstab 1:1 demonstriert.

Contents

Nomenclature

Abbreviations

2D	Two-dimensional
3D	Three-dimensional
AN	Analytical framework
ASTM	American Society for Testing and Materials
BBA	Building block approach
CDM	Continuum damage model
CF	Carbon fiber
CFRP	Carbon fiber-reinforced plastic
CMH-17	Composite Materials Handbook-17
CS	Certification specification
CV	Coefficient of variation
CWG	Crashworthiness Working Group
CZE	Cohesive zone elements
CZM	Cohesive zone model
DCB	Double-cantilever beam
DIC	Digital image correlation
DPM	Discrete-ply model
EASA	European Union Aviation Safety Agency
ENF	End-notched flexure
FE	Finite element
FRP	Fiber-reinforced plastic
FT	Fracture toughness
FVC	Fiber volume content
GF	Glass fiber
GFRP	Glass fiber-reinforced plastic
HPC	High-performance cluster
HR	High (strain) rate
ISO	International Organization for Standardization
LCC	Chair of Carbon Composites
MCS	Mean crushing stress
MCSD	Mean crushing stress deviation
MLPM	Multi-layered-ply model

OHC ..... Open-hole compression
ORNL ..... Oak Ridge National Laboratory
QI ..... Quasi-isotropic
QS ..... Quasi-static
SE ..... Single-element
SEA ..... Specific energy absorption
SLM ..... Stacked-laminate model
SR ..... Strain rate
SSCS ..... Specific sustained crushing stress
SSM ..... Single-shell model
STDV ..... Standard deviation
TTT ..... Triangular through-thickness trigger
TUM ..... Technical University of Munich
UD ..... Unidirectional
UTM ..... Universal testing machine

Greek letters

α_0 ..... [°] ..... Fracture angle
β ..... [-] ..... Mixed-mode ratio
Δ ..... [mm] ..... Processed separation
δ ..... [mm] ..... Displacement
$\dot{\epsilon}_{ij}$ ..... [1/s] ..... True strain rate in ij-direction
ϵ_{ij} ..... [-] ..... True strain in ij-direction
η_T ..... [-] ..... Friction coefficient
ν_{ij} ..... [-] ..... Minor Poisson's ratio in ij-plane
ρ ..... [-] ..... Elastic parameter
σ_{ij} ..... [MPa] .... Stress in ij-direction

Latin letters

a ..... [-] ..... Adjustment parameter
$\boldsymbol{C}$ ..... [MPa] .... Constitutive tensor
C ..... [-] ..... Index for compressive loading
d_{ij} ..... [-] ..... Simplified damage parameter in ij-direction
E_{ii} ..... [MPa] .... Elastic modulus in ii-direction

F	[N]	Force
G_{ij}	[MPa]	Shear modulus in ij-direction
G_{ijc}	[N/mm]	Fracture toughness in ij-direction
K	[-]	Cowper-Symonds regression coefficient
k	$[\frac{\sqrt{mm}}{mm}]$	Correctional unit parameter
K_I	$[\frac{N}{\sqrt{mm^3}}]$	Mode I stress intensity factor
l_{cz}	[mm]	Length of cohesive zone
l_e	[mm]	Element length
n	[-]	Cowper-Symonds regression exponent
N_e	[-]	Number of elements in cohesive zone
S	[MPa]	Interlaminar yield stress under shear loading
S_{ij}	[MPa]	Strength in ij-direction
T	[-]	Index for tensile loading
T	[MPa]	Interlaminar yield stress under tensile loading
t	[mm]	Layer thickness
t_e	[mm]	Cohesive element thickness
$\dot{u}_{ij}$	[mm/s]	Element separation velocity in ij-direction
u_{ij}	[mm]	Element separation in ij-direction

List of figures

List of tables

1 Introduction

1.1 Motivation

Originating from their first applications in the military aerospace industry, fiber-reinforced plastics (FRP) have become the state-of-the-art material in commercial aircraft. This is primarily thanks to the high specific and tunable properties of these composite materials but also due to the improved corrosion and fatigue resistance that can be achieved compared to metals. One particular aeronautic application area of composite structures is the sailplane industry: In 1957, FS-24 Phoenix from Akaflieg Stuttgart became the first sailplane that utilized glass-fiber-reinforced plastics (GFRP) [2]. Since then, sailplane fuselages and wings have become mainly hand-laminated composite structures. Analytical flight-load-based design of these structures is an established methodology among sailplane manufacturers [3, 4]. In addition, a crash loadcase has to be taken into account according to European Union Aviation Safety Agency (EASA) certification specification (CS) 22 [5]. However, the quasi-static loading of the fuselage nose, as designated in CS-22, is insufficient to cover real-world impacts. This shortcoming is due to often deviating loading conditions during an accident and the highly dynamic nature of a sailplane crash. Therefore, LuFo V3 aviation research project CraCpit (**Cra**sh **C**ock**pit**) of the Chair of Carbon Composites (LCC) at the Technical University of Munich (TUM), in collaboration with Akaflieg Munich, investigated novel design methods and loadcase scenarios derived from flight accidents to enhance the crashworthiness of future sailplane generations. On 26 July 2022, a crash test was successfully conducted using a full-scale fuselage designed and manufactured by Akaflieg Munich. Figure 1-1 shows the impact of the sailplane nose during the hardware crash at 45° impact angle and 5° angle of sideslip.

As can be seen, crushing failure of the nose cone section is responsible for the deceleration of the fuselage during the first impact. Crushing refers to the destructive loading of fixed cross-sectional or tapered composite structures – often profiles – in the axial direction or with an off-axis exposure angle. Depending on the applied material constituents and architecture, the process can yield the highest specific energy absorption (SEA) capacities of any known engineering material [6]. It is therefore used in lightweight, crashworthy devices of, e.g., Formula One race car crash cones [7, 8], helicopter structures [9–11], or subfloor structures of commercial airplanes [12, 13]. Progressive crushing failure is characterized by the influence of friction and different micro-scale damage mechanisms such as fiber kinking, fiber fracture, and pull-out, matrix fracture, fiber-matrix debonding, and delamination

(a) (b) (c)

Fig. 1-1 Crushing of the cockpit nose during the CraCpit crash test (a) 0 ms, (b) 19 ms, and (c) 38 ms after the initial impact. Lateral view onto the cockpit with rope suspension, substitute masses, and dummy.

[14]. On the macro-scale, splaying and fragmentation failure can be observed. Splaying is characterized by destructive lamina bending, whereas fragmentation is driven by out-of-plane shear failure [15, 16]. Often, a combination of the two failure modes can be observed. Figure 1-2 represents the different damage mechanisms and the two crushing failure modes. The profile and trigger shape, composite layup, properties of the constituent materials, and boundary conditions affect the occurrence of the failure modes [14, 17]. In order to replace costly experiments, attempts were made to predict crushing failure of FRPs with numerical tools based on finite element (FE) simulations since the beginning of the 1990s [18]. However, crushing turned out to be notoriously challenging to simulate due to the variety of failure mechanisms and material properties involved in the process. For this reason, the simulation of FRP crushing failure is still a subject of scientific investigations.

Composite crushing is also governed by strain rate (SR) dependencies of the FRP used. Individual mechanical properties of composite materials have been investigated by numerous authors and largely show a clear trend when SRs are raised: they tend to fail at higher loads. Depending on the failure mode, strains upon fracture can increase or decrease. However, they usually vary to a lesser degree than the corresponding strengths [19–23]. This effect can be attributed to the restricted mobility of molecular chains in composite materials exposed to higher SRs, which is similar to the effect observed at lower temperatures [24]. SR-induced property value increases play a considerable role in polymers and most fiber materials, e.g., glass fibers (GF) or aramid fibers [25–28]. An exception here is carbon fibers (CF), whose properties are not affected by SRs [29]. The SR-dependent response of FRPs under high-rate mechanical loads results from an interaction of the constituent fibers, matrix, and fiber-matrix interfaces [30].

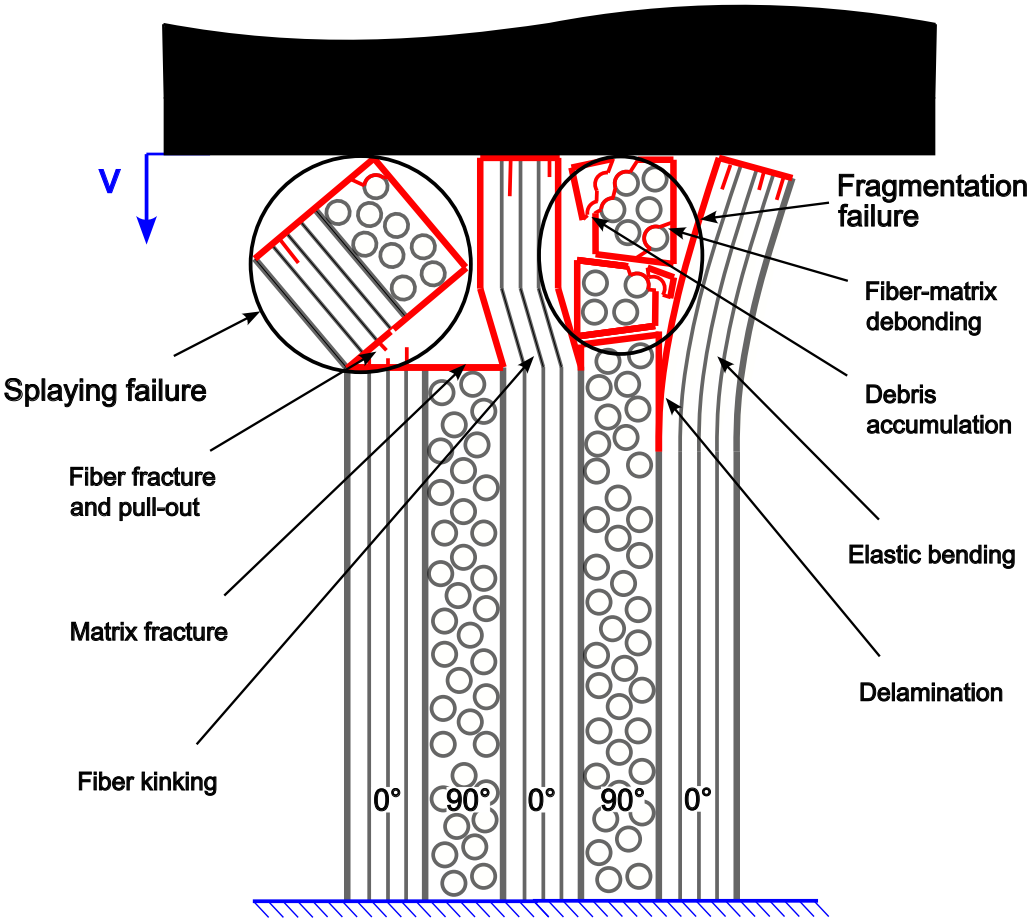

Fig. 1-2 Failure modes and micro-scale damage mechanisms in composite laminates subjected to axial crush loading.

1.2 Objectives of the thesis

Based on the previous motivation, the following research question arises:

Under which conditions can finite element models replicate composite crushing, and what role do strain-rate-induced property changes play for their predictive quality?

Several primary objectives were identified in order to provide a well-founded response to this question:

- Quasi-static (QS) and high-rate (HR) experiments with specimens of increasing complexity will be used to study the compression and crushing failure of FRPs. The experimental methods should be as far as possible based on studies from the literature. A novel experimental procedure will be investigated that facilitates the study of flat crushing coupons under the influence of high loading rates.
- Numerical simulations will accompany the experimental investigations: Commercial material models, material data from a well-studied FRP, and varying through-thickness discretizations build the basis for the model setup.
- Material parameters with particular regard to SR effects will be evaluated. In addition, the influence of the selected boundary conditions and model simplifications on the results has to be studied.
- Possible limitations of the present modeling approach will be identified to outline promising objectives to further enhance and accelerate crushing simulations of FRPs beyond the scope of this thesis.

1.3 Thesis outline

Chapter 1 introduced the significance of crushing failure in a commercial application and the influencing factors and challenges that need to be accounted for when dealing with this type of failure in composites. Additionally, the research question that motivates investigations within the framework of a doctoral thesis was formulated. Based on the motivation, several objectives were defined, and an outline of the entire thesis document was provided.

Chapter 2 presents an extensive literature review of existing studies on the numerical representation of composite crushing with particular reference to studies considering SR effects. Furthermore, it summarizes the publications that have studied the crushing failure in coupon-level experiments and simulations.

Chapter 3 provides an overview of the material properties for a unidirectional (UD) carbon/epoxy material that serves as the database for the numerical models. The database covers elastic parameters, strengths, and fracture toughnesses (FT) Particular attention is paid to SR dependencies of the selected material and the transfer of these properties into numerical models.

Chapter 4 presents the employed experimental geometries and methods along with the data reduction procedures of the selected studies from literature and complementary in-house testing series. They comprise experiments with open-hole compression (OHC), triangular through-thickness trigger (TTT) crushing, and rectangular tube crushing specimens in Section 4.1, Section 4.2, and Section 4.3, respectively. Novel data reduction procedures are defined where necessary.

Chapter 5 introduces the reader to the applied numerical modeling strategy in LS-DYNA using shell elements or stacks of shell elements (see Section 5.1). The necessary material models and parameter definitions for the intra- and interlaminar material representation are discussed in detail. In addition, the numerical models corresponding to the experiments are presented in Section 5.2 to Section 5.4.

The outcomes of all experiments and simulations are summarized in Chapter 6. Where appropriate, numerical studies are added to the chapter to enhance the understanding of model sensitivities.

Chapter 7 presents conclusions from this doctoral thesis. The chapters of the thesis are recapitulated, and a summary comparison of the predictive quality that was reached utilizing models of different complexity and size is given.

Chapter 8 outlines areas for future study and revives the example from Chapter 1 to conclude the thesis with an application of the presented methodology on a full-scale structure.

The truncated experimental/numerical pyramid in Figure 1-3 shows the overall methodology of the thesis following the building block approach (BBA) according to EASA's modelling & simulation of CS-25 structural certification specifications [31]: Starting from the material characteristics and models, the failure behavior of specimens is investigated with increasing complexity up to an exemplary full-scale structural application. The chapters or respective sections which describe the experimental setups and numerical models are also assigned to the building block diagram.

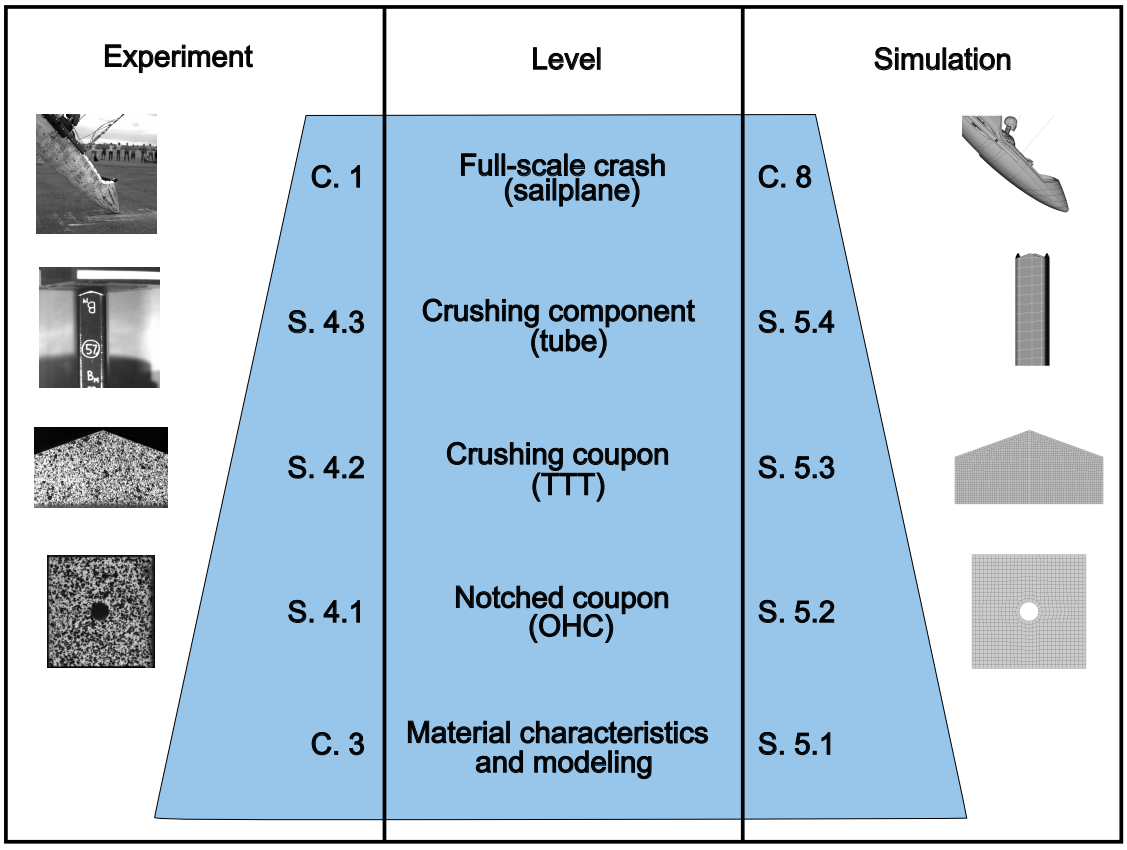

Fig. 1-3 Truncated experimental/numerical pyramid with chapter (C.) and section (S.) assignments for the present doctoral thesis.

2 Literature review

Following the objectives of the thesis outlined in Chapter 1, two fields were defined for literature review: In the first part of this chapter, studies on composite crushing FE simulations with three-dimensional (3D) geometries are presented. In the second part of the chapter, publications on experimental and numerical investigations of two-dimensional (2D) composite crushing coupons are shown, which facilitate the study of strain-rate-induced material behavior.

2.1 Numerical studies of 3D composite crushing components

Due to the amount of literature in the field, the review of 3D component crushing focuses on studies that used macro-scale or meso-scale modeling with homogenized plies and were conducted with endless-fiber-reinforced material. Thus, studies that resolved the material into fiber and matrix components, e.g., by Berger et al., are left aside [32]. Also, publications that used randomly oriented fiber mats instead of neatly oriented layers, e.g., by Böhm et al., are not taken into further account [33]. A possible way to categorize the literature studies is the trough-thickness discretization of the models. Due to their simplicity, single-shell models (SSM) are often used as the first approach to model composite crushing. They are able to replicate fragmentation failure, whereas they are not able to generate splaying failure. To account for the splaying failure mode, stacked-laminate models (SLM), discrete-ply models (DPM), or even multi-layered-ply models (MLPM) have to be created, which introduce debonding interfaces with, e.g., cohesive zone elements (CZE), between the plies or ply bundles as depicted in Figure 2-1. In the following, literature studies on the component crushing of composites are categorized accordingly and will be briefly described.

2.1.1 Single-shell models

The first contribution using SSMs was published by Matzenmiller et al. as early as 1991 [18]. They evaluated the failure of GF-reinforced crushing cylinders, considering Hashin's failure criteria in LS-DYNA [34]. Their model showed results that were fairly comparable to the experimentally determined values. McGregor et al. investigated an SSM with intralaminar material representation following the CODAM continuum damage model (CDM) implemented in LS-DYNA by Williams et al. [35, 36]. Their simulations of braided composite tubes with varying laminate

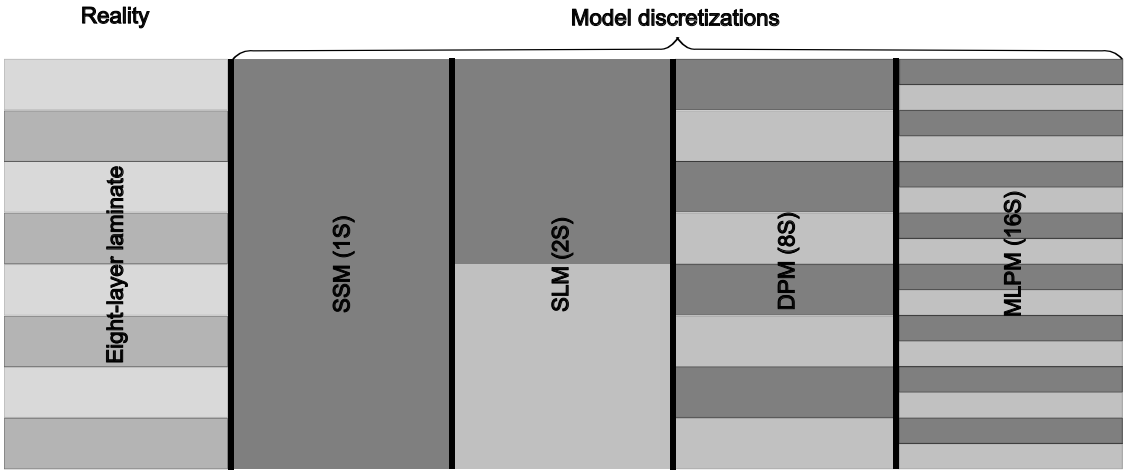

Fig. 2-1 Model discretizations on the example of an eight-layer laminate.

thickness and triggers reasonably captured the experimentally observed failure behavior. Feraboli et al. selected a built-in LS-DYNA material model with failure criteria by Chang and Chang or Tsai and Wu (*MAT_054) to perform detailed calibration studies with SSMs on corrugated specimens [37–40]. They found that a numerical softening parameter of the material model was most influential for the success of the simulations. Also, their results were very dependent on the mesh size and the filtering scheme used in the post-processing. Dalli et al. used flat and circular crushing specimens to derive the mean crushing stress (MCS) as input for a crushing definition based on contact softening (CZone) [8, 41]. Their SSM of a Formula One side crash cone with ABAQUS/Explicit CZone definition provided proper quantitative predictions at an affordable computational cost. Cherniaev et al. compared the three built-in LS-DYNA material models *MAT_054, *MAT_058, and *MAT_262 regarding the crushing performance as SSMs [42]. They found that all material models required extensive calibration. Additionally, they reported that randomization of the out-of-plane nodal coordinates proved useful for the predictive quality of the models and that SSMs were an inappropriate modeling choice to replicate splaying failure. Reiner et al. investigated the SSM crushing response of three different material formulations in ABAQUS/Explicit and LS-DYNA (*MAT_081, *MAT_219, and ABQ_DLR_UD) [43]. They analyzed the influence of the solver, mesh, and erosion definition. Their models turned out to be a computationally efficient choice to reproduce fragmentation failure without employing unphysical tweaking parameters. They also showed that higher mesh densities or unstructured meshes could mitigate load peaks and that crack band scaling did not apply to their simulations. Both latter studies used the same component crushing database as the present thesis [44]. Feser pursued an approach very similar to the present thesis, even based on the same material system [45]: He investigated the failure behavior of notched coupons, crushing coupons, and 3D profiles using experiments

and simulations with the material model ABQ_DLR_UD in ABAQUS/Explicit. Applying a thorough methodology along the different levels of the building blocks, his main conclusions on SSMs were that structured meshes can lead to catastrophic failure and that crack band scaling does not apply to crushing with fragmentation failure mode. Also, Feser demonstrated the importance of evaluating the influence of the strain-softening formulation.

2.1.2 Stacked-laminate models

Braided composite tubes were used by Xiao et al. to study the crushing failure predictivity of LS-DYNA *MAT_058 with TIEBREAK interfaces [46]. They created SLMs with failure parameters adapted to coupon experiments or property value estimates. The results correlated well regarding the maximum force but underestimated the crush force, which they interpreted as a deficiency of *MAT_058 to correctly replicate material unloading. Huang et al. created SLMs of circular CF/epoxy tubes with two laminate layers of *MAT_054 in LS-DYNA, whereby they mostly adopted damage property definitions from the literature [47]. TIEBREAK contact option 8, based on interlaminar strength, was defined to account for delaminations. This contact model is equivalent to a cohesive element damage formulation driven by interlaminar strengths. The authors concluded that their approach could effectively model the crushing process with a brittle fracture mode. Siromani et al. applied the same combination of *MAT_054 and TIEBREAK contact to replicate the crushing behavior of a circular tube with an SLM [48]. The cohesive zone failure parameters were partly defined based on the interlaminar FTs to enhance the physical motivation of the model. Intralaminar failure parameters were calibrated to match the experimental results. The models accurately captured the crushing characteristics, but the authors concluded that the models could be further improved with ply-by-ply discretization, finer meshes, or mesh alignment. David and Johnson were the first authors to consider SR dependencies for their SLMs created in PAM-CRASH [49]. Half-circle segments were meshed, and the material parameters of a CF/epoxy composite calibrated to coincide with experimental characteristics over two strain-rate regimes. Supporting the failure initiation with a numerical trigger, their ABAQUS/Explicit HR models successfully captured the crushing behavior and force-displacement curve. In contrast, their QS models succumbed to global buckling failure not observed in the experiments. Reuter et al. used experimental data from flat coupons tested in a fixture as proposed by Feindler to calibrate the lamina material properties of their CF-epoxy material [50, 51]. Again, SLMs were set up with *MAT_054 laminae and TIEBREAK interfaces. For various materials, layups, and specimen geometries, their models produced results that were equally good. In two publications, McGregor et al. investigated SLMs utilizing the aforementioned

CODAM model combined with TIEBREAK contacts [52, 53]. Different coupon experiments built the database for the calibration of the intralaminar material card. Only a quarter of their double-symmetric square profile braided tubes was used for the simulation models. They evaluated crushing with a plug trigger but also free crushing with an artificial rigid debris wedge added to the simulation after the end of the trigger phase. The SEA appeared to be well-predicted for all configurations, whereas the load peaks were overpredicted for the models with a plug. SSMs and staggered SLMs were employed by Striewe et al. to simulate the crushing of thermo-formed GF-thermoplastic profiles [54]. They also applied the common LS-DYNA modeling combination *MAT_054/TIEBREAK and received excellent numerical predictions after an iterative optimization process. Physically motivated SLMs with different ply bundling, friction coefficient, and interface property definitions were examined by Chen et al. [55]. They received the best fit for their QS and HR GF/epoxy tube crushing experiments using six-ply bundles and a novel scaling approach for the interlaminar FTs. Sommer et al. studied the crushing of circular IM7/8552 tubes with stacked +45° and -45° plies and an academic 3D CDM with TIEBREAK interfaces and consideration of SR-dependent behavior in LS-DYNA [56]. They also conducted parameter studies with different bevel trigger geometries. They concluded that an accurate forecast of the crushing response required a fiber-aligned mesh and a proper combination of interlaminar FTs and friction.

2.1.3 Discrete-ply models

Sokolinsky et al. proposed a physics-based approach in ABAQUS/Explicit to predict crushing as observed in the experiments with corrugated specimens by Feraboli [39, 57]. Their stacked shell/cohesive DPMs showed high potential for realistically simulating composite crushing structures. In the work of Feindler, DPMs of three crushing geometries were created in PAM-CRASH [50]. Based on material data from coupon experiments and supported by a rigid debris wedge, the models were mainly able to produce progressive crushing. They correlated well with the experiments regarding force levels. Matheis et al. evaluated a numerical modeling approach for braided, circular CF/epoxy tubes in LS-DYNA. They calibrated interlaminar TIEBREAK contact option 8 with a double-cantilever beam experiment [58]. A quasi-DPM was created by dividing braided layers into separate layers with one fiber orientation each. To replicate the failure behavior for varying fiber angles and filler yarn ratios, *MAT_058 model parameters SLIM and ERODS had to be adapted individually for each variant. Bussadori et al. compared different modeling techniques in PAM-CRASH [59]: a SSM using a crushing zone definition similar to CZone in ABAQUS/Explicit and stacked-shell models using different numbers

of shells through the thickness. Since their SLM and DPM did not reach the experimentally observed load level, they recommended using crushing zone models like CZone for engineering applications. A crush absorber for crashworthy aircraft fuselage structures was modeled as DPM in ABAQUS/Explicit by Waimer et al. [13]. They studied appropriate meshing strategies and generally applicable definitions of the intra- and interlaminar properties derived from coupon experiments. Without changing the numerical approach or input parameters, their model could handle various crushing failure modes. However, the cohesive interface model exhibited numerical instabilities when complex loading conditions were present at the structural level. Ren et al. also took the experimental crushing database from Feraboli and the CODAM model already mentioned to set up their models [39, 60]. They implemented the CODAM model in ABAQUS/Explicit and combined it with a cohesive contact to create DPMs and study influences of material parameters and geometrical characteristics. They concluded that friction and compression strength played an important role in crushing failure and that staggered meshes should be preferred to aligned meshes for this failure type. Another DPM study was carried out by Karagiozova et al. [61]. They proposed a novel modeling technique replacing cohesive elements in the debonding interfaces with isotropic resin shell elements. Thus, stacks of tied shells and shells serving as cohesive elements were used to evaluate different layups and loading rate effects in ABAQUS/Explicit. Apart from the intralaminar FTs, they only applied experimentally determined CF/epoxy material values. Their approach did not consider SR dependencies but was able to reproduce the mostly rate-insensitive experiments in large parts. Also, it was superior to CZEs regarding computation time and premature interlaminar failure. Atabaadi et al. focused on accurately predicting the crushing modes in their DPMs [62]. They used stacked shells and cohesive elements in ABAQUS/Explicit and implemented a VUMAT to, e.g., optimize the element deletion scheme. Excellent agreement of the numerical models with high-velocity experiments on CF/epoxy tubes with varying stacking sequences was reported [63]. Costa et al. employed tube crushing experiments and FE simulations to validate a novel composite damage model [64]. Their LS-DYNA DPMs, made up of solid elements with cohesive element interfaces, could replicate crushing failure but underestimated the load due to premature layer debonding. Rondina et al. studied the predictive capabilities of the CDM by Ladèveze as well as Pineda and Waas [65–69]. The authors sought to define, where possible, physics-based DPMs and investigated the crushing behavior of corrugated carbon fiber-reinforced composites (CFRP) components. They obtained adequate responses from their simulations combining shell elements (MAT131) and TIED beams (MAT303) in PAM-CRASH for both damage models compared to experiments. In addition, they evaluated the influences of mesh objectivity, friction, and interlaminar damage parameters. They found that calibrations of interlaminar

fracture toughnesses were necessary to obtain reasonable results. Another of the few studies on numerical composite crushing considering SR-dependent behavior was conducted by Chen et al. [70]. They carried out QS and HR experiments on CF- and GF-epoxy double-hat profiles and used ABAQUS/Explicit to create a DPM with cohesive-element debonding interfaces. A VUMAT with an SR-sensitive 2D material model was defined taking into account a combination of in-house data and literature data to model the SR dependencies of the in-plane properties. The interfacial properties, however, were manually amplified with a scaling factor to fit the structural response in the HR domain. The authors reported reduced absorbed energies for the CFRP specimens under high loading rate, whereas the energy absorption level remained virtually the same for the GFRP samples. Also, their simulations successfully reproduced the crushing of both materials for both loading rates with high accuracy.

2.1.4 Multi-layered-ply models

To correctly capture the post-delamination bending response of plies represented by solid elements, Chiu et al. proposed to use three elements for each ply in the thickness direction [71]. They combined a novel intralaminar material model for CF/thermoset materials, an established surface-based interlaminar material model, and fully experimentally determined input parameters to simulate tubular composite energy absorbers under QS axial loading. Thus, they obtained nonlinear, mesh-objective, and load-history-dependent material behavior and successfully reproduced the experimental material response in ABAQUS/Explicit. In a further study, the authors benchmarked their approach against QS experimental in-house along with literature results and reported maximum deviations of the SEA within 12% of the experimental value [72]. Similarly, the same research group presented a material model for CF/thermoplastic materials. In two studies, they defined the material model, discussed the role of material characterization and crush modeling, and validated the model against corrugated crushing specimens, showing negligible deviations from the experiments [73, 74]. Liu et al. proposed yet another model to capture the in-plane behavior of CF/epoxy under crush loading conditions [75]. With their MLPMs, they obtained an accurate prognosis of the damage morphology and load response compared with the circular tube experiments by Chiu et al. [71]. They used the validated models to conduct numerical studies on ply blocking and the friction coefficient. According to their models, a reduction of the impactor-specimen friction coefficient during stable crushing yielded the most realistic correlation with the experiments. Furthermore, blocked plies deteriorated the crushing performance in composite laminates due to early element erosion and decreased load-bearing capacity.

2.1.5 Strain-rate-dependent material formulation

The influence of SR-dependent property changes on crushing behavior is still subject to academic discussions [76]. To the best of the author's knowledge, only three studies investigated the influence of SR sensitivities on the crushing of composite materials to date [49, 56, 70]. However, it should be noted that other authors studied the influence of SR-dependent composite formulations on the impact of laminate plates. Wang et al. investigated low-velocity impacts onto CF/epoxy plates with a DPM consisting of shells and CZEs with a rate-dependent damage model for the intralaminar material description [77]. From their validation of the models at different impact energies, they pointed out the necessity to account for SR sensitivities in low-velocity impact simulations. Liu et al. conducted low- and high-velocity impact experiments on CF/epoxy plates with different layups [78]. They introduced dynamic increase factors to account for rate sensitivities in their in-house cohesive zone and FRP laminate damage models in ABAQUS/Explicit. Also, calculations using the built-in LS-DYNA material model *MAT_162 were used as a benchmark for the material response. They found that their model was able to replicate the failure behavior for both velocities investigated when rate effects were taken into account. The model proved superior to *MAT_162 in terms of the predicted delamination area and load-displacement curve. Furthermore, the publication of Kim et al. aimed to evaluate SR effects on the frontal crash of a bumper beam structure manufactured from GF-reinforced thermoplastic material [79]. They determined the necessary QS and dynamic material properties to define two individual material cards in LS-DYNA *MAT_058. From their substructure shell element simulations, they reported that rate effects tended to be more apparent at higher impact velocities, which was also a result of Wang et al. These findings – regardless of the loadcase, numerical tool, and material system – underline the increasing necessity to account for SR effects with a growing loading rate.

In the presented studies, rate sensitivities of material parameters were accounted for with separate data sets at high and low rates in commercial FE material models [49, 79], using parameter-based formulae for the property extrapolation in proprietary material models [56, 77, 78], or they used a combination of two mentioned methods [70]. Several commercial models in LS-DYNA offer SR-dependent formulations based on either look-up tables (e.g., *MAT_LAMINATED_COMPOSITE_FABRIC/ *MAT_058) or parameters (e.g., *MAT_COMPOSITE_MSC/*MAT_162).

2.2 Experimental and numerical studies of 2D composite crushing coupons

2D coupon geometries can be used in composite crushing experiments to reduce geometrical influences and material costs. Lavoie and Morton first suggested to impact flat coupons supported by knife edges with a sliding plate guided on linear bearings as shown in Figure 2-2a [80, 81]. Their fixture was also used in other publications: Lavoie and Kellas studied the QS and HR response of different fiber-matrix combinations and reported a load level reduction for higher SRs [82]. Cauchi Savona and Hogg, along with Daniel et al., found that rising specific sustained crushing stresses (SSCS) of GFRP resulted from interlaminar shear strength and interlaminar FT increases [83, 84]. In another study, Cauchi Savona and Hogg showed the influence of fiber architectures, matrix materials, and unsupported width on the absorbed energy of GFRP [85]. They discovered that the amount of energy absorbed depended on how stable the laminates were and whether any outside plies might have detached during crushing.

While keeping the plate from buckling, the knife edges in the supported fixture can also cause localized tearing of the laminate at the supports. Therefore, Feraboli added a free crushing length to the original fixture design shown in Figure 2-2b [86]. Guillon et al. investigated different trigger shapes, loading velocities, and laminate configurations. Israr et al. examined the concept of an MCS to characterize the crushing failure of FRPs in a QS setup [87]. Duong et al. used a guided unsupported crushing fixture for dynamic experiments on the same CF/epoxy material as Israr et al. They found that higher loading velocities also lead to higher maximum crushing forces but hardly affected the SEA [88].

Feindler proposed an experimental fixture that clamps a flat specimen to a base plate and gets loaded quasi-statically by a square-profiled impactor Figure 2-2c [50]. Lausch et al. adopted Feindler's fixture and specimen geometry. They developed a data reduction framework to separate the influence of the lateral splitting load contribution from the crushing load [89]. As already mentioned in the last section, Reuter et al. used the coupon crushing configuration with laterally clamped specimens [51].

To further simplify the fixture design and minimize the material required for testing, Gutkin and Pinho first studied the flat-plate loading of a clamped specimen with unsupported length and bevel trigger as shown in Figure 2-2d [90]. Their approach was adopted and refined by Bru et al. [91]. They increased the crushing length and came up with a triangular-shaped through-thickness trigger (TTT), which minimized delamination during the crushing initiation of CF/epoxy samples. Ma et

al. investigated the original, symmetrical TTTs by Bru et al., but also unsymmetrical triangle triggers varying the angles of the triangles [92]. From their QS crushing experiments on CF/PA6, they reported a change in failure mode and higher SEAs for steeper trigger triangles. Liu et al. studied the coupon-level QS crushing of UD and hybrid UD/woven CF/epoxy material systems with bevel- and steeple-trigger specimens [93]. They reported higher sustained loads and SEAs for steeple-trigger specimens and the hybrid UD/woven material. Dalli et al. used the specimen design of Bru et al. to characterize the QS and HR crushing stress of a woven CF/epoxy material. However, they increased the specimen size due to the dimensions of the unit cell in their material [8]. Their QS experimental results were similar to those of the other given sources. Experiments under HR loads exhibited spurious oscillations of the force level. They highlighted the need for a better understanding of the interaction between the experimental setup, the coupon geometry, and the material response.

Apart from their experimental investigations, Guillon et al. studied pseudo 2D discrete-ply models (DPM) with physically motivated debonding interfaces to simulate the behavior of their guided, unsupported crushing specimens in ABAQUS/ Explicit [94]. They presented good agreement with the results of experiments using a metallic blade trigger. Israr et al. extended their numerical work by using a free-face-crushing concept, which applied two damage criteria: a softening criterion resembling CZone at the edge of the plies and a classical failure criterion inside the plies [95]. They reported good correlations with QS experiments but an underestimation of the crushing load in HR simulations. Even better agreement with the results of the experiments by Israr et al. and Duong et al. was achieved when Grotto et al. expanded their work to a 3D representation with DPMs and the definition of an MCS [96]. Feindler was able to numerically replicate the failure mode of his laterally clamped specimens with 3D DPMs using built-in PAM-CRASH material formulations [50]. His models correlated well with the experiments during the stable crushing phase, whereas they underestimated the initiation stress. Gutkin and Pinho successfully evaluated a newly developed 3D material model on their transversely loaded UD CF/epoxy out-of-plane shear samples [90]. QS results of Israr et al., as well as Gutkin and Pinho, were taken by Tan et al. to validate their 3D MLPM approach combined with a surface-based cohesive formulation in ABAQUS/Explicit [87, 90, 95, 97]. They adopted the damage models of Puck and Schuermann as well as Catalanotti et al. and applied a robust element deletion strategy to correctly replicate the crushing mechanisms [98, 99]. Depending on the crushing trigger, material system, and layup, they reported good correlation with the experiments during the initiation phase, but varying predictive success during the phase of stable crushing. Furthermore, Liu et al. created solid-element

models of their previously mentioned specimens to numerically predict coupon crushing in ABAQUS/Explicit [93]. Their models were again based on Puck and Schuermann's works and contributions from other authors [98–101]. Liu et al. were able to replicate the QS coupon failure behavior in their simulations with high accuracy. Feser compared SSMs and DPMs of flat, guided crushing coupons [45]. Since splaying failure was observed in the underlying experiments, SSMs were unable to correctly replicate the failure behavior, but DPMs showed a good correlation. Also, Feser underlined the necessity to investigate strain rate effects on composite crushing in future research. Engül and Ersoy experimented with Bru's bevel trigger coupons [102]. They created DPM models to improve the understanding of the failure mechanisms during the crushing process, but also applied SLMs to reduce simulation runtimes. They reached a high predictive quality with both modeling approaches and for different layups. Their SLM models were reported to decrease computation runtimes by more than 50%.

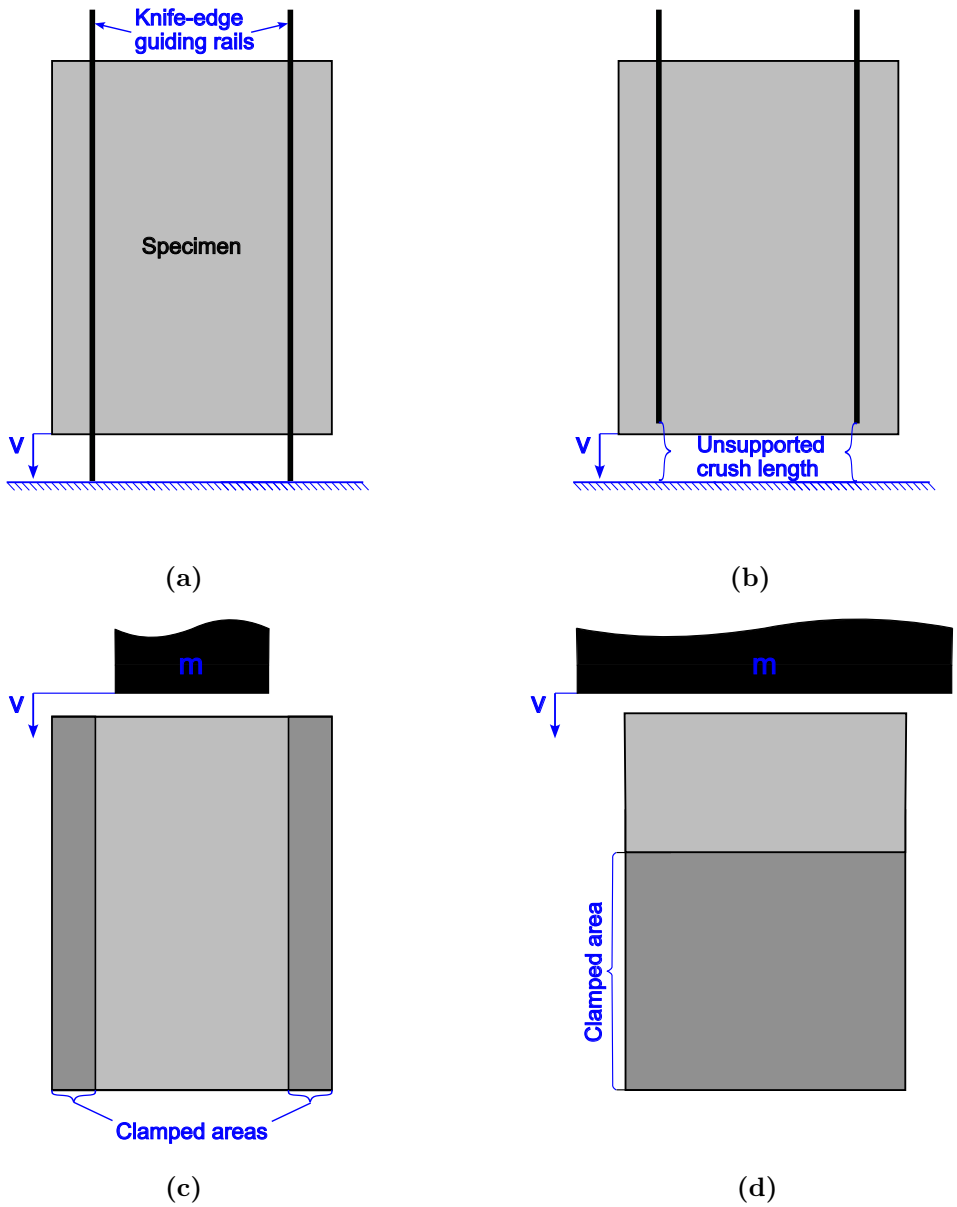

Fig. 2-2 Comparison of designs for coupon crushing experiments (specimens without trigger): (a) Guided specimen sliding in crushing fixture, (b) guided specimen sliding in crushing fixture with unsupported crushing length, (c) impactor crushing onto laterally clamped specimen, and (d) impactor crushing onto specimen clamped at the bottom, but unsupported in crushing length.

3 Material database

Since its introduction to the market in the 1990s, Hexcel's IM7/8552 prepreg has become a popular material system for primary aerospace structures due to its excellent mechanical properties and processing capabilities [103–105]. With its additional high fiber volume content (FVC) of about 58% achievable when cured in an autoclave [106], the material also gained popularity as a research subject. To the author's knowledge, IM7/8552 currently offers the most extensive open-access material database of any fiber-reinforced plastic (FRP) and was therefore selected for the present thesis.

The following section and tables describe the mechanical properties of the IM7/8552 EU version and also form part of the publication by Pohl et al. [107]. The adapted overview of elastic properties, strengths, and FTs under QS and HR loading is repeated here for the sake of completeness. In the tables, E_{ii} and G_{ij} denominate the elastic modulus in the ii-direction and the shear modulus in the ij-direction, respectively. S_{ij} and G_{ijc} represent the strength in the ij-direction and FT in the ij-direction. Indices T and C mark tensile and compressive loading, whereas QS and HR stand for the strain rate regime. Apart from material properties observed in experiments, the tables also contain extrapolations of the QS values to the HR domain. The extrapolations were calculated with the following expressions derived for IM7/8552 by Koerber [108]:

Extrapolation factor for elastic properties:

$$f_e(\dot{\epsilon}) = 1 + (K_e \cdot \dot{\epsilon})^{\frac{1}{n_e}},\ K_e = 1.60 \cdot 10^{-4},\ n_e = 2 \tag{3-1}$$

Extrapolation factor for strength properties:

$$f_u(\dot{\epsilon}) = 1 + (K_u \cdot \dot{\epsilon})^{\frac{1}{n_u}},\ K_u = 1.13 \cdot 10^{-4},\ n_u = 4 \tag{3-2}$$

The FT extrapolation factor is derived from the latter formula, assuming a quadratic influence of the strength increase factor onto the critical strain energy release rates:

$$f_{ft}(\dot{\epsilon}) = (1 + (K_u \cdot \dot{\epsilon})^{\frac{1}{n_u}})^2,\ K_u = 1.13 \cdot 10^{-4},\ n_u = 4 \tag{3-3}$$

$\dot{\epsilon}$ represents the corresponding strain rate, K and n are regression coefficients and exponents.

Tab. 3-1 Elastic properties of IM7/8552 composite (extrapolated HR values in parentheses).

Property	Value (Equation 3-1)	SR	Source or formula
$E^{\mathrm{a}}_{11,T,QS}$	164,000 MPa	-	[106]
$E^{\mathrm{b}}_{11,C,QS}$	154,486 MPa	-	[20]
$E^{\mathrm{c}}_{22,T,QS}$	8,691 MPa	-	[21]
$E^{\mathrm{c,d}}_{22,T,HR}$	10,706 (10,501) MPa	271 1/s	[21]
$E_{22,C,QS}$	8,930 MPa	-	[19]
$E^{\mathrm{d}}_{22,C,HR}$	10,019 (10,789) MPa	271 1/s	[19]
$G^{\mathrm{e}}_{12,QS}$	5,068 MPa	-	[19]
$G^{\mathrm{f}}_{12,HR}$	6,345 (6,178) MPa	$\approx$ 300 1/s	[19]
$G_{23,QS}$	2,977 MPa	-	$G_{23,QS} = E_{22,QS}/(2 \cdot (1 + \nu_{32}))$
$G^{\mathrm{g}}_{23,HR}$	3,340 (3,597) MPa	271 1/s	$G_{23,HR} = E_{22,HR}/(2 \cdot (1 + \nu_{32}))$
ν^{h}_{21}	0.019	-	[109]
ν^{i}_{32}	0.5	-	-

[a] Tensile 11 Young's modulus does not depend on the SR [110]

[b] Compressive 11 Young's modulus is only slightly SR-sensitive [111]

[c] Calculated from raw data [21]

[d] Yield SR

[e] Transversal isotropy ($G_{13} = G_{12}$)

[f] Shear elongation SR at yield

[g] Young's modulus extrapolation with the SR from $E_{22,\mathrm{HR}}$

[h] Minor Poisson's ratio

[i] Assuming incompressibility

Tab. 3-2 Strength properties of IM7/8552 composite (extrapolated HR values in parentheses).

Property	Value (Equation 3-2)	SR	Source
$S^{\mathrm{a}}_{11,T}$	2,724 MPa	-	[106]
$S_{11,C,QS}$	1,454 MPa	-	[22]
$S_{11,C,HR}$	2,008 (1,928) MPa	100 1/s	[22]
$S_{22,T,QS}$	62 MPa	-	[21]
$S_{22,T,HR}$	82 (88) MPa	271 1/s	[21]
$S_{22,C,QS}$	255 MPa	-	[19]
$S^{\mathrm{b}}_{22,C,HR}$	371 (362) MPa	276 1/s	[19]
$S^{\mathrm{c}}_{33,T,QS}$	110.4 MPa	-	[112]

$S_{12,QS}$	99.9 MPa	-	[19]
$S^{d}_{12,HR}$	141.8 (150.9) MPa	≈ 600 1/s	[19]
$S^{e}_{13,QS}$	95.8 MPa	-	[113]

[a] 11 tensile strength does not depend on the SR [110]

[b] Failure SR

[c] Refined interlaminar tensile strength experiments, average-stress

[d] Shear elongation SR at failure

[e] SR calculated from loading rate in 1.5-inch specimen experiments with lowest CV

Tab. 3-3 FT of IM7/8552 composite (extrapolated HR values in parentheses).

Property	Value (Equation 3-3)	SR	Source or formula
$G_{11c,T,QS}$	195.5 N/mm	-	[114]
$G^{a}_{11c,T,HR}$	241.0 (251.6) N/mm	60 1/s	[114]
$G_{11c,C,QS}$	83.9 N/mm	-	Based on [115]
$G_{11c,C,HR}$	135.1 (147.5) N/mm	100 1/s	Based on [115]
$G^{b}_{22c,T,QS}$	0.262 N/mm	-	[116]
$G^{b}_{33c,T,QS}$	0.229 N/mm	-	[116]
$G^{c}_{33c,T,HR}$	0.2 N/mm	≈ 80 1/s	[117]
$G^{d}_{33c,C,QS}$	5.1 N/mm	-	$G_{33c,C,QS} = f(G_{13c,QS},t)$
$G^{b}_{13c,QS}$	1.23 N/mm	-	[118]
$G_{13c,HR}$	0.970 N/mm	≈ 22 1/s	[119]

[a] Using Equation 3-2 for the FT extrapolation due to SR-independent 11-tensile strength

[b] Value from specimens with Teflon insert and non-precracked

[c] SR calculated from the crack opening rate

[d] Calculated with formula from [120]; Fracture angle $\alpha_0 = 53°$, adjustment parameter $a = 0.5$, layer thickness t, friction coefficient $\eta_T = 0.4$

The translaminar compression FTs $G_{11c,C}$ in Table 3-3 were reduced by about 20% compared to the value published by Kuhn et al. [115]. The reduction is due to a change in laminate elasticity introduced to match the elastic properties to those of the present numerical models. A detailed overview of the adaption can be found in Appendix A.1. The table also differs from the publication in the interlaminar mode I and II fracture toughnesses $G_{33c,T,QS}$ and $G_{13c,QS}$, which are now taken from specimens with Teflon inserts instead of fatigue-precracked samples. The out-of-plane properties build the basis for a detailed model evaluation in Chapter 5. Also, based on the results of the studies by Ponnusami et al. and Yasaee et al.

[117, 119], these fracture energies are assumed SR-independent along with the elastic moduli $E_{11,\mathrm{i}}$ and tensile strength in longitudinal direction $S_{11,\mathrm{T}}$. This assumption is common sense when dealing with CF-reinforced materials [110]. All other properties are considered SR-dependent following the Cowper-Symonds extrapolations. This approach was also chosen for the out-of-plane strength properties, even though to date, there are no material properties reported in the literature. Still, the assumption aligns well with the studies of Sommer et al. and Chen et al., who applied increases in these strength properties for HR simulations independently of each other [56, 70].

4 Experimental methodology

The content of the following chapter, including text and figures, has already been partly published by Pohl et al. [107, 121]. Three geometries were selected to study the compression and crushing behavior of IM7/8552: a simple failure mode with very localized crack growth was reached with OHC specimens, whereas TTT specimens facilitated studies on small-scale, flat crushing samples. Finally, crushing tubes were used to evaluate the crushing behavior on a curved 3D geometry.

4.1 Open-hole compression experiments

4.1.1 Specimen design

The OHC specimen proportions and a suitable quasi-isotropic (QI) stacking sequence ($(90/0/\pm45)_{2s}$) were defined based on ASTM D6484/D6484M, resulting in a laminate thickness of 2 mm [122]. A non-standard specimen size with a width of 9 mm, an unsupported length of 9 mm, and a hole diameter of 1.5 mm had to be chosen to test the specimens with the available split-Hopkinson bar setup. The center holes prevented the standard back-to-back strain gauge configuration, and the HR test setup's optical strain measurement did not support using a test device to prevent buckling failure. As a result, the research findings of Bessa were utilized for a preliminary examination of buckling [123]. With safety factors higher than 2, it was possible to declare the chosen laminate thickness insensitive to buckling for both strain rate regimes (see Appendix A.2).

Flat plates were manufactured from IM7/8552 using a hot press, and the curing cycle suggested in the manufacturer's data sheet [106]. The plates were drilled, the samples were cut out with a saw, and wet ground. Based on an existing shape that enables a combined load introduction, identical specimen adapters for QS and HR compression studies were made from steel rods [22]. 3M Scotchweld DP 490 structural adhesive was used to connect the specimens to the adapters, acrylic paint was applied to add a random black and white speckle pattern, and the clamps were pretensioned with a torque of 2.0 Nm. Figure 4-1a shows one of the prepared specimens as an example.

4.1.2 Experimental setup

The QS experiments were carried out on a Hegewald & Peschke electro-mechanical testing machine. A 20 kN load cell was used to quantify the force, and stress was

determined using the actual specimen dimensions subsequently. With the aid of the program GOM Correlate and a virtual, 6 mm long virtual strain gauge centered on the hole, the strain was assessed optically. Four specimens were evaluated at a crosshead velocity of 0.54 mm/min, resulting in a nominal SR of 0.001 1/s.

During the HR studies, a split-Hopkinson pressure bar arrangement was employed. It is made up of a steel striker, incident, and transmission bar with uniform diameters of 18 mm and corresponding lengths of 0.6 m, 2.6 m, and 1.6 m. Strain gauges positioned on the incident bar at a distance of 1.3 m and on the transmission bar at a distance of 0.3 m from the bar-specimen interfaces were used to identify the elastic waves. With a frequency setting of 300 kHz and a gain setting of 100, the bar strain signals were sent to a FE-H379-TA high-speed transducer amplifier from FYLDE Modular Instrumentation. A Tektronix TDS2004C oscilloscope was then used to capture the amplified signals of the bar gauges and the striker bar's velocity. To achieve a continuous SR plateau of around 100 1/s, an incident bar velocity of about 6.0 m/s was defined. A 1.5 mm thick cylindrical copper platelet with a 5 mm diameter was selected as a pulse shaper. When tested, four specimens produced experiments that were close to dynamic equilibrium upon fracture: Figure 4-1b shows a comparison of the force curves over time in the incident and transmission bar, which are almost identical at the force peaks. Stresses were calculated from the conservative transmission bar signals, taking into account the actual specimen cross-sectional area and using a Savitzky-Golay-filter of order 4 and a window of 21 frames. A Shimadzu HPV-X2 high-speed camera with a resolution of 400 by 250 pixels and a frame rate of 400,000 to 500,000 fps was used to detect strain optically. The lens's aperture was set to f/8. During the recording, a well-lit specimen surface was supplied by two LED lights. The collected pictures underwent the same post-processing as the QS tests. The reader is directed to Ploeckl et al. for a more thorough explanation of the HR compression testing approach, including the processing of the strain data from the bar gauges [22].

4.1.3 Data reduction

Stress-strain curves were employed to evaluate OHC failure. The cross-section force was divided by the nominal cross-section area of the specimens to determine the stress for the OHC experiments. With a virtual strain gauge 6 mm long and centered on the hole, the strain was measured in the loading direction. Further evaluations were carried out on the curves to derive the initial stiffness, maximum stress, and strain at maximum stress.

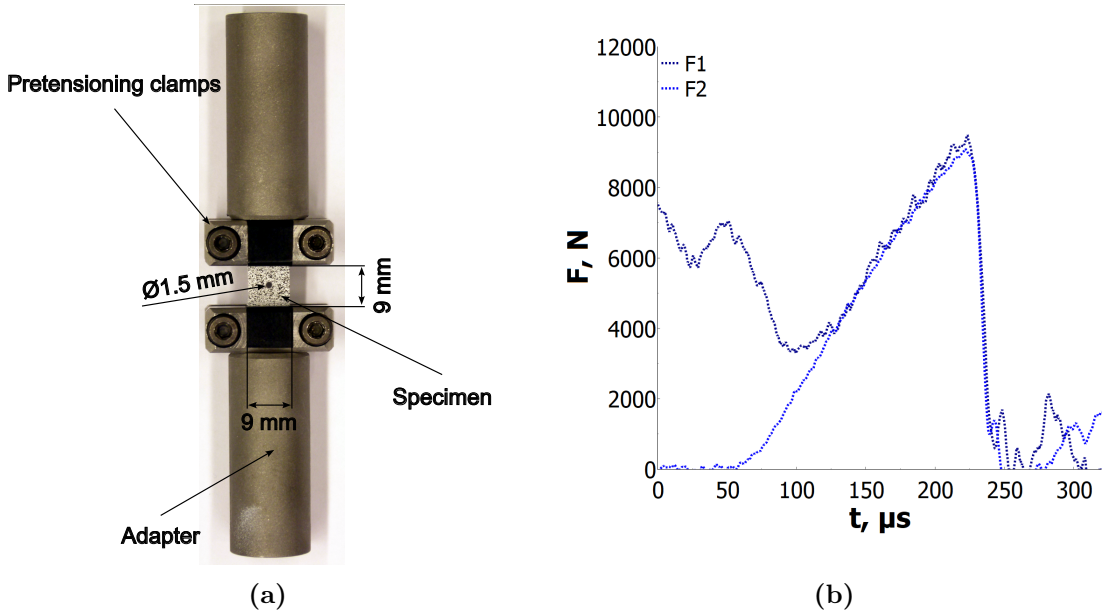

(a) (b)

Fig. 4-1 (a) OHC specimen with dimensions prepared for testing and (b) recorded forces for this specimen in the incident (F_1) and transmission bar (F_2) during impact.

4.2 Crushing experiments with triangular through-thickness trigger specimens

4.2.1 Specimen design

The geometries suggested by Bru et al. served as the basis for the coupon specimen design used in this work [91]. Their TTT design was modified as depicted in Figure 4-2a. The visible crushing length and area were maximized in comparison to the original design through preliminary numerical calculations (see Appendix A.3). A trigger angle of 20° and a free length of 10 mm turned out to be the most effective settings regarding crushing length and buckling tendency. A 2 mm thick quasi-isotropic laminate ($(90/0/\pm 45)_{2s}$) made from carbon-epoxy material IM7/8552 from the same material batch as the OHC specimens was used to manufacture specimens by milling and grinding. Also, in Figure 4-2a, the selected specimen size and boundary conditions for the TTT experiments are shown.

4.2.2 Experimental setup

At the University of Oxford's Impact Engineering Laboratory, two identical specimen series were tested as follows: on a Zwick Roell universal testing machine (UTM) at a medium, constant loading rate of 1 mm/s (MR) and on a drop-tower setup with a 6.2 kg impactor mass at 4.56 m/s (HR). The velocity of the drop-tower impactor

was measured using a photoelectric sensor. The specimens were finger-tightened in the testing fixtures, which were bolted to a steel frame to prevent vibrations reported by Dalli et al. with their untightened fixtures [8]. A force transducer fixture with an integrated Kistler 9349A load cell was used, offering a maximum sampling frequency of 2,500,000 Hz. The force transducer was embedded in a cylindrical tube serving as an overload protection system (see Appendix A.4). The output signal was recorded and amplified in a Tektronix DPO4034. By integrating the recorded force twice and dividing it by the drop weight mass, the load cell displacement signal was deduced in the HR setup. In addition, two high-speed cameras were deployed at a rate of about 100,000 frames per second for the drop-tower tests. They allow for an evaluation of local strain rates and failure patterns. They were put in place perpendicular to one another to capture the failure patterns and facilitate a subsequent strain field evaluation on the specimen surface. A summary of the HR experimental setup is provided in Figure 4-2b.

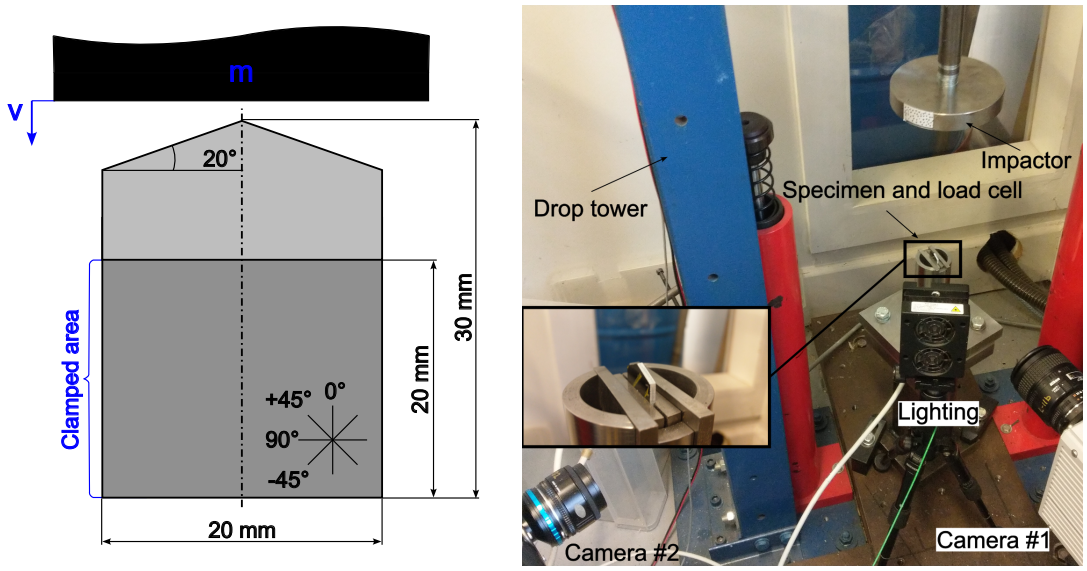

Fig. 4-2 (a) Specimen dimensions and boundary conditions for TTT experiments and (b) immediate specimen surroundings for TTT HR experiments: drop-tower with impactor, load cell, specimen, lighting and two high-speed cameras.

4.2.3 Data reduction

In order to calculate the far-field stress that resulted from the TTT experiments, the cross-section force was divided by the nominal cross-section area of the specimens. Evaluations of the stress-displacement along with the energy-displacement behavior were carried out. Further analyses were conducted on the unfiltered stress-

displacement curves to derive the maximum initiation stress, the MCS between 5 mm and 6.5 mm displacement, as well as the SEA up to 6.5 mm displacement.

4.3 Tube crushing experiments

4.3.1 Specimen design

For the tube crushing investigation, experimental data were obtained from published sources. As described in detail by Courteau, the University of Utah produced the examined crushing components [124]. Roll wrapping was used to manufacture tubes that were 200 mm × 50 mm × 50 mm in size on square-profiled aluminum mandrels with a 0.25° draft angle. The tubes were subjected to a modified IM7/8552 curing cycle on a compaction device. The curing process involved soaking at 107°C for 80 minutes and subsequent tempering at 160°C for 120 minutes. The author reported to have reached full cure. Therefore, the change in mechanical properties compared to the manufacturer's curing cycle is considered negligible. The thickness of the corner sections was 2.03 mm on average, compared to 2.16 mm for the flat section. One of the tube edges was cut at an angle of 20° using a diamond saw to create a tulip trigger geometry. Among other layups, a QI ($(90_2/\pm 45_2/0_2)_s$) stacking sequence was examined. It was designed to combine a splaying and fragmentation failure mode and increase the probability of forming a debris wedge [124].

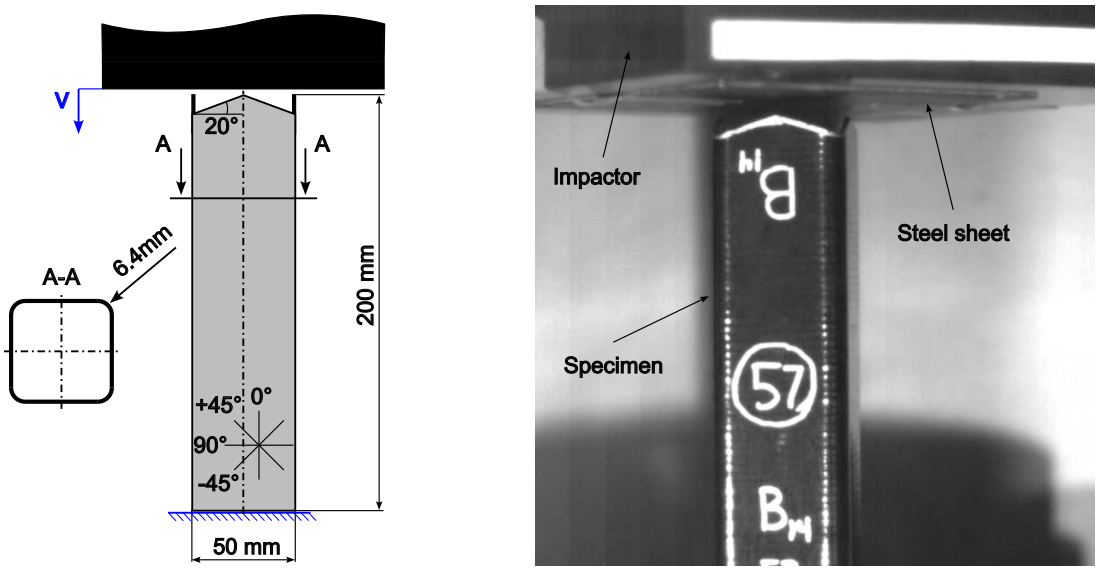

Fig. 4-3 (a) Sketch of experimental setup for tube crushing and (b) specimen 57B prior to the HR test [44].

4.3.2 Experimental setup

The experiments were conducted by Oak Ridge National Laboratory (ORNL), and the results were released online [44]. Square tubes manufactured out of IM7/8552 were impacted over a length of approximately 100 mm at an initial velocity of about 6 m/s. The impactor was covered with a cold rolled steel sheet, which was replaced after each impact. For each of the HR tests, load and displacement information, along with a high-speed video, were captured. Throughout the procedure, samples were not clamped; instead, they positioned themselves on the supporting plate. The QS specimens were tested over a length of 50 mm utilizing the same setup on a UTM at a speed of 25.4 mm/min. An overview of the specimen geometry and dynamic test setup is given in Figure 4-3.

4.3.3 Data reduction

The crushing behavior was quantitatively evaluated using force-displacement and energy-displacement curves. The curves were studied uniformly up to 50 mm displacement, which was the maximum displacement reached in the QS experiments. The load curves from the HR experiment had to be cropped subsequently to make the duration of the experiments comparable to each other. The maximum initiation force was determined from unfiltered load-diplacement data along with the specific sustained crushing stress (SSCS), which corresponds to the SEA during the stable crushing phase. Deviating from the approach by Courteau, who introduced an individual stable crushing length for each experiment, stable crushing was defined to occur between 20 mm and 50 mm displacement [124]:

$$SSCS = \frac{\int F(x)\,dx}{V_s \cdot \rho}. \tag{4-1}$$

where $F(x)$ denominates the force as a function of displacement, V_s represents the specimen's crushed volume, and ρ the material density. In addition, the mean crushing stress deviation (MCSD) was defined as a measure of the load level fluctuation in the stable crushing phase from 20 mm to 50 mm displacement:

$$MCSD = \sqrt{\frac{\int (F(x) - F_\mathrm{crush})^2\,dx}{x_\mathrm{crush}}} \tag{4-2}$$

with

$$F_\mathrm{crush} = \frac{\int F(x)\,dx}{x_\mathrm{crush}} \tag{4-3}$$

where x_{crush} denominates the crushing length of 30 mm between 20 mm and 50 mm displacement.

5 Numerical methodology

This chapter builds the central methodical part of this doctoral thesis and the already published studies by Pohl et al. likewise [107, 121]. In the following, their applied methodology will be presented in more detail than in the publications, e.g., adding the results of single-element (SE) simulations (Subsection 5.1.1) or a revision of the interlaminar properties, which led to better comparability with the experiments (Subsection 5.1.2). The descriptions of the OHC, TTT crushing, and tube crushing models in Section 5.2, Section 5.3, and Section 5.4 are also aligned with the two publications by Pohl et al.

The FE simulations in this publication were consistently performed with LS-DYNA version R13 MPP double precision, enabling SR-dependent elasticities and tension-compression differentiation in *MAT_058. Default solver settings were used as much as possible. Simulation runs were carried out in parallel using 18 Intel Xeon E5-2690 v3 (2.6 GHz) cores on the high-performance cluster (HPC) of Leibniz Supercomputing Center in Garching.

5.1 Modeling strategy

5.1.1 Intralaminar material representation

*MAT_058 theory

Due to its suitability for UD and fabric laminate modeling, its runtime efficiency, and its capability to take SR sensitivities into account, LS-DYNA *MAT_LAMINATED_COMPOSITE_FABRIC (*MAT_058) was chosen for this work. For the transfer into full-scale airplane crash models in the underlying research effort, each of these qualities were crucial. Additionally, numerous earlier papers have benefited from *MAT_058 consistent performance over the years [42, 46, 58, 125, 126], although taking into account SR-dependent properties with look-up tables has only lately been possible.

The constitutive CDM *MAT_058 is based on the work of Matzenmiller et al. and will be explained in the following sections [127]. It assumes a plane stress state for use with shell elements and linear anisotropic elasticity following the classical lamination theory. Optionally, mode-coupling failure criteria based on the work of Hashin can be applied [34]. They are appropriate for UD-layered composites. However, the faceted failure surface type was selected in the present thesis (FS = -1), because complete laminates were modeled in all investigated geometries.

Thus, the following failure criterion is considered for the five in-plane loading modes independently:

$$e_{ij}^2 = (\frac{\sigma_{ij}}{S_{ij} \cdot (1 - d_{ij})})^2 - 1 \begin{cases} \geq 0 & \text{failed} \\ < 0 & \text{elastic,} \end{cases} \tag{5-1}$$

with e_{ij} denominating the failure variable, σ_{ij} the stress, and S_{ij} the strength in the ij-direction, respectively. Loading along fiber direction (11), transverse to the fibers (22), and shear loading are considered. In addition, tensile (T) and compressive (C) loading are differentiated in 11- and 22-direction. d_{ij} represents the simplified damage variable to account for progressive degradation, which was defined by Schweizerhof et al. as follows [128]:

$$d_{ij} = 1 - \frac{SLIM \cdot \sigma_{ij}}{E_{ij} \cdot \epsilon_{ij}} \tag{5-2}$$

$SLIM$ is the specified stress limit factor in the ij-direction, whereas the material modulus, element stress, and element true strain are represented by the variables E_{ij}, σ_{ij}, and ϵ_{ij}, respectively. After failure has begun and the limit stress is reached, with S_{ij} denoting the corresponding strength, this expression results in damage progression at a constant stress level $SLIM \cdot S_{\mathrm{ij}}$ in the ij-direction. Under the constant volume assumption, the final rupture occurs when the equivalent strain calculated on the entire strain tensor reaches the effective limit value $ERODS$.

Finally, the constitutive tensor $\boldsymbol{C}(\mathrm{d})$ can be given as a function of the undamaged ply properties and the damage variables:

$$\boldsymbol{C}(d_{ij}) = \frac{1}{D} \begin{pmatrix} (1-d_{11})E_{11} & (1-d_{11})(1-d_{22})\nu_{21}E_{22} & 0 \\ (1-d_{11})(1-d_{22})\nu_{12}E_{11} & D(1-d_{22})E_{22} & 0 \\ 0 & 0 & (1-d_{12})G_{12} \end{pmatrix} \tag{5-3}$$

where

$$D = 1 - (1 - d_{11}) \cdot (1 - d_{22}) \cdot \nu_{12} \cdot \nu_{21} > 0 \tag{5-4}$$

Insertion of fracture toughnesses and regularization approach

Since FTs are not provided as direct input parameters by material model *MAT_058, they had to be inserted implicitly through the limit stress factors. With the smallest

numerically stable limit stress factors $SLIMT2$ and $SLIMC2$ defined as 0.05, the numerically obtained energy absorption capacities for the 22-direction were already greater than the physically measured FTs. This variation was seen as inconsequential, because the FTs in the 22-direction are two orders of magnitude lower than in the 11-direction. A sensitivity assessment on quasi-isotropic OHC models with changing $SLIM2$, displayed in Figure 5-1d, supports this hypothesis. In order to simulate a shear testing curve as described by Cherniaev et al., the limit stress value for in-plane shear loading $SLIMS$ was equal to 1 [42, 125]. The corresponding factors in 11-direction were modified as shown in the following to correctly account for both tensile ($SLIMT1$) and compressive failure ($SLIMC1$).

The maximum fracture strain in 11-direction $\epsilon_{11,\mathrm{u}}$ was determined from the definition of the maximum effective strain $ERODS$, with ν_{21} being the minor Poisson's ratio [129]:

$$\epsilon_{11,u} = \frac{\sqrt{3} \cdot ERODS}{2 \cdot \sqrt{1 + \nu_{21} + \nu_{21}^2}} \tag{5-5}$$

Hence, the typical energy absorption of the material was defined using the fracture strain. Moreover, damage simulation results are known to have an intrinsic mesh dependency. To obtain objective, mesh-size-independent results, numerous authors used Bažant's crack band model [52, 120, 130]:

$$\frac{G_{11c}}{l_E} = \int_0^{\epsilon_{11,u}} \sigma_{11}\, d\epsilon_{11} \tag{5-6}$$

The compressive or tensile FT in the 11-direction is indicated by the symbol $G_{11\mathrm{c}}$ in this formula. The mathematical symbols for element stress and element true strain in the 11-direction are σ_{11} and ϵ_{11}.

The formulae mentioned above offer a closed-form expression to determine the limit stresses $SLIMT1$ and $SLIMC1$ based on the mean element length l_{E} when used in conjunction with the composite material model of *MAT_058. OHC SSMs with various mesh sizes were run using the computed values (see Figure 5-1a, Figure 5-1b, and Figure 5-1c); the resulting force-displacement curves are shown in Figure 5-1e. The curves with linear regularization (LIN) support known descriptions of the influence of the strain-softening damage definition on the fracture process [45, 131]. While keeping $ERODS$ constant, the residual stress value ($SLIM \cdot S_{11}$) increases for smaller element sizes. Hence, the strain-softening curve shows a lower damage increment for finer meshes, which excessively suppresses crack propagation. Here, the crack band model was modified using a regularization factor of $\frac{1}{\sqrt{l_{\mathrm{E}}}}$ instead of $\frac{1}{l_{\mathrm{E}}}$ to counteract the mesh size influence (k as a correctional unit parameter):

$$\frac{G_{11c}}{\sqrt{l_E}} = k \cdot \int_0^{\epsilon_{11,u}} \sigma_{11}\, d\epsilon_{11} \tag{5-7}$$

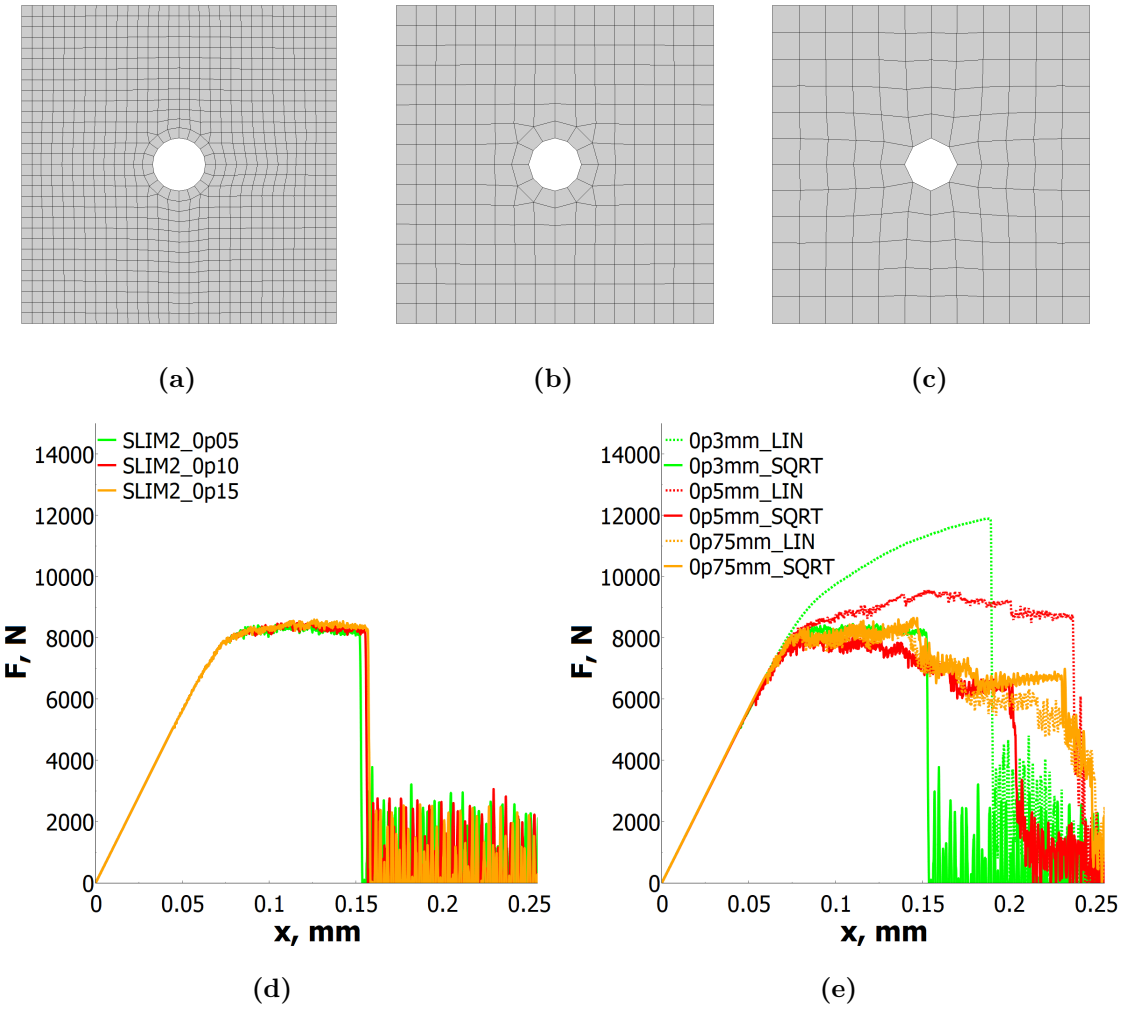

Fig. 5-1 OHC FE meshes: (a) 0.3 mm, (b) 0.5 mm, (c) 0.75 mm. Comparison of numerical OHC_QS force-displacement characteristics for (d) different SLIM2 and (e) 0.3 mm, 0.5 mm and 0.75 mm mesh size and linear (LIN) or square-root (SQRT) regularization factor.

Following the application of the nonlinear scaling factor (SQRT), the meshes obtain comparable maximum load levels and sufficiently similar failure characteristics as shown in Figure 5-1e. It should be noted that the aforementioned regularization expression may be unique to the examined coupons and components, including their crack evolution behavior, inherent material architecture, and material properties. Moreover, only element sizes from 0.3 mm to 2.0 mm were used to evaluate the regularization factor; these two mesh lengths cover a range that is relevant for the present thesis and common in engineering applications. It should also be mentioned that similar regularization techniques are frequently used for other LS-DYNA

material definitions, such as *MAT_ADD_DAMAGE_GISSMO, to eliminate mesh size effects [132].

Final definition of intralaminar characteristics

Additional parameters had to be defined to complete the material card. The shear master curve proposed by Koerber et al. was used to extract the missing properties for IM7/8552's shear behavior [23]. Neither fracture strain values nor curves were supplied for the longitudinal and transverse directions; LS-DYNA automatically determined them from the strengths and elastic characteristics. Moreover, no extra strain softening of the crash front elements was used. As was already mentioned in the previous section, the definition of maximum effective strain, or *ERODS*, is vital for understanding how damage develops since it determines the strain-softening curve shape. Thus, in all composite CDM, softening curve properties should be evaluated using experimental data: The influence of *ERODS* was assessed using the same double-edge notched compression (DENC) experiments (size B) from Kuhn et al. that had been used to characterize the corresponding intralaminar FT [115]. The FE model setup is shown in Figure 5-2a. Figure 5-2b presents a numerical DENC study using three different *ERODS* settings. Even though an *ERODS* of 0.2 slightly overshoots the average stress maximum from the experiments, the corresponding strains at maximum stress agree well. Consequently, this value was specified for the following investigations.

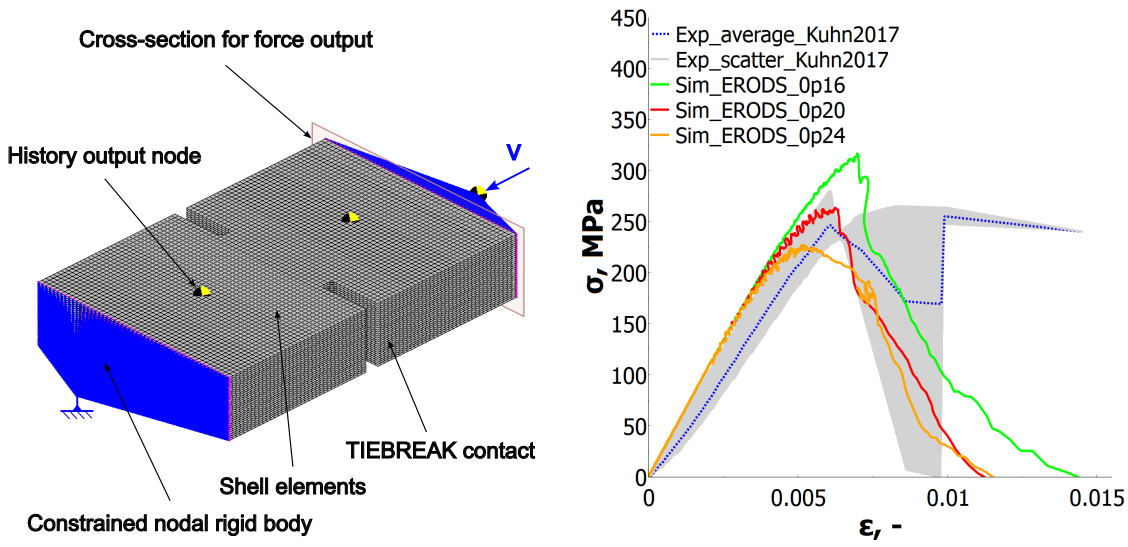

(a) (b)

Fig. 5-2 (a) DENC model with a description of constituents, boundary conditions, and output entities. (b) Comparison of experimental DENC stress-strain characteristics with respective 16S simulations at varying ERODS.

For tensile and compressive loads, asymmetric elastic behavior was defined. Increase factors were introduced using curve definitions as shown in Chapter 3 for all SR-dependent properties in the dynamic material cards. The Cowper-Symonds parameters were taken from [108]. Following the assumption of a quadratic growth of the FT values when compared to the linear growth of strength values, identical SR scaling as for the latter was applied to the maximum effective strain *ERODS* (see Equation 3-2 and Equation 3-3).

The SR-sensitive response of the material model was tested in SE simulations before further use. A sketch of an exemplary SE for the verification of the tensile and compressive behavior in fiber direction is given in Figure 5-3a. The element was loaded with a velocity of 1 mm/s yielding a nominal SR of 3.33 1/s. Figure 5-3b depicts the exemplary material response of an SE under compression loading in the QS and HR domain. Additionally, the element response was calculated in MATLAB with the analytical framework presented above (AN). The tensile stress-strain response Figure 5-3b of the QS simulation and the analytical solution show an almost identical curve in the elastic region and beyond the maximum stress limit when ϵ_x is used as strain metric. Still, this way of measuring strain exceeds the *ERODS* value of 0.2, so the effective strain has to be introduced to evaluate strain upon fracture, which in turn is not able to reproduce the correct strain at maximum stress. This deviation is caused by strain oscillations in the y- direction during load onset in the SE. Figure 5-3c shows that AN and QS final effective strains ϵ_{eff} resemble each other very closely. The persisting deviation between the curves occurs since the effective strain is calculated from the full strain tensor for the SE simulations [132]. As expected, the SR-dependent material response increases in eroding strain and stress level by approximately 14%, as predicted by Equation 3-2.

Figure 5-3d exhibits the comparison under tensile loading for the analytical and SE calculations over ϵ_{eff}. Again, the maximum stress peaks do not coincide with the analytical evaluation due to initial numerical strain fluctuations. The rest of the curves are in good agreement with the analytical solution. Also, the diagram depicts the SR-dependency of the effective failure strain, which rises by the targeted 14%, whereas the stress level does not rise. Unexpectedly, the HR curve shows a more abrupt load reduction than the QS counterpart after the tensile strength limit is exceeded. The force fluctuations of the curve in the enlarged view indicate that this could be due to a temporary numerical instability in the HR model.

The necessary *MAT_058 entries, which are neither default values nor characterized values already specified in Chapter 3, are summarized in Table 5-1. Descriptions are in accordance with the LS-DYNA Keyword User's Manual [133].

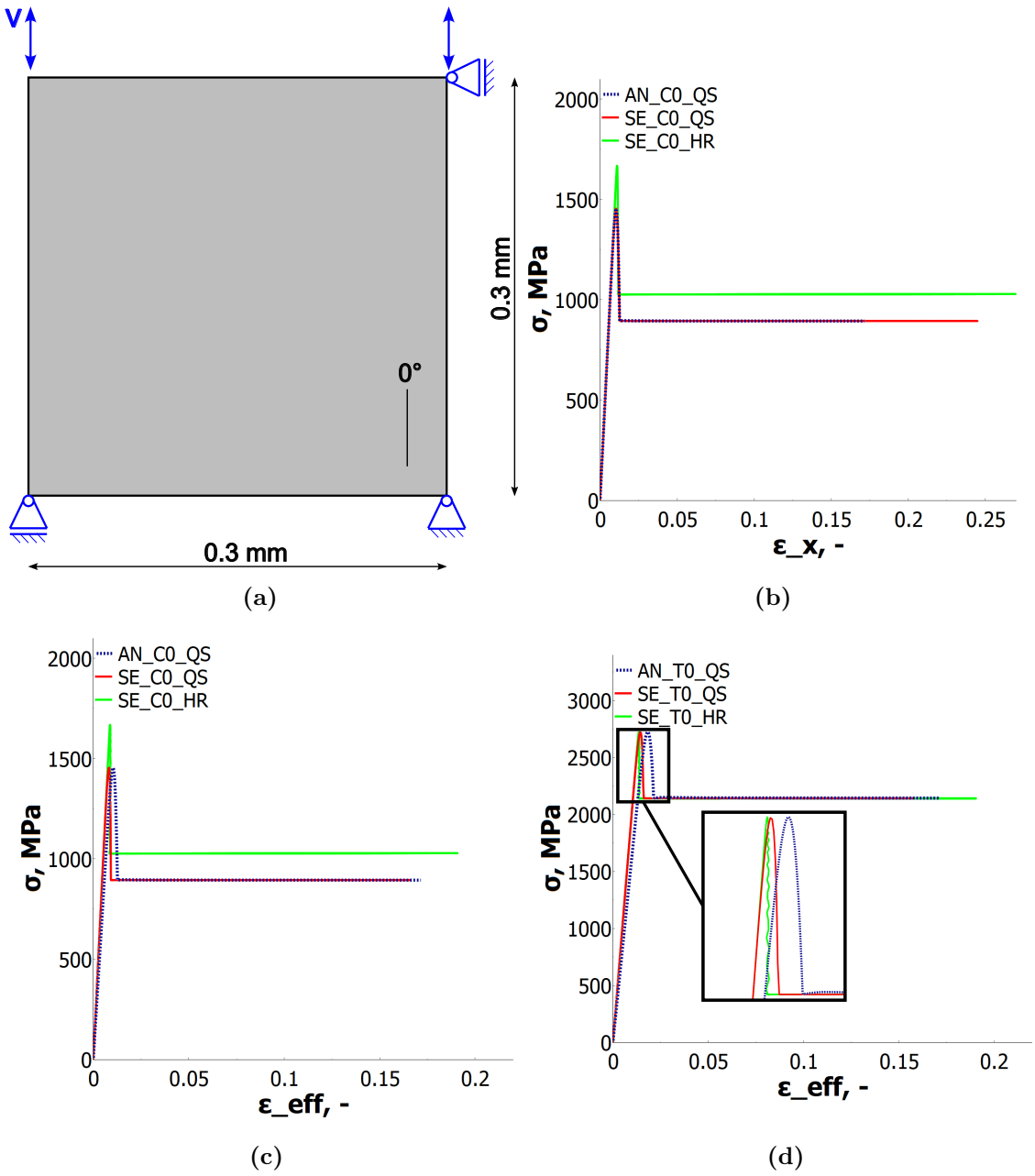

Fig. 5-3 (a) SE for tensile or compression simulation along fiber direction with an applied velocity of v = 1 mm/s. (b) SE compression (C0) stress curves over longitudinal strain ϵ_x with QS and HR material representation and analytical solution (AN). (c) SE compression stress curves over effective strain ϵ_{eff} with QS and HR material representation and analytical solution. (d) SE tension (T0) stress curves over effective strain ϵ_{eff} with QS and HR material representation and analytical solution.

Tab. 5-1 Additional *MAT_058 material card entries

Property	Value	Description	Source/explanation
RO	1.57 g/cm^3	Mass density	[106]
$TAU1$	80.0 MPa	Limit stress of the first slightly nonlinear part of the shear stress versus shear strain curve	[23]
GMS	0.0447	Engineering shear strain at shear strength	[23]
$ERODS$	-0.2	Maximum effective strain for element layer failure calculated from the full strain tensor	From DENC study
FS	-1	Failure surface definition	Faceted failure surface recommended for complete laminates
$SOFT$	1.0	Softening reduction factor for strength in the crash front	The value corresponds to no strain softening

Material cards adapted to 0.3 mm mesh size were integrated into the OHC and TTT crushing models, whereas the cards adapted to 2 mm were used for the tube crushing models. Appendix A.5 shows an example IM7/8552 QS material card as LS-DYNA Ascii input for an element size of 2 mm.

5.1.2 Interlaminar material representation

Theory of *MAT_240 and *CONTACT_..._TIEBREAK option 14

To model the out-of-plane behavior of the composite and to introduce delamination to the model, a cohesive zone model (CZM) was applied. In LS-DYNA, these models can be defined by CZEs or TIEBREAK contacts. *MAT_COHESIVE_-MIXED_MODE_ELASTOPLASTIC_RATE (*MAT_240) is a cohesive element formulation based on the work of Marzi et al. [134]. Also, the formulation is the underlying material model of *CONTACT_..._TIEBREAK option 14. TIEBREAK connections transfer compressive and tensile forces between paired parts and are subject to failure depending on the underlying material models. They are much more runtime-efficient compared to CDMs of cohesive zones and also more modeling-efficient compared to CZEs. TIEBREAK contacts are, therefore, frequently employed to represent the delamination behavior of composite parts or components attached to each other when adhesives are used. The TIEBREAK implementation was applied in

the SLMs with balanced ply clusters. During the evaluations, the approach was not transferable to DPMs as it led to instable contact responses after damage onset in the vicinity of the crack (see Figure 5-4). Even though the shown behavior was improved by switching from a reduced-integrated element formulation ($ELFORM = 2$) to a fully integrated element formulation ($ELFORM = 16$) [132], it was considered a risk for the simulation stability, which could easily be avoided. Therefore, CZEs were modeled to coincide with the neighboring nodes in the interface of two plies each for the 16S models instead. The CZM formulation of *MAT_240 could be used with largely identical settings as in the TIEBREAK definition: Interlaminar elastic properties required as input for the CZE modeling were additionally defined, and the cohesive element thickness was specified as the geometrical thickness ($THICK = t_\mathrm{e} = 0$). A description of the applied model of Marzi et al. in simplified bilinear form (trilinearity parameters $f_{\mathrm{g1}} = f_{\mathrm{g2}} = 0$), thus not considering plastic separation, is given in the following paragraphs [134].

Using the normal and tangential element separations u_{33}, u_{13}, and u_{23} in the integration points, the normal (peel) and tangential (shear) separations Δ_t and Δ_n are determined:

$$\Delta_n = \langle u_{33} \rangle, \text{ where } \langle u_{33} \rangle = \begin{cases} u_{33}, & if\ u_{33} > 0 \\ 0, & else \end{cases} \tag{5-8}$$

$$\Delta_t = \sqrt{u_{13}^2 + u_{23}^2} \tag{5-9}$$

The mixed-mode separation Δ_m is given by:

$$\Delta_m = \sqrt{\Delta_n^2 + \Delta_t^2} \tag{5-10}$$

An equivalent strain rate $\dot{\epsilon}_\mathrm{eq}$ is derived from the element separations in the integration points and the cohesive element thickness t_e to account for SR effects:

$$\dot{\epsilon}_{eq} = \frac{\sqrt{\dot{u}_{33}^2 + \dot{u}_{13}^2 + \dot{u}_{23}^2}}{t_e} \tag{5-11}$$

Yield stresses are considered rate-sensitive, whereas FTs are considered constant. The yield stresses under tension (T) and shear (S) as a function of the equivalent strain rates are determined by:

$$T(\dot{\epsilon}_{eq}) = T_0 + T_1 \cdot (ln\frac{\dot{\epsilon}_{eq}}{\dot{\epsilon}_T})^2 \tag{5-12}$$

$$S(\dot{\epsilon}_{eq}) = S_0 + S_1 \cdot (ln\frac{\dot{\epsilon}_{eq}}{\dot{\epsilon}_S})^2 \tag{5-13}$$

where an index 0 indicates a QS yield stress and an index 1 indicates the SR increase parameter of the corresponding yield stress. $\dot{\epsilon}_{\mathrm{T}}$ and $\dot{\epsilon}_{\mathrm{S}}$ denominate the equivalent strain rate at yield initiation to describe the rate dependency of the yield stresses in Mode I and II, respectively. All of these variables are parameters from the material card. The mixed-mode yield displacement is calculated from:

$$\delta_m = \delta_n \cdot \delta_t \cdot \sqrt{\frac{1+\beta^2}{\delta_t^2 + (\beta \cdot \delta_n)^2}}, \text{ where } \delta_n = \frac{T \cdot t_e}{E}, \ \delta_t = \frac{S \cdot t_e}{G}, \text{ and } \beta = \frac{\Delta_t}{\Delta_n} \tag{5-14}$$

Here, δ_{n} and δ_{t} represent the yield initiation displacement under peel and shear loading. β is the calculated loading mixed-mode ratio, whereas E is the Young's modulus and G the shear modulus of the cohesive as defined in the material card. Furthermore, the failure displacement δ_{mf} can be written as:

$$\delta_{mf} = \frac{2 \cdot G_{Ic} \cdot G_{IIc} \cdot t_e}{\delta_m \cdot (E \cdot G_{IIc} \cdot cos^2\gamma + G \cdot G_{Ic} \cdot sin^2\gamma)}, \text{ where } \gamma = arccos\frac{\Delta_n}{\Delta_m} \tag{5-15}$$

with G_{Ic} and G_{IIc} denominating the mode I and II FTs. Damage D within a time step is defined as:

$$D = max(\frac{\Delta_m - \delta_m}{\delta_{mf} - \delta_m}, \ D_{t_{i-1}}, \ 0) \tag{5-16}$$

where $D_{\mathrm{t_{i-1}}}$ denominates the damage variable from the prior time step. The element fails in the corresponding integration point when total damage ($D = 1$) is reached. Finally, the element stresses σ_{ij} are obtained from:

$$\sigma_{33} = \begin{cases} \frac{E \cdot (1-D) \cdot u_{33}}{t_e}, & if \ u_{33} > 0 \\ \frac{E \cdot u_{33}}{t_e}, & else \end{cases} \tag{5-17}$$

$$\sigma_{13} = \frac{G \cdot (1-D) \cdot u_{13}}{t_e} \tag{5-18}$$

$$\sigma_{23} = \frac{G \cdot (1-D) \cdot u_{23}}{t_e} \tag{5-19}$$

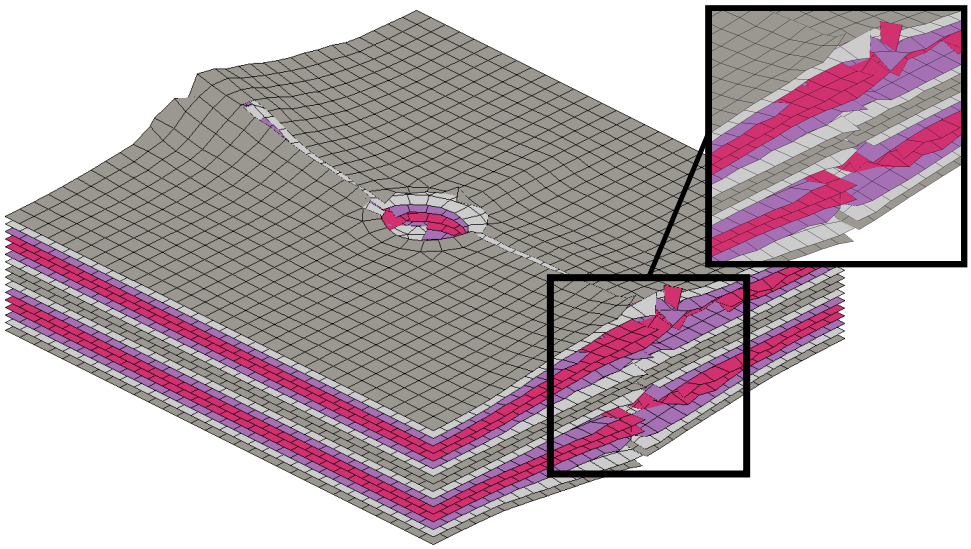

Fig. 5-4 OHC DPM model with TIEBREAK and ELFORM 2 exhibiting unstable contact behavior in the area of the crack.

Evaluation of cohesive zone models

Prior to any notched coupon or crushing simulation, numerical studies had to be performed on the interlaminar crack propagation of the material. This step is necessary because millimeter-scale element lengths can evoke abrupt and unphysical delamination failure in cohesive zone models (CZM) ruled by a traction-separation law. For crack opening mode I and mode II, the following criteria for critical element lengths were defined by Smith and Massabò et al., assuming a linear softening law and slender specimen:

Mode I ([135]):

$$l_{\mathrm{cz}} = N_{\mathrm{e}} l_{\mathrm{e}} = \left(\frac{E_{33} G_{33\mathrm{c,T}}}{S_{33}^2}\right)^{\frac{1}{4}} h^{\frac{3}{4}} \tag{5-20}$$

Mode II ([136]):

$$l_{\mathrm{cz}} = N_{\mathrm{e}} l_{\mathrm{e}} = \sqrt{\frac{G_{13} G_{13\mathrm{c}}}{S_{13}^2} h} \tag{5-21}$$

where l_{cz} is the length of the cohesive fracture zone consisting of N_{e} elements with a length of l_{e} each. E_{33} represents the out-of-plane tensile modulus and G_{13} the out-of-plane shear modulus along the fibers, whereas $G_{33\mathrm{c}}$ and $G_{13\mathrm{c}}$ represent the interlaminar FT. S_{33} and S_{13} are the interlaminar tensile strength and shear strength along the fiber direction. h stands for the specimen height and is much smaller than the crack length.

To obtain accurate delamination failure in a CZM, different authors recommend discretizing the cohesive zone with 2 to 10 elements [137, 138]. For IM7/8552 and an assumed $N_e = 2$ the above expressions yield critical element lengths of 0.54 mm for mode I and 0.58 mm for mode II. These lengths are too small to be used in the investigated composite geometries, e.g., the crushing tubes with 2 mm element size. An adaption of the out-of-plane strengths can stabilize the delamination process in FE meshes of this scale [139]. It should be noted that Daniel et al. recently investigated a novel CZM to increase the required cohesive element size to a more applicable length [140]. Since this model was not available for this thesis, strength calibrations were essential to the present approach.

Based on the experimental results of Czabaj and Ratcliffe along with O'Brien et al., QS double-cantilever beam (DCB) and end-notched flexure (ENF) simulations with a nominal mesh dimension of 0.3 mm and 2.0 mm were set up to evaluate and reduce the interlaminar strength properties as far as necessary [116, 118]. The DCB experiments of Czabaj and Ratcliffe obtained by application of test standard ASTM D5528 were reproduced numerically with the specimen dimensions specified in Figure 5-5a [141]. The load was applied into the free shell edges via rigid body elements representing end tabs and a scaled prescribed velocity of 30 mm/s. The ENF experiments of O'Brien et al. obtained by application of test standard ASTM D7905(M) were set up numerically with the specimen dimensions specified in Figure 5-5b [142]. The specimen was supported by two rigid bodies at the same distance from the outer edges. The load was applied centrally with another rigid body at a scaled prescribed velocity of 80 mm/s. Load introduction via rigid bodies had proven superior to physical modeling of the cylindrical bearings for the 0.3 mm variants. For the 2 mm variants, all supports were modeled with cylindrical beam elements. The results of the model calibrations are shown in Figure 5-6 for DCB and Figure 5-7 for ENF, respectively.

All DCB simulations can capture the initial load increase from the experiments. At around 20 N force, the 2 mm mesh variants exhibit a uniformly decreased stiffness compared to the experimental curves before they reach the maximum force in the region of the fatigue-precracked specimen around 70 N. The 0.3 mm variant reaches the characteristic load peak of the experiments with a Teflon insert for crack initiation. Upon failure of the cohesive zone, all simulation curves decrease along the experimental curves. In the case of the studies with 2 mm element length, this is thanks to a drastic reduction of the interlaminar tensile strength S_{33} to 7 MPa. As expected, a mesh size of 0.3 mm is sufficiently small to reproduce the experimental material response without the necessity to reduce the strength. As shown in Figure 5-8a, this fine-meshed model can even reproduce a quasi-parabolic crack front morphology over the width of the specimen as described

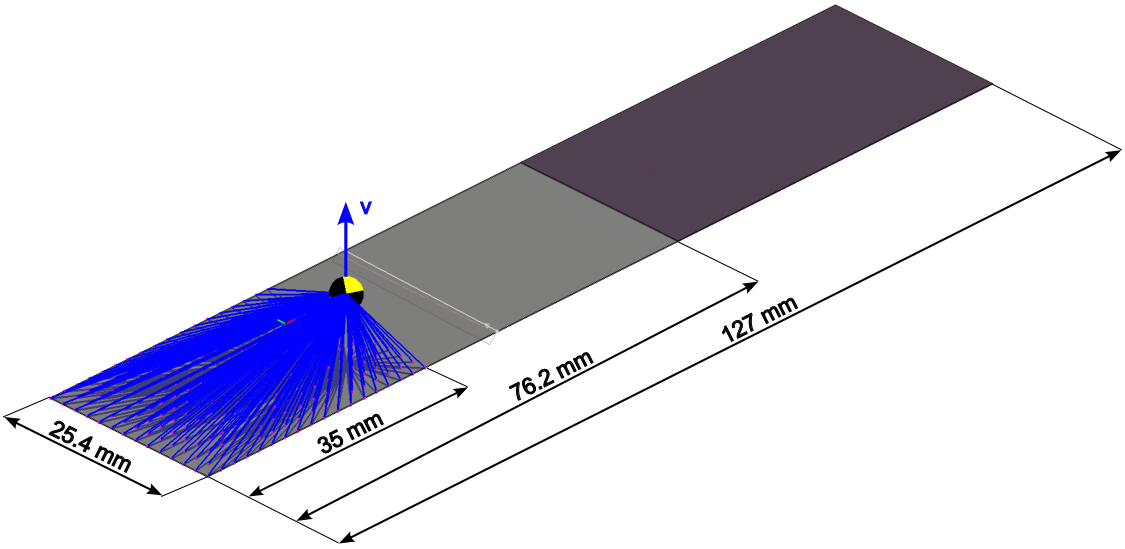

(a)

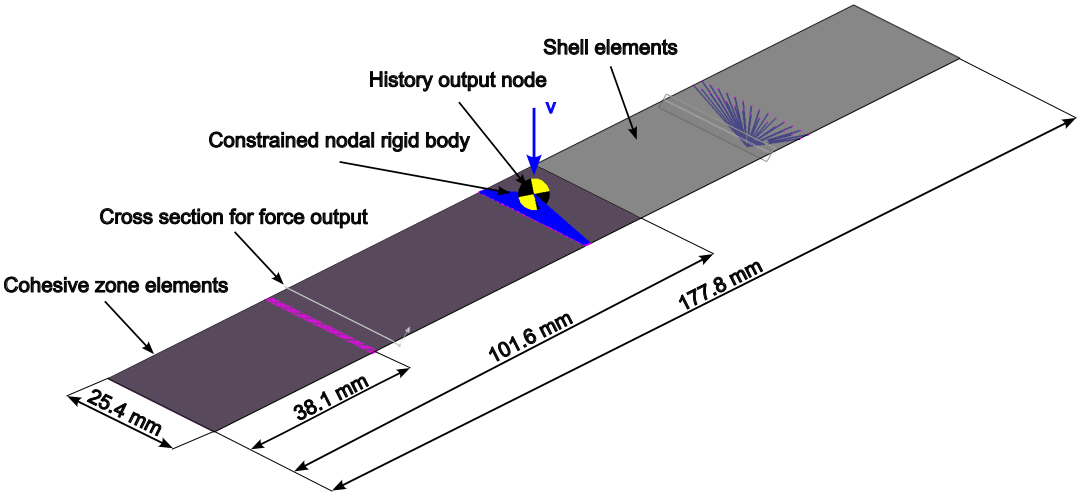

(b)

Fig. 5-5 ISO-views of 0.3 mm (a) DCB and (b) ENF FE model with dimensions using semi-transparency to make the CZE visible. A specimen thickness of 2 mm and an out-of-plane length of 0.125 mm was applied for the purple cohesive elements.

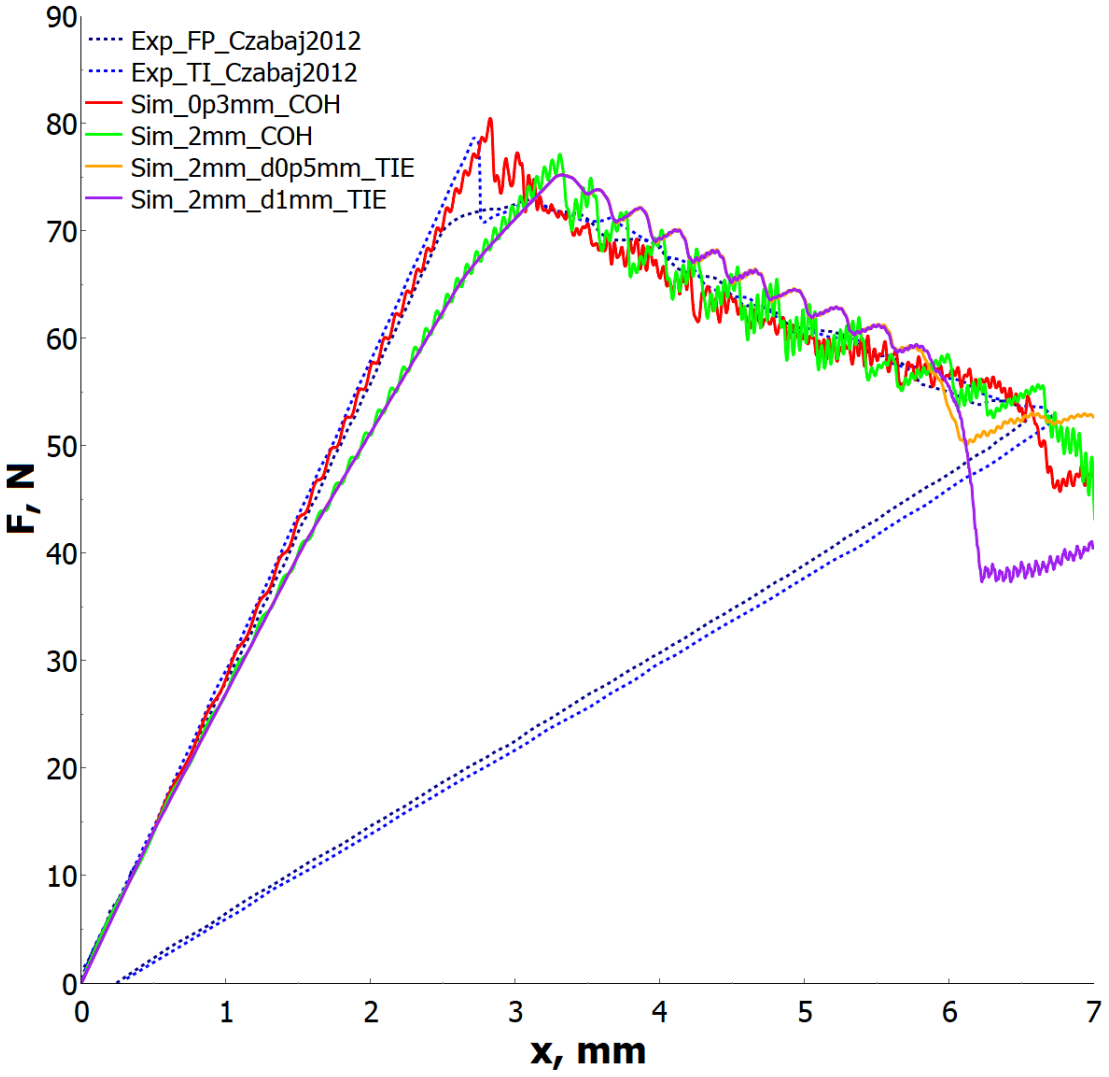

Fig. 5-6 Force over displacement of the DCB experiments conducted by Czabaj and Ratcliffe and four DCB simulations with varying mesh size (0p3mm / 2mm), shell gap (d0p5mm / d1mm) and CZM representation (COH / TIE) [116]. Experimental curves are given for specimens with fatigue precrack (FP) and Teflon insert (TI).

by Møberg et al. [143]. Czabaj and Ratcliffe reported the same effect from their fatigue precracked specimens [116]. FT G_{33c} had to be increased by 22% to 0.28 N/mm for all simulations compared to the experimental property determined with Teflon inserts to obtain the maximum force observed. Apart from the discretization, neither the CZM representation nor the layer distance seem to significantly affect the numerical failure under crack growth mode I.

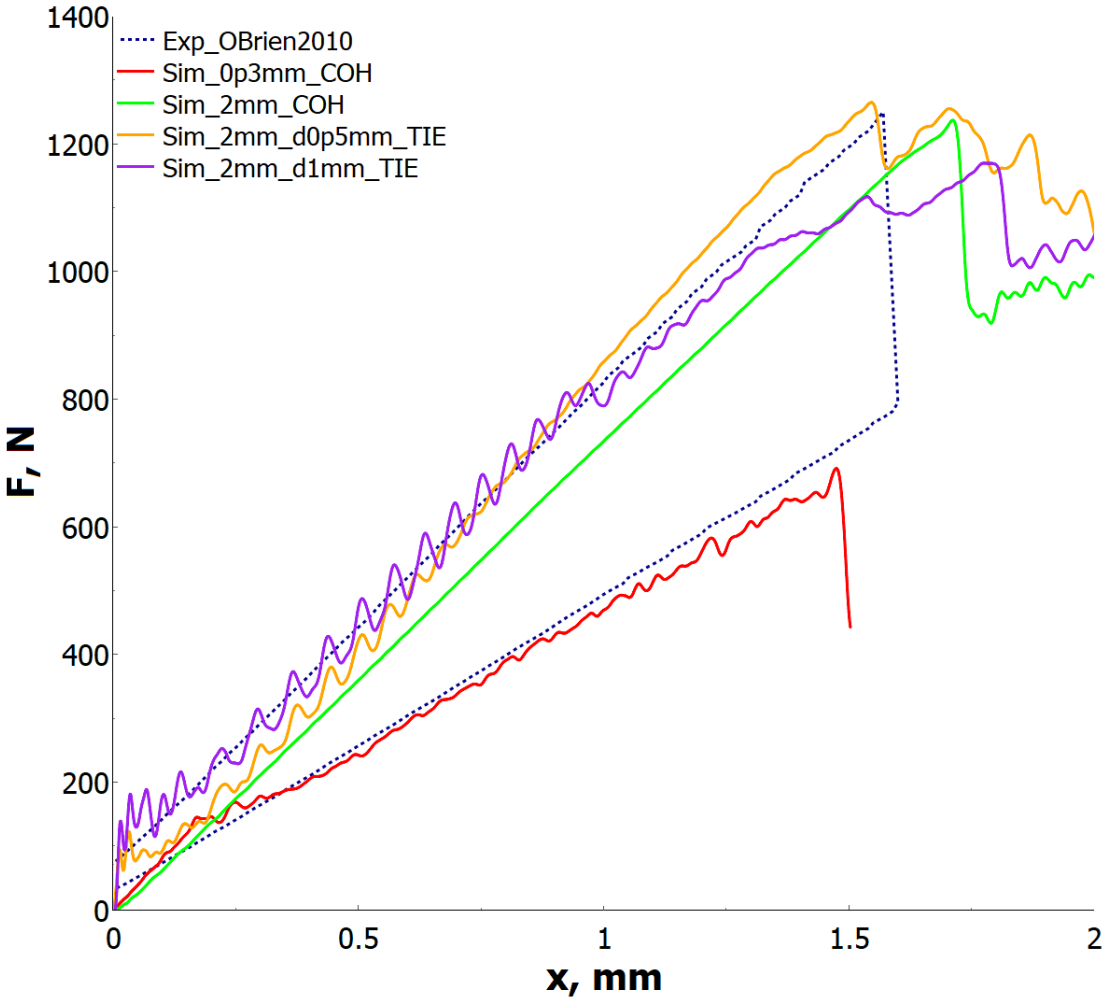

Fig. 5-7 Force over displacement of a non-precracked ENF experiment conducted by O'Brien et al. and four ENF simulations with varying mesh size (0p3mm/2mm), shell gaps (d0p5mm/d1mm) and CZM representation (COH/TIE) [118].

The ENF 2 mm mesh variants closely resemble the experimental curve, above all with the cohesive element representation (COH). The TIEBREAK formulation (TIE) has a visible influence, which leads to high-frequent oscillations in the contact initiation phase of the simulation. Unexpectedly, no strength adaption was necessary for any of the CZM descriptions to reach the maximum load of about 1.300 N.

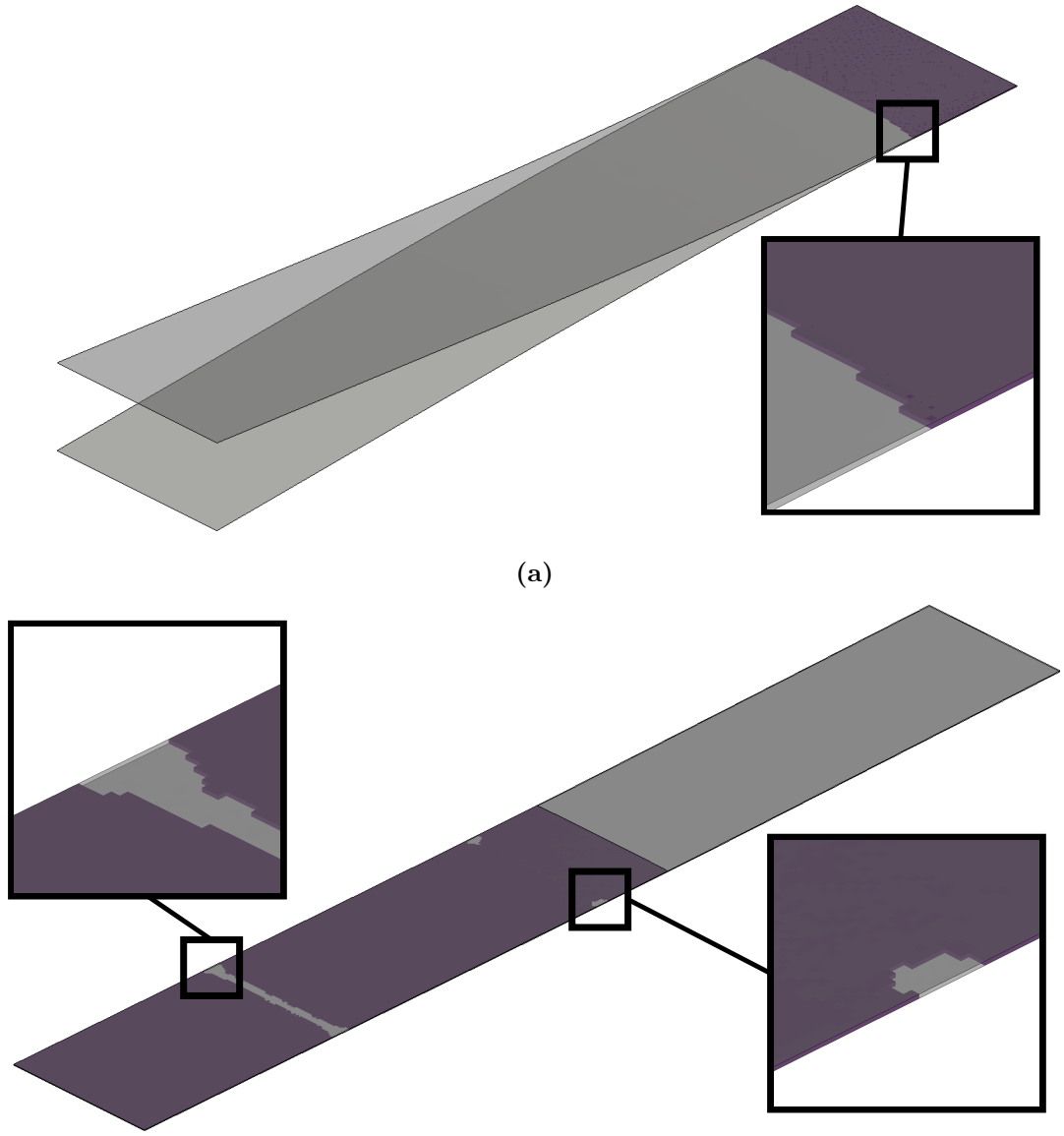

(a)

(b)

Fig. 5-8 ISO-views of 0.3 mm (a) DCB simulation in the final state (b) ENF simulation after failure in the vicinity of the load introductions using semi-transparency to make the CZE visible.

Thus, the nominal value of the interlaminar shear strength S_{13} could be applied, but again, the FT had to be increased uniformly: in the case of mode II crack opening by 30%, leading to $G_{13c} = 1.6$ N/mm. The 0.3 mm variant follows the load increase of the experiment, and the 2 mm variants up to approximately 150 N load. The following reduction in the curve gradient is caused by failing elements in the load introduction area of the rigid bodies, as depicted in Figure 5-8b. This reduction is a purely numerical effect, which could not be resolved due to the variant runtime of more than one day on several HPC cores. Still, the existing results can be further evaluated toward the experiment: Firstly, the curve increase after the kink point is comparable to the unloading path of the experiment. Moreover, the intended failure below the impactor is initiated at about 1.5 mm displacement, close to the experimental maximum displacement.

Table 5-2 yields the final overview of the interlaminar material properties derived from the numerical studies. The 0.3 mm parameters were incorporated in the OHC and TTT crushing models, whereas the 2 mm parameters were used for the tube crushing models. TIEBREAK formulations were applied in the SLMs, and *MAT_240 CZEs were defined in the DPMs to account for ply debonding. 2 mm material cards of the two interlaminar formulations also including SR-dependencies adapted to the regressions from [108] can be found in Appendix A.5.

Tab. 5-2 Crack opening mode I and II damage properties of IM7/8552 for application in CZM.

Element size	Crack opening mode	Strength	FT
2 mm	mode I	7 MPa	0.28 N/mm
	mode II	95.8 MPa	1.6 N/mm
0.3 mm	mode I	101.4 MPa	0.28 N/mm
	mode II	95.8 MPa	1.6 N/mm

5.2 Open-hole compression models

As already shown in Figure 5-1, OHC specimens were meshed as single shells (1S) with nominal element lengths of 0.3 mm, 0.5 mm, and 0.75 mm. A uniform, mostly quadratic, and symmetric mesh was created with one ring of elements around the hole. *PART_COMPOSITE formulation and $LAMSHT = 3$ were used to allow for the laminated shell theory. The regularization investigation, whose findings were already described in Section 5.1.1, was the only study that used the coarser meshes. The 0.3 mm mesh was selected for the OHC validation because it was anticipated to produce sufficiently realistic fracture behavior due to the fine discretization but at tolerable simulation runtimes. The 1S model was intended to build a simplified

baseline of the models without considering delamination. To allow for ply debonding, models with four balanced sub-laminate shells (4S) and 16 stacked single-ply shells (16S) were created. The 16S model employed *PART definitions with three through-thickness integration points at pre-defined Gauss positions to accurately account for bending behavior in each layer. Reduced integrated element formulation $ELFORM$ 2 was used for 1S and 4S setups to provide runtime-efficient models. Due to the otherwise unphysical hourglassing of the elements impacted by the crack, 16S configurations had to be run with a fully integrated element formulation, such as $ELFORM$ 16. Also, the number of integration points through the thickness (NIP = 3) had to be increased. Both measures were taken to improve the deformation and failure behavior, even though they reduced the runtime comparability. Cohesive elements were used for the 16S model instead of the TIEBREAK formulation due to numerical stability concerns, which were already described in Section 5.1.2. These model adaptions were transferred to the TTT and tube crushing simulations likewise. In order to attain the mean SR from the HR experiments, one specimen edge was constrained for the HR simulations, and after a brief acceleration period, a uniform velocity of 0.725 m/s was applied to the opposite edge. This velocity was used for the QS simulations as well. In Figure 5-9, all OHC simulation models and boundary conditions are shown.

Tab. 5-3 Simulation plan for the OHC validation study.

Variation	Values
Stack modeling	1S / 4S / 16S
Strain rate	QS / HR

The models consisted of 888 elements for the 1S, 3,552 elements for the 4S, and 27,528 elements for the 16S, respectively. The summary of the simulation iterations for the OHC validation may be found in Table 5-3. As can be seen, three modeling variants were examined in two SR domains each.

The post-processing of the OHC simulations was carried out following the OHC experiments. The underlying success criteria of the simulations also used by Justusson et al. were defined by the Composite Materials Handbook-17 (CMH-17) Crashworthiness Working Group (CWG) and are presented in detail in Appendix A.6 [144]. Also, the failure patterns and simulation runtimes underwent an evaluation.

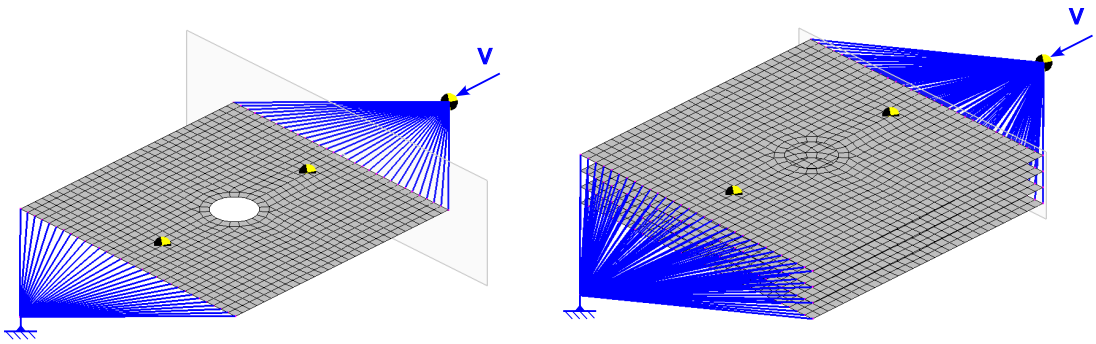

(a) (b)

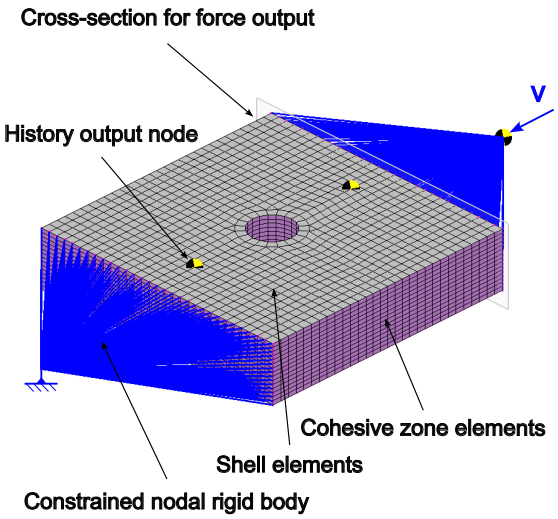

(c)

Fig. 5-9 (a) OHC 1S model, (b) 4S model, and (c) 16S model with a description of constituents, boundary conditions, and output entities. Shell thicknesses and contacts are not shown in the figures.

5.3 Crushing models of triangular through-thickness trigger specimens

Both the inter- and intralaminar modeling were aligned with the OHC simulations. Thus, a 0.3 mm mesh was used along with through-thickness discretizations as SSM (1S), SLM (4S), and DPM (16S). Rectangular quadrilateral FE meshes tend to fail non-continuously under axial crush loading [13, 40, 42]. Along with unstructured meshes and node scattering, literature studies suggest oblique meshes to approach the issue [13, 43, 45]. To evaluate the influence of the element shape on the present coupon geometry, 4S models were set up with a mixed mesh, mainly consisting of square-shaped elements and a purely rhomboidal mesh (see Figure 5-10a and Figure 5-10b). As shown in Figure 5-10c, the largely rectangular mesh produces non-physical force oscillations, triggering a premature loss of the coupon's load bearing capacity due to delamination. Therefore, the rhomboid mesh was used throughout all further TTT simulations.

For the MR models, calibrated initiation FTs G_{33c} and G_{13c} were deemed appropriate, since rapid and unstable crack propagation was observed in the experiments. This behavior was also reported in the DCB experiments by Czabaj and Ratcliffe [116]. The lower propagation values $G_{33c,PV} = 0.201$ N/mm and $G_{13c,PV} = 0.773$ N/mm were applied uniformly throughout the HR models as steady crack propagation was observed in the corresponding experiments (see Figure A-4).

Experimental settings were simplified as far as feasible in the numerical models to achieve efficient models and a good runtime comparability: the impactor was represented by a *MAT_RIGID plate with either an impact mass and *INITIAL_VELOCITY of 4.56 m/s (HR) or a *PRESCRIBED_MOTION definition (MR). The validity of the model reduction will be proven in Section 6.2.3. The MR setup used two configurations for the 4S models: (a) a constant but elevated velocity of 1 m/s in comparison to the tests and (b) an original velocity of 1 mm/s with strain-rate-dependent implementation and no mass scaling. The latter had demonstrated to affect contact between impactor and specimen at a mass scaling level adequate to significantly shorten the runtime. Only the free length of the specimen was modeled with the fixture as *CONSTRAINED_NODAL_RIGID_BODY. The symmetry plane spanned by the impact axis and the through-thickness direction of the specimen was used to divide all entities of the generated models in half to increase runtime efficiency. To provide physical boundary constraints, selected rotational and translational degrees of freedom were limited in the symmetry plane. Also, the gravitational load of the impactors was taken into consideration. The model setups are displayed in Figure 5-11.

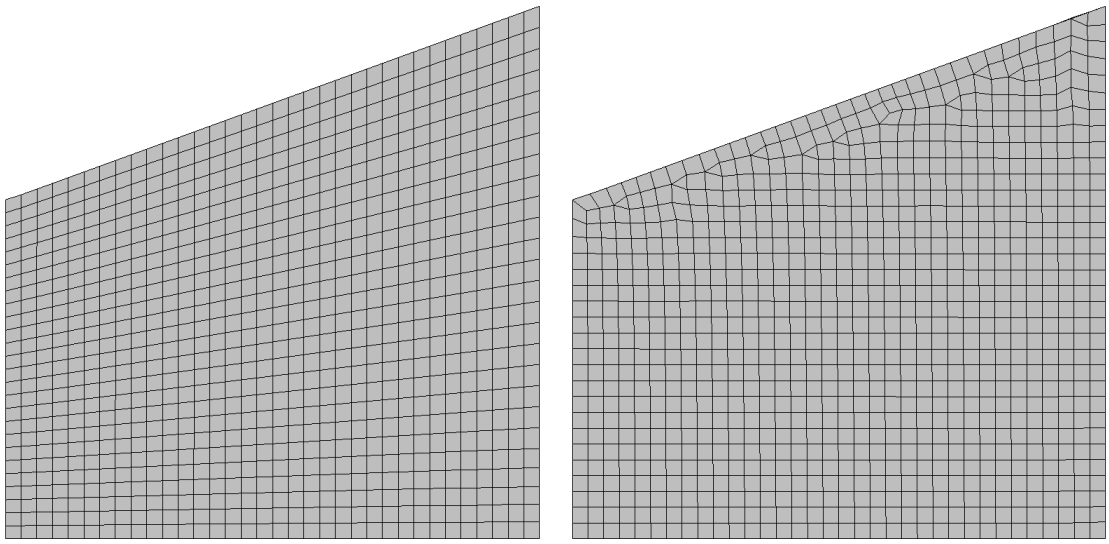

(a) (b)

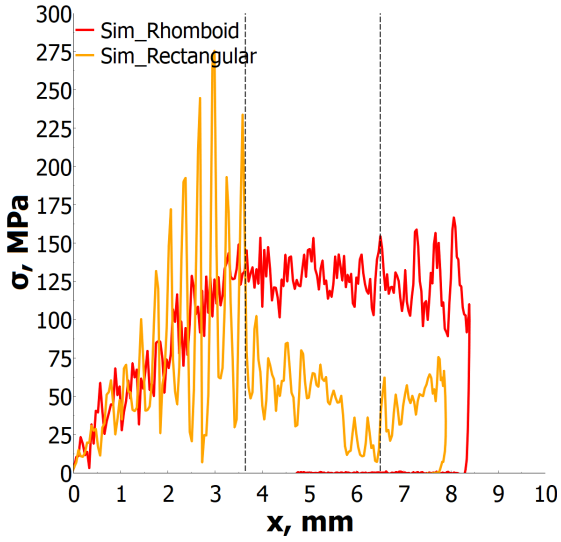

(c)

Fig. 5-10 (a) Rhomboidal 0.3 mm mesh and (b) largely rectangular 0.3 mm mesh. (c) Stress-strain response of TTT simulations using the two meshes.

The MR models consisted of 1,835 elements for the 1S, 3,552 elements for the 4S, and 29,098 elements for the 16S, respectively. The conducted simulations are presented in Table 5-4. In total, seven variants were examined in two SR domains.

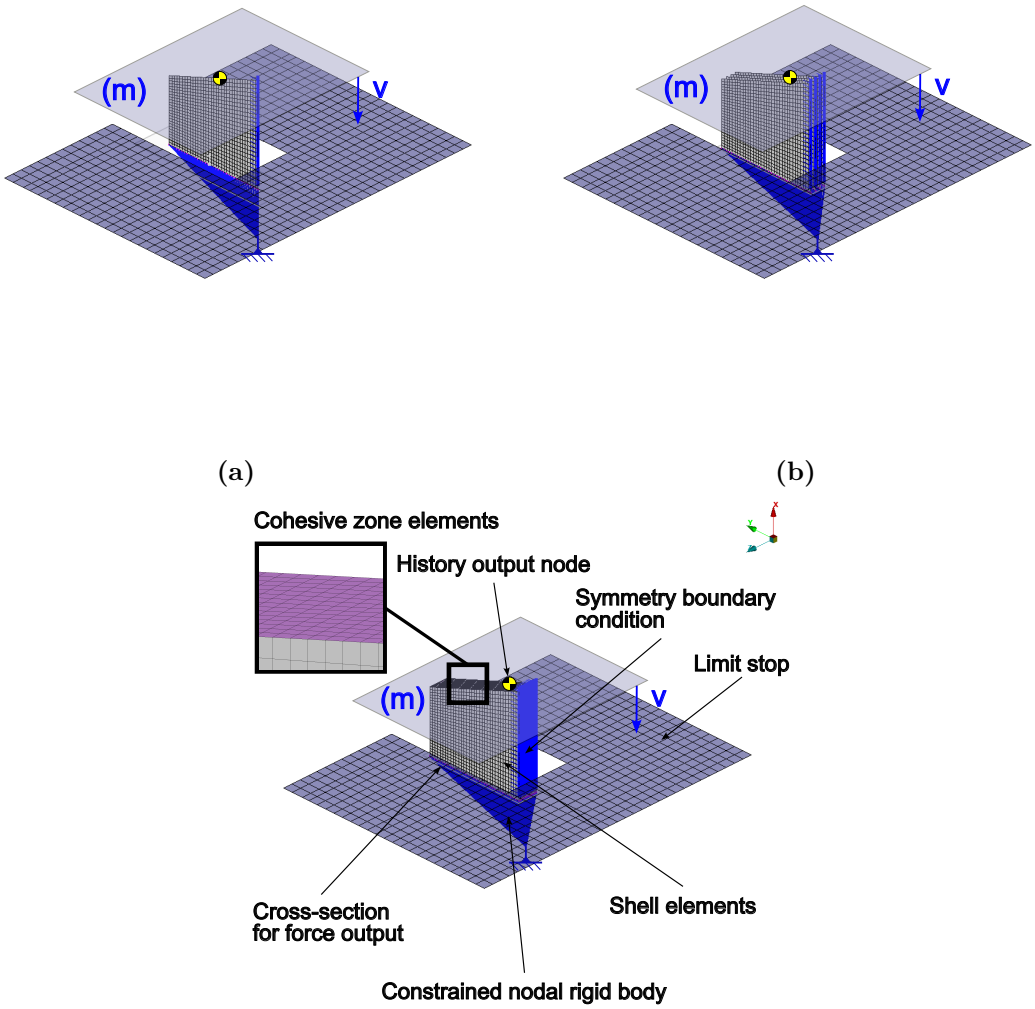

Fig. 5-11 (a) TTT 1S model, (b) 4S model, and (c) 16S model with a description of constituents, boundary conditions, and output entities. Shell thicknesses and contacts are not shown in the figures.

The post-processing of the TTT simulations was carried out following the TTT experiments. The simulations facilitated an evaluation of the failure patterns and breakdowns of the energy absorption mechanisms. Again, the CMH-17 CWG simulation success criteria were applied (see Appendix A.6).

Tab. 5-4 Simulation plan for the TTT crushing study.

Variation	Values
Stack modeling	1S / 4S / 16S
Velocity	MR(_1mmps / _1mps) / HR

5.4 Tube crushing models

The rectangular tube geometries from ORNL used in this work were meshed with homogeneous, slightly rhomboid elements to face mesh-induced force oscillations. The draft angle of the profiles was ignored in the numerical models. The crushing tube geometry with a tulip trigger was used to generate a single-shell (1S) 2 mm mesh with a "thread pitch" of one element row (see Figure 5-12c). The mesh was then copied and offset to produce an SLM with two balanced sub-laminate shells (2S) and a DPM with 16 stacked shells (16S). To eliminate mesh-evoked out-of-axis bending moments that the author had observed at the 1S tubes, the second 2S shell was rotated 180 degrees clockwise around the longitudinal axis. The rotation was not applied to the 16S models because the mesh had to be uniform to connect the cohesive elements with coincident nodes. The material formulations and settings used in the OHC and TTT investigations were transferred to the tube crushing models. Table 5-5 summarizes the simulation plan for the crushing component studies with three modeling variants at two SR domains each. Figure 5-12 displays the tube model setups. The models comprised 12,328 elements for the 1S, 22,156 elements for the 2S, and 147,420 elements for the 16S, respectively.

Tab. 5-5 Simulation plan for the tube crushing study.

Variation	Values
Stack modeling	1S / 2S / 16S
Velocity	QS / HR

Single-point constraints were used to completely restrain the motion of the nodes around the edge of the untriggered specimen side. A flat and rigid impactor was impinged with the identical transient velocity profile in all configurations determined from experiment 46B by ORNL (see Figure 5-12d). To prevent sticking effects noticed during early-phase studies with a friction coefficient of 0.4, suggested by other authors [145, 146], a global friction coefficient of 0.3, as proposed by Feindler, was introduced [50].

Again, the CMH-17 CWG simulation quality criteria were employed (see Appendix A.6) and the energy absorbing processes were numerically assessed for the

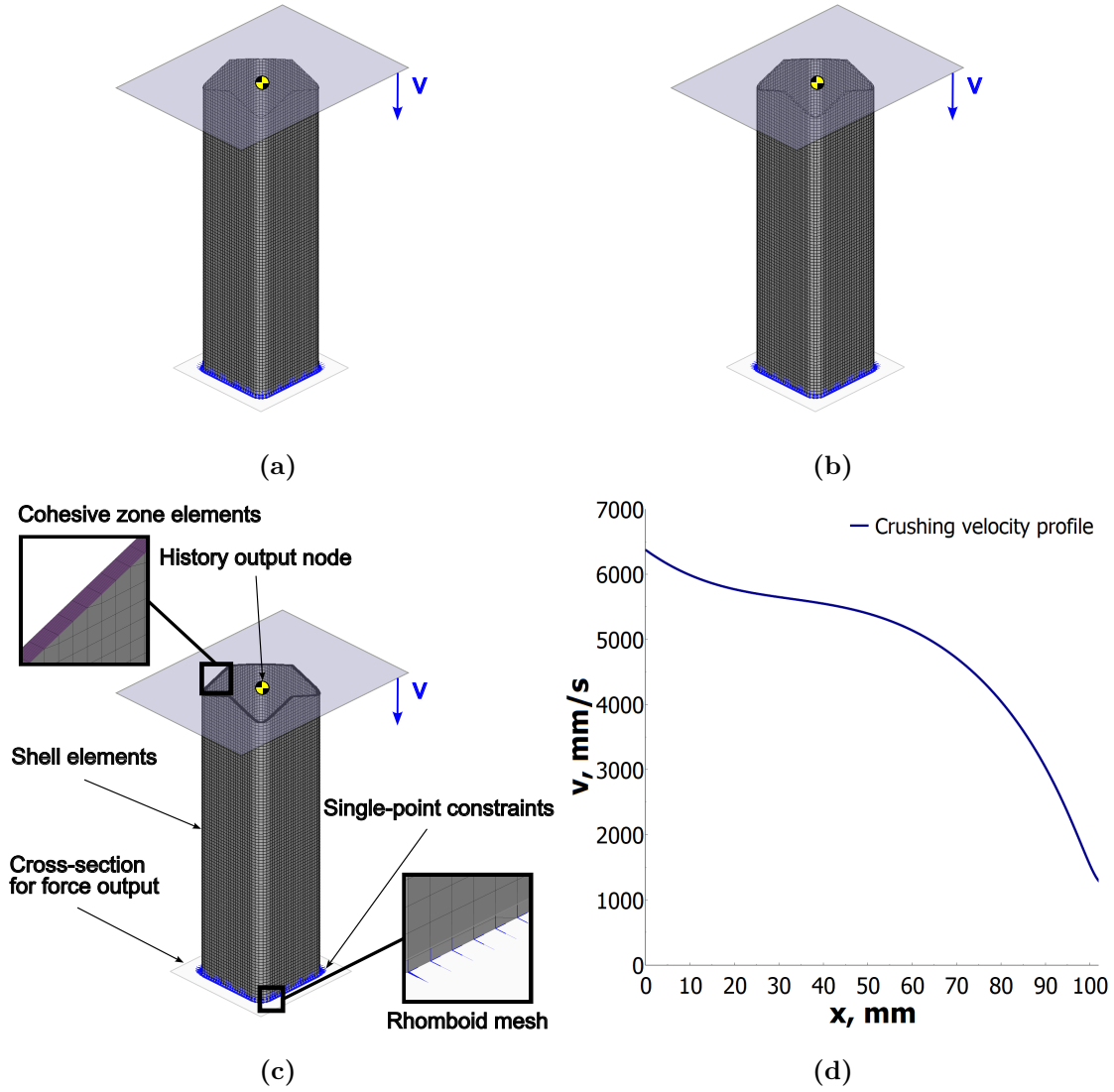

Fig. 5-12 (a) Tube 1S model, (b) 2S model, and (c) 16S model with a description of constituents, boundary conditions, and output entities. Shell thicknesses and contacts are not shown in the figures. Subfigure (d) shows the crushing velocity profile derived from experiment 46B.

simulations. In addition, the failure patterns in the simulations were compared with footage from the tube crushing experiments. Recordings of the experiments were available for the HR configuration. However, only a picture of a QS specimen after the experiment was provided by Courteau [124].

6 Result overview and numerical validation

As for the experiments and numerical methodology, it should be noticed that parts of the following results have been published previously by Pohl et al. [107, 121]. However, several model evaluations, e.g., on the DPM OHC failure behavior, were refined, and a global comparison of the models was added in this thesis.

6.1 Open-hole compression experiments and simulations

6.1.1 Quasi-static domain

Figure 6-1 shows the results of the OHC QS simulations and experiments with a characteristic linear stress increase until strength is reached. Upon failure, a linear load drop indicates an insufficient temporal resolution of the failure process, as the high-speed event could not be captured by the employed digital image correlation (DIC) system. The expected failure mode was visible in all experiments, with centered crack initiation at the hole. One specimen was excluded from the study because of a signal loss during the measurement. Nonetheless, as can be seen in Table 6-1, the measured initial stiffness, strength, and fracture strain exhibit a low standard deviation (STDV) and coefficient of variation (CV).

Figure 6-2, Figure 6-3, and Figure 6-4 show the intra- and interlaminar failure patterns in the three outer layers as well as up to three primarily affected interfaces between two sub-laminates (4S) or single-layer shells (16S). Failure is demonstrated prior to the first element's deletion (initiation) and prior to the first element's deletion at the specimen's outer edge, or in the last frame of the fringe output (final).

The anticipated notch-driven failure mode from the experiments is present in all QS simulations. Their rotation-symmetric damage pattern can be seen as an artifact of the discretization. The 1S_QS configuration exceeds the observed initial stiffness, maximum stress level, and strain upon fracture in the stress-strain diagram (see Figure 6-1 and Table 6-1). This overestimation occurs because the modeling strategy does not support the interlaminar elastic compliance and delamination failure.

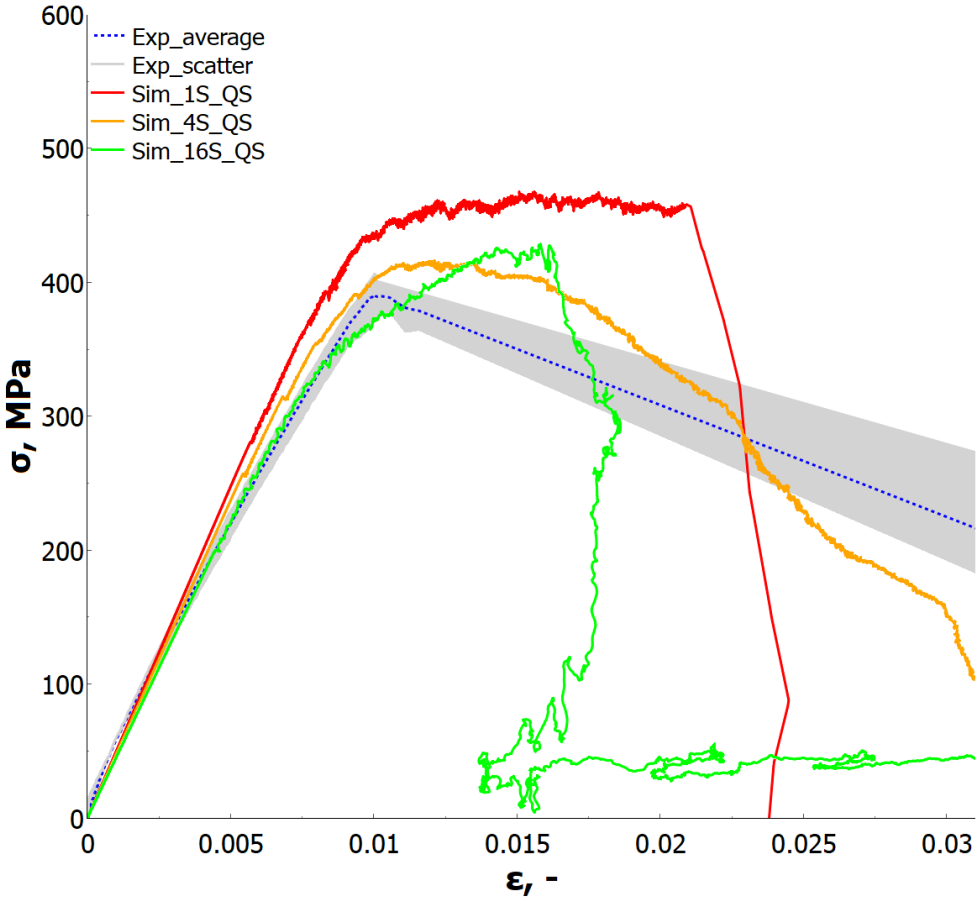

Fig. 6-1 Comparison of stress-strain average and scatter band from OHC_QS experiments with the corresponding numerical variants 1S, 4S, and 16S.

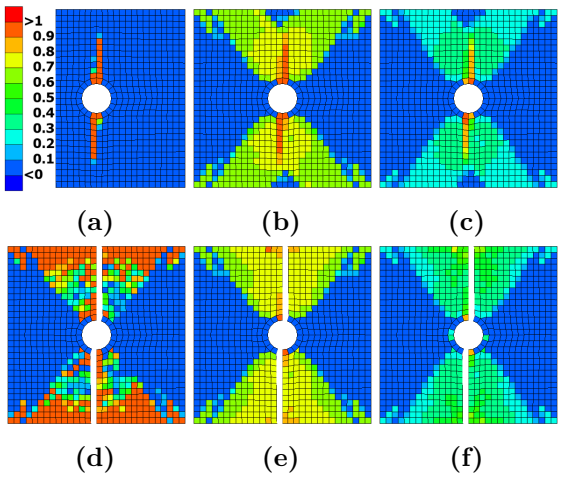

Fig. 6-2 Damage pattern of the 1S_QS model: initiation (a) 90° layer, (b) 0° layer, (c) 45° layer; final (d) 90° layer, (e) 0° layer, (f) 45° layer

The significance of delamination for the 4S_QS configuration is illustrated by comparing the damage patterns of Figure 6-2 and Figure 6-3. The heavily loaded 0° layer shows a scattered damage pattern in this simulation. Following the onset of damage at the hole, the specimen experiences two-sided through-thickness buckling ("blow-up"), which results in complete delamination in the considered outer interface. Nonetheless, the initial stiffness and strength agree well with the experiments. Only the failure strain is overrated, as can be seen in Figure 6-1 and Table 6-1. The comparison of Figure 6-5a and Figure 6-5b reveals that the strain fields upon maximum force are similar for the 4S simulation and the experiments. Still, the highly strained area is more extended in the simulation.

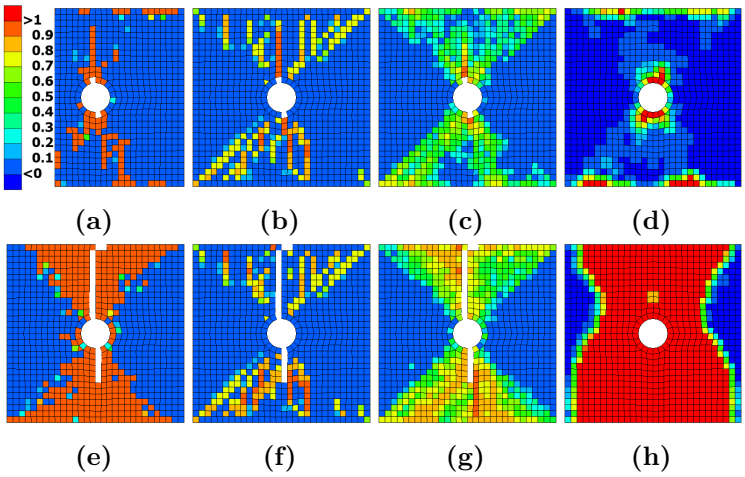

Fig. 6-3 Damage pattern of the 4S_QS model: initiation (a) 90° layer, (b) 0° layer, (c) 45° layer, (d) delamination outer to inner shell; final (e) 90° layer, (f) 0° layer, (g) 45° layer, (h) delamination of outer to inner shell

The 16S_QS configuration in Figure 6-4 also exhibits the two-sided buckling of the 4S_QS configuration. Delamination failure results in incomplete transverse fracture of the outer 0° layer. It should be noted that excessively damaged cohesive elements are deleted from the 16S_QS fringe plot instead of remaining as fully damaged elements. The stress-strain characteristic shows an underestimation of stiffness prior to achieving maximum stress and an overestimation of the fracture strain, whereas the initial stiffness and strength of the model agree well with the experiments (see Figure 6-1 and Table 6-1). Also, a more abrupt load drop occurs in the 16S model compared to the other simulations, which is a more realistic scenario. Other than Pohl et al. stated, premature intralaminar damage of the 0° plies was identified as the primary driver for the stiffness deviation [107]. This behavior is intrinsic to the softening characteristic of *MAT_058 and, therefore, cannot be eradicated. Xue and Kirane also reported a growth of the fracture process zone in their notched numerical specimens due to the plateau region in a sigmoidal softening law when compared to, e.g., a linear softening law [131]. Their sigmoidal softening

law compares well to the damage characteristic of *MAT_058. As shown above, the softening law affects the 4S simulation to a lesser extent than the 16S variant. This difference can be explained with the classical lamination theory applied in the shell elements: a cluster of four plies with the chosen orientations $90/0/\pm 45$ creates unsymmetric but balanced laminate shells with isotropic in-plane stiffnesses. At damage onset and assuming no delamination failure, neighboring plies in the cluster will support the damaged ply and increase its residual stiffness, reducing the excessive crack propagation of *MAT_058 as seen in the 16S variant.

To complement the analysis, Figure 6-5a displays the visible strain field on a representative OHC specimen before final failure compared to the 16S simulation. The highly strained area is very localized in the experiments, extending from the hole to the outer edges in the simulation (see Figure 6-5c). Thus, the strain field supports the above observations on the premature damage in the model.

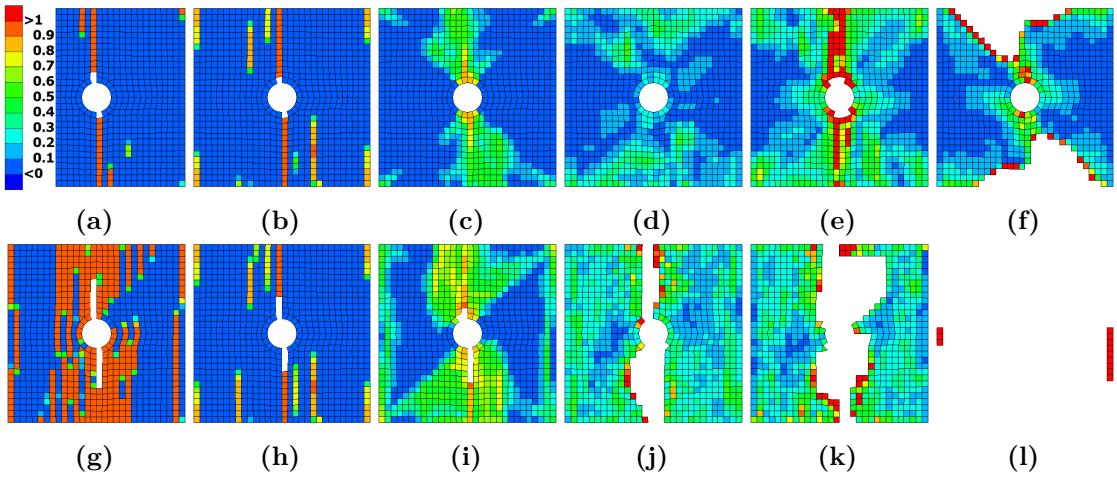

Fig. 6-4 Damage pattern of the 16S_QS model: initiation (a) 90° layer, (b) 0° layer, (c) 45° layer, (d) delamination 90°- to 0° layer, (e) delamination 0° to +45° layer, (f) delamination +45°- to -45° layer; final (g) 90° layer, (h) 0° layer, (i) 45° layer, (j) delamination 90°- to 0° layer, (k) delamination 0° to +45° layer, (l) delamination +45°- to -45° layer

In Table 6-1, the simulation results are summarized and evaluated toward the average value of the experiments following CMH-17 CWG.

6.1.2 High-rate domain

The stress-strain diagram of the OHC HR simulations and experiments is presented in Figure 6-6. Again, stress increases until the failure strength is reached and the load drops at very inhomogeneous rates in the different samples. Once more, this can be explained by the DIC system, which is not able to account for the high-speed character of the failure process. Every experiment showed the anticipated failure mode, which started with a central crack at the hole. The analysis considered

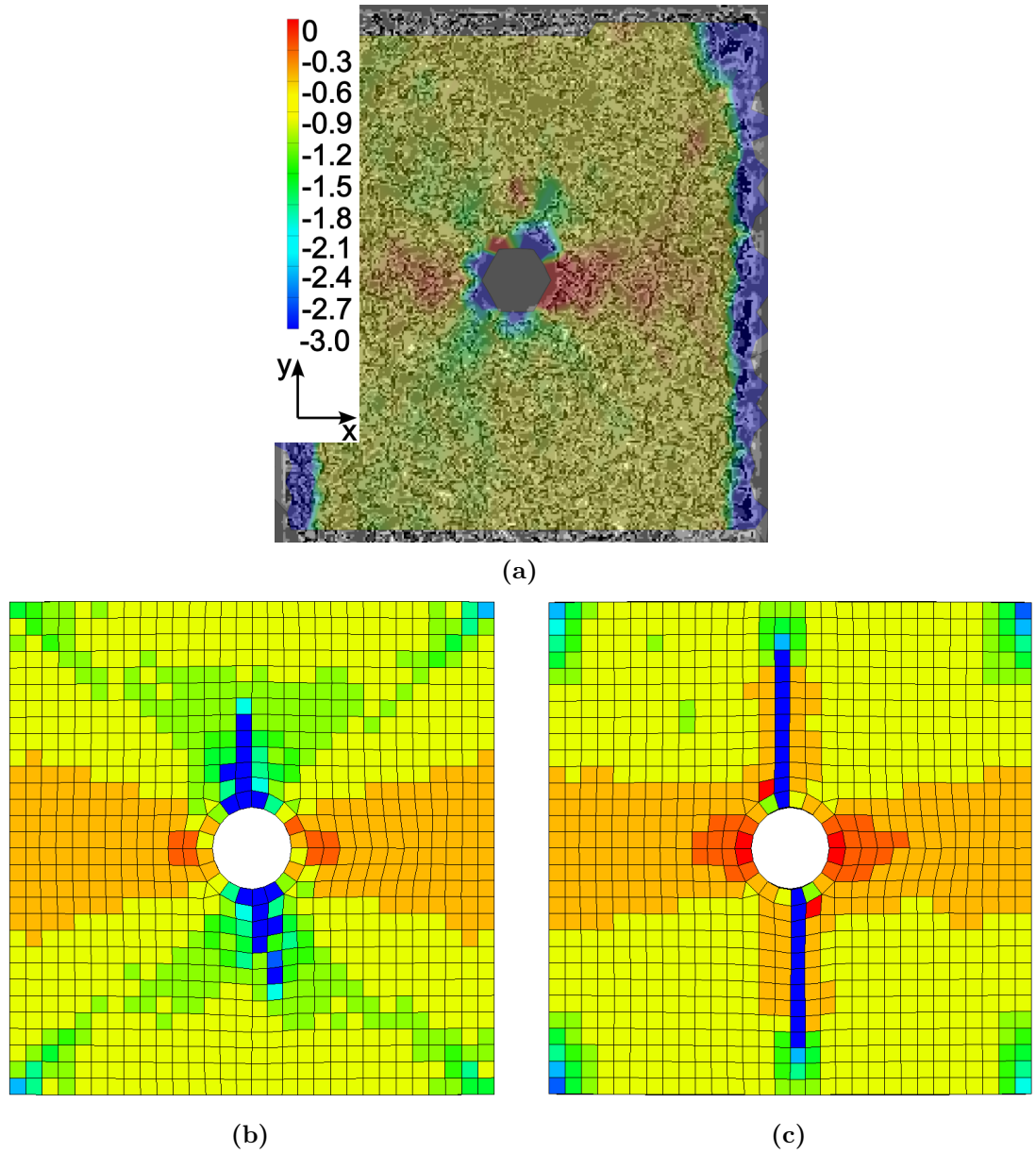

Fig. 6-5 Comparison of strain field in outer 90° layer of (a) QS specimen 10, (b) 4S_QS simulation, and (c) 16S_QS simulation at nominal strain $\epsilon_x = 1\%$ and with a uniform color scale.

each of the four samples. The observed initial stiffness exhibits a significant CV characteristic of split-Hopkinson bar experiments. However, the statistical scattering of the fracture strain and strength is comparable to the QS results (see Table 6-1). With a mean SR of 92.2 ± 8.5 1/s, all properties show an expectedly pronounced SR increase of 24% to 31%.

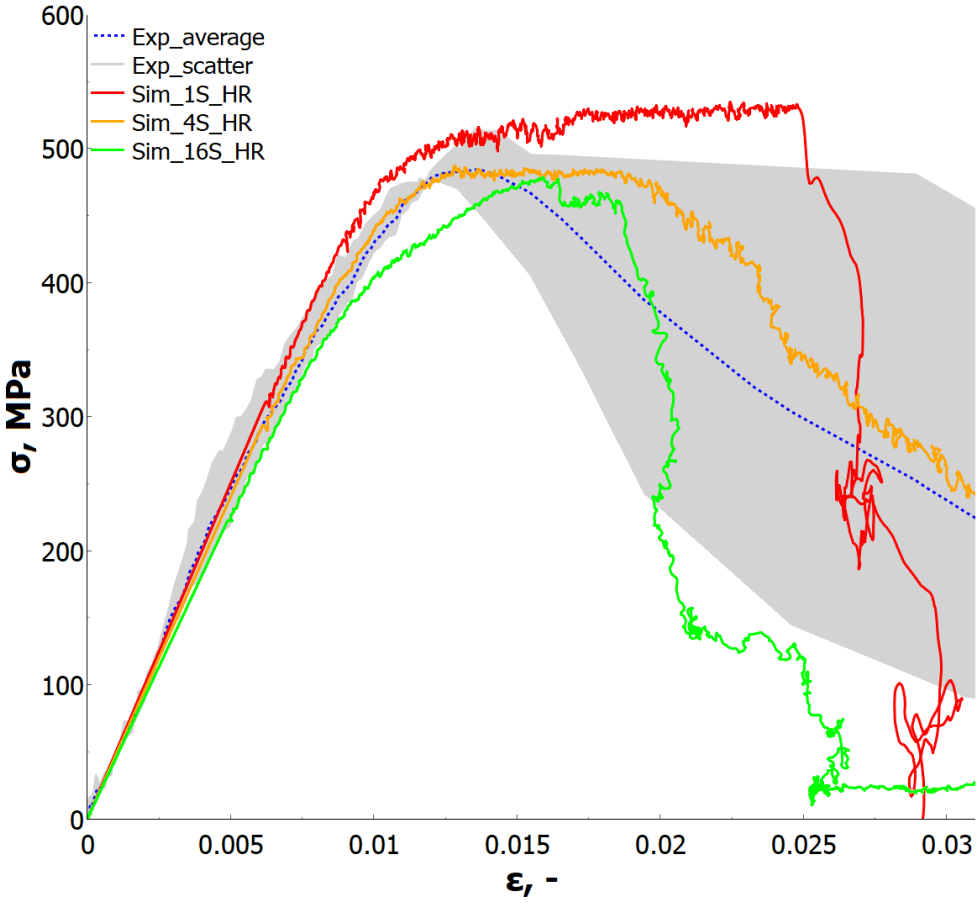

Fig. 6-6 Comparison of stress-strain average and scatter band from OHC_HR experiments with the corresponding numerical variants 1S, 4S, and 16S.

Figure 6-7, Figure 6-8, and Figure 6-9 exhibit the intra- and interlaminar failure patterns in the three outer layers as well as up to three primarily affected interfaces between two sub-laminates (4S) or single layer shells (16S). Similarly, failure initiation and the final failure pattern are displayed for the QS simulations. It should be noted that the responses of all HR models are very similar to their QS equivalents, only scaled to a higher stress and strain level.

Regarding failure mechanisms and characteristics in the 1S setup, the HR simulations are comparable to their QS counterparts. The initial stiffness fits the experimental

average, whereas maximum stress and strain at maximum stress are overrated by the single-shell approach due to the missing delamination interfaces (see Figure 6-6 and Table 6-1).

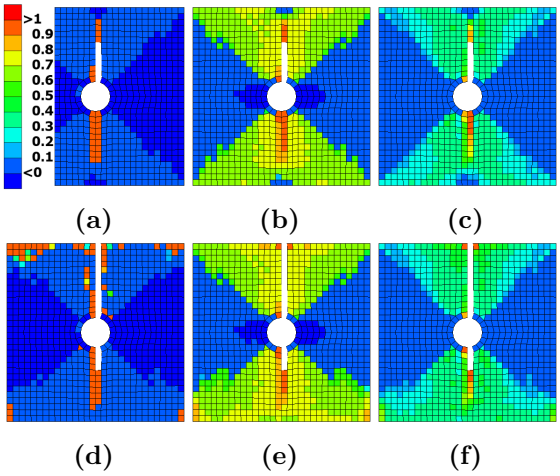

Fig. 6-7 Damage pattern of the 1S_HR model: initiation (a) 90° layer, (b) 0° layer, (c) 45° layer; final (d) 90° layer, (e) 0° layer, (f) 45° layer

Less delamination is produced by the 4S_HR model when compared to 4S_QS, but other than that, the damage pattern is almost identical (see Figure 6-8). The stress-strain response of this model agrees remarkably well with the experimental measurements regarding all key figures (see Figure 6-6 and Table 6-1). The strain fields of the experiment and 4S simulation in Figure 6-10a and Figure 6-10b are again similar. Still, the bigger extent of the highly strained central area close to the crack observed in the 4S_QS model also emerges in the HR variant.

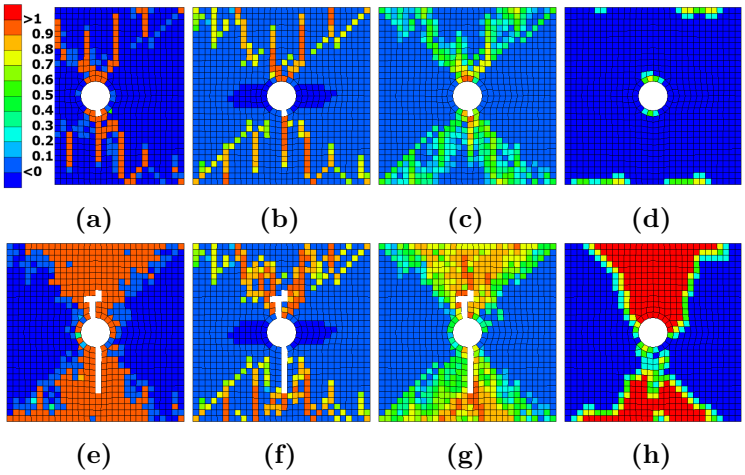

Fig. 6-8 Damage pattern of the 4S_HR model: initiation (a) 90° layer, (b) 0° layer, (c) 45° layer, (d) delamination of outer to inner shell; final (e) 90° layer, (f) 0° layer, (g) 45° layer, (h) delamination of outer to inner shell

The 16S_HR simulation exhibits similar delamination at fracture as the QS variant. Nevertheless, the damage pattern of the 0° layer is more dispersed (see Figure 6-9). On the other hand, the higher SR reduces the size of the delaminated areas. The stress-strain behavior is in good agreement with the experiments, although the premature stiffness reduction and the subsequent overestimation of the fracture strain can be observed again (see Figure 6-6 and Table 6-1). Even though the highly strained area is again more expanded in the simulation, the strain fields upon maximum force are essentially the same for both the 16S simulation and the experiment, as shown by the comparison of Figure 6-10a and Figure 6-10c.

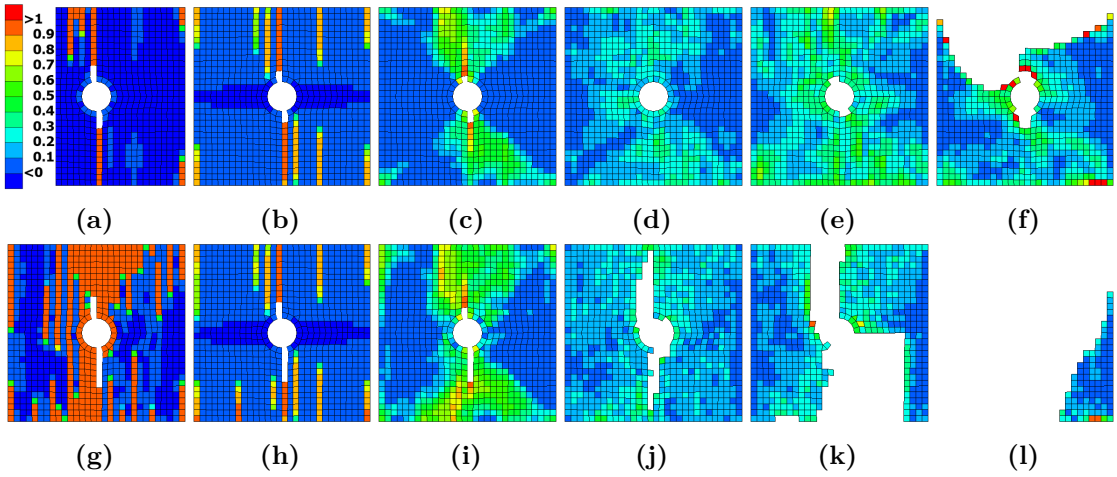

Fig. 6-9 Damage pattern of the 16S_HR model: initiation (a) 90° layer, (b) 0° layer, (c) 45° layer, (d) delamination 90°- to 0° layer, (e) delamination 0° to +45° layer, (f) delamination +45°- to -45° layer; final (g) 90° layer, (h) 0° layer, (i) 45° layer, (j) delamination 90°- to 0° layer, (k) delamination 0° to +45° layer, (l) delamination +45°- to -45° layer

6.1.3 Summary assessment

Tab. 6-1 Overview of initial stiffnesses, strengths, and fracture strains in OHC experiments and simulations (color code for deviation from experimental average values: <10% green, 10-15% yellow, 15-20% orange, >20% red).

Initial Stiffness[a]				
Sim/Exp[b]	Denomination	Value	Denomination	Value
Exp	QS Mean	40,246 MPa	HR Mean	49,875 MPa
Exp	QS STDV	2,746 MPa	HR STDV	6,891 MPa
Exp	QS CV	6.8%	HR CV	13.8%
Sim	1S_QS	49,522 MPa	1S_HR	50,030 MPa
Sim	4S_QS	47,427 MPa	4S_HR	48,029 MPa
Sim	16S_QS	43,934 MPa	16S_HR	44,215 MPa
Strength				

Sim/Exp	Denomination	Value	Denomination	Value
Exp	QS Mean	395 MPa	HR Mean	491 MPa
Exp	QS STDV	15 MPa	HR STDV	18 MPa
Exp	QS CV	3.9%	HR CV	3.5%
Sim	1S_QS	468 MPa	1S_HR	535 MPa
Sim	4S_QS	416 MPa	4S_HR	487 MPa
Sim	16S_QS	429 MPa	16S_HR	479 MPa
Fracture strain				
Sim/Exp	Denomination	Value	Denomination	Value
Exp	QS Mean	1.02E-02	HR Mean	1.34E-02
Exp	QS STDV	3.69E-04	HR STDV	8.25E-04
Exp	QS CV	3.5%	HR CV	6.2%
Sim	1S_QS	1.51E-02	1S_HR	2.24E-02
Sim	4S_QS	1.21E-02	4S_HR	1.28E-02
Sim	16S_QS	1.58E-02	16S_HR	1.59E-02

[a] Calculated in strain-interval from 0.1% to 0.5%

[b] Simulation/experiment

For the deployment of FE tools in development processes, calculation performance also plays an important role. Therefore, Table 6-2 gives a summary of the runtimes for all OHC simulations. More stacked shells produce more contact interfaces, which significantly increases simulation times by about 60% for the 4S_QS configuration compared to the 1S_QS configuration. Apart from the increasing number of contact partners, the almost 20-fold rise of the runtime for the 16S in comparison to the 1S simulation can additionally be attributed to: (a) element formulation *ELFORM* 16 is numerically more expensive, (b) the higher number of integration points per ply, and (c) the reduced timestep governed by the through-thickness element length. The additional numerical effort required to take into account SR dependencies in the HR material card also tends to increase simulation runtimes by 40% to 65%.

Tab. 6-2 Model size and runtime comparison for OHC simulations (time step: 2.7E-8 for 1S/4S and 1.5E-8 for 16S).

QS	Elements	Runtime (s)
1S	888	15
4S	3,552	25
16S	27,528	285
HR	Elements	Runtime (s)
1S	888	22
4S	3,552	35
16S	27,528	470

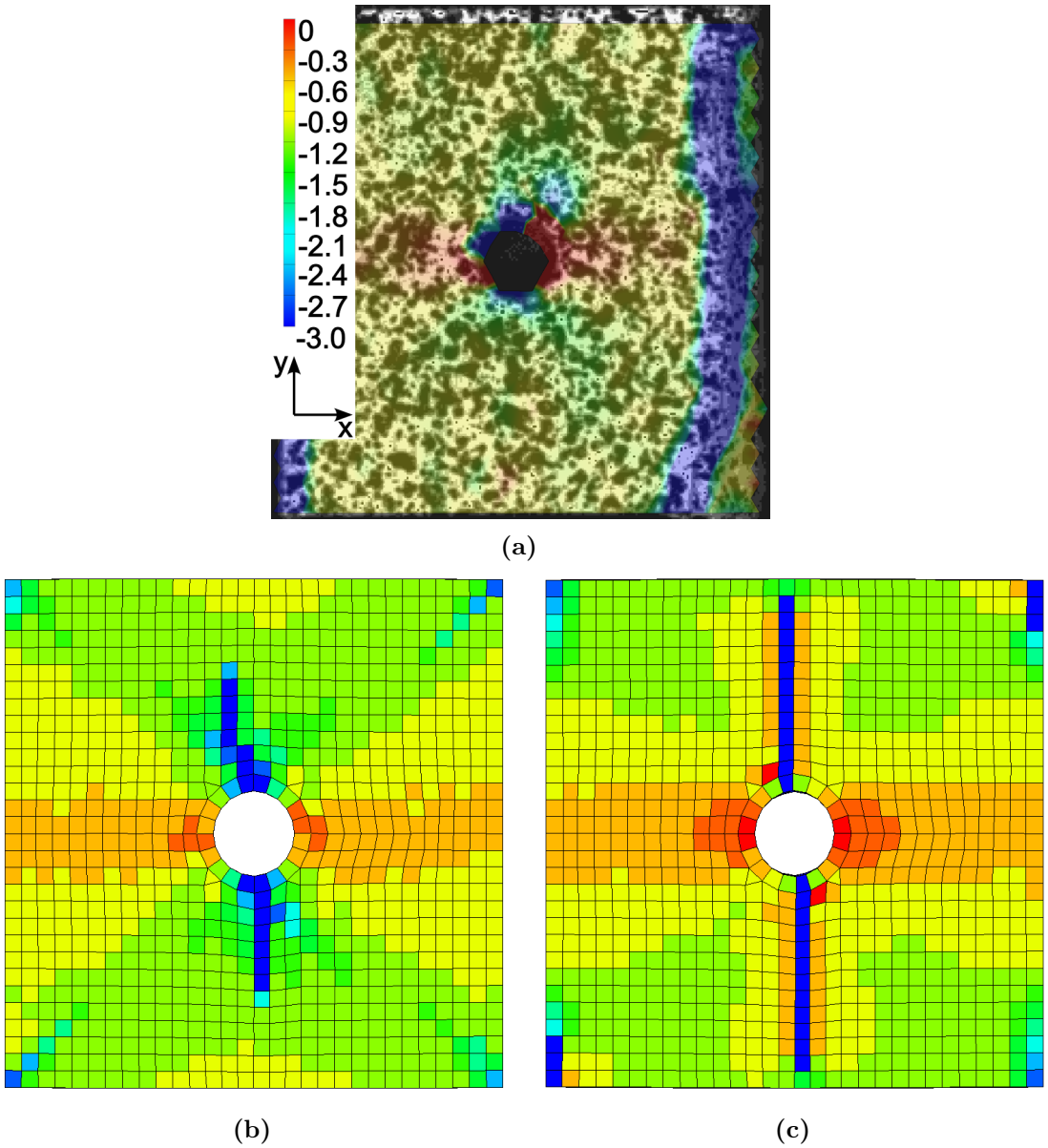

Fig. 6-10 Comparison of strain field in outer 90° layer of (a) HR specimen 3, (b) 4S_HR simulation and (c) 16S_HR simulation at nominal strain $\epsilon_x = 1.2\%$ and with a uniform color scale.

SSMs (1S), SLMs (4S), and DPMs (16S) were used to replicate the experimental OHC results. The QS stiffness, strength and fracture strain response of the OHC specimens is overestimated in all numerical models, whereas the predictions in the HR domain are closer to the experiments. The modeling studies show that SSMs systematically overestimate force levels due to the lack of delamination failure. DPMs yield accurate prognoses but suffer from premature softening caused by the applied intralaminar material formulation. Interestingly, SLMs show the most appropriate prediction. In addition, this model turned out to be about ten times more runtime-efficient when compared to the DPMs.

6.2 Experiments and simulations with triangular through-thickness trigger specimens

6.2.1 Medium-rate domain

The stress-displacement and energy-displacement diagrams of the TTT MR crushing experiments and the three simulations are depicted in Figure 6-11. The corresponding damage patterns of a typical experiment and the models within and after the trigger phase are given in Figure 6-13. Also, Table 6-3 provides an overview of the maximum initiation stress, crushing stress, and SEAs for experiments and simulations. The experiments reached an average maximum initiation stress value of 118.6 MPa, an MCS of 58.2 MPa between 5 and 6.5 mm displacement, and an SEA of 63.6 J/g up to a displacement of 6.5 mm. CVs lie below 10% except from the crushing stress. A microsection was made of an exemplary specimen (see Figure 6-12a). The microsection shows most of the failure modes and damage mechanisms described in Figure 1-2. The crush front is very localized, and the cross-section of the sample appears in a Y-shape. The black band in the top left corner is caused by a pore, which was probably created during the surface preparation for microscopy.

Compared to the experiments, the stress increase is initially underrated in all simulation models. The deviation might be attributed to debris formation. In the experiments, the fragments stay in the fracture zone because the specimen still has intact fiber bundles attached or because the fragments lack sufficient kinetic energy to get dispersed. However, elements reaching the critical effective strain in the scaled-velocity simulations are deleted. This behavior can be clearly seen when comparing the inner laminate layers, bent laterally in Figure 6-13h at original velocity and deleted in Figure 6-13i at scaled velocity. As a result, there are conflicting requirements to keep elements available for the solution or receive negative Jacobians

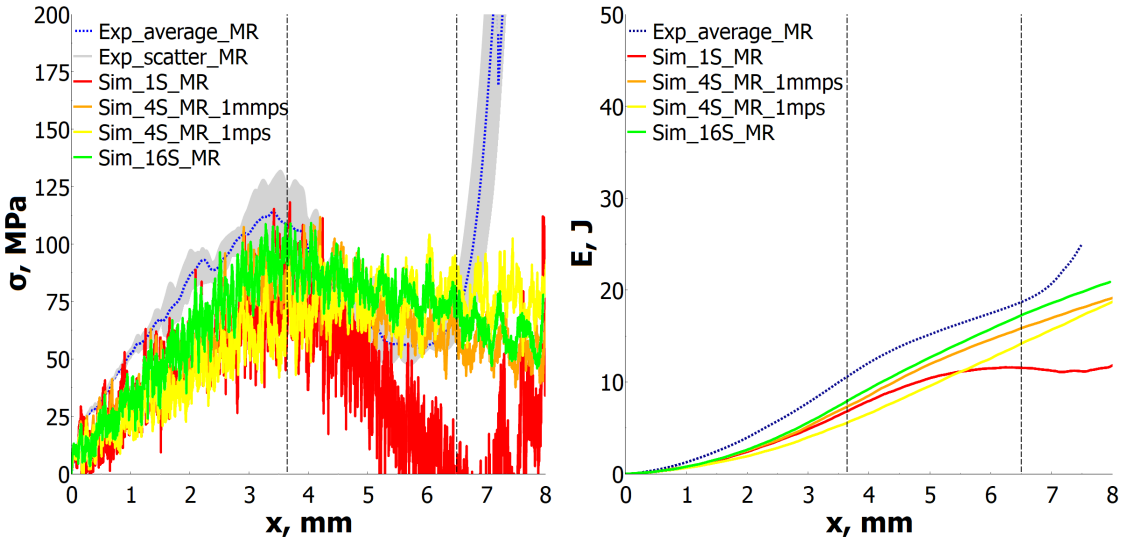

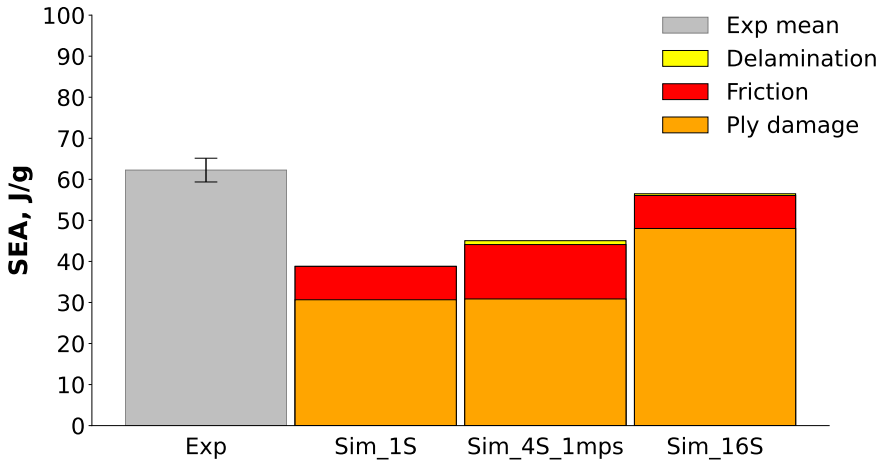

Fig. 6-11 (a) Comparison of stress-displacement average and scatter band from MR experiments with the corresponding numerical variants 1S, 4S_1mmps, 4S_1mps, and 16S. Comparison of (b) the corresponding energy-displacement curves and (c) the mean energy absorption and standard deviation from MR experiments and energy breakdowns for the evaluable numerical variants at 6.5 mm displacement. The vertical lines on the curve plots indicate the end of the trigger (3.6 mm) and the stable crushing length (6.5 mm).

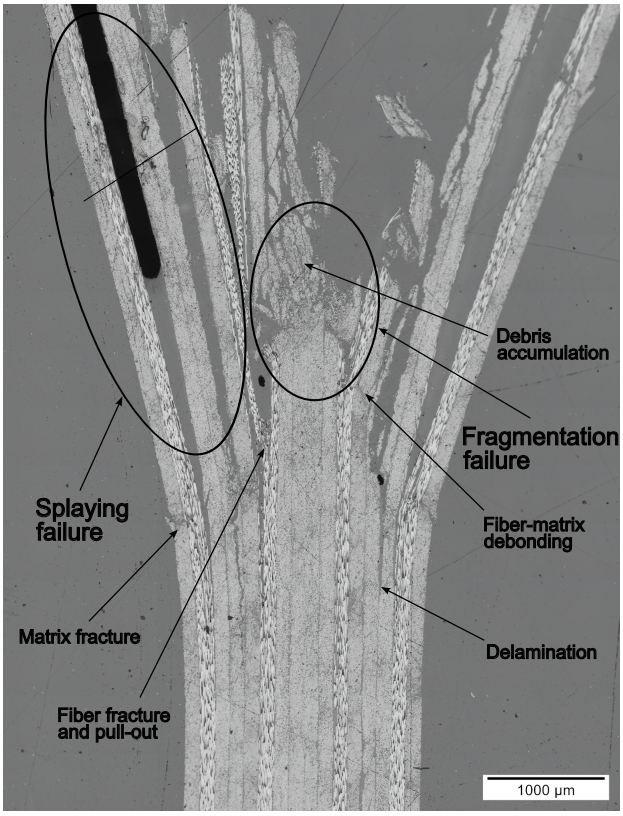

(a)

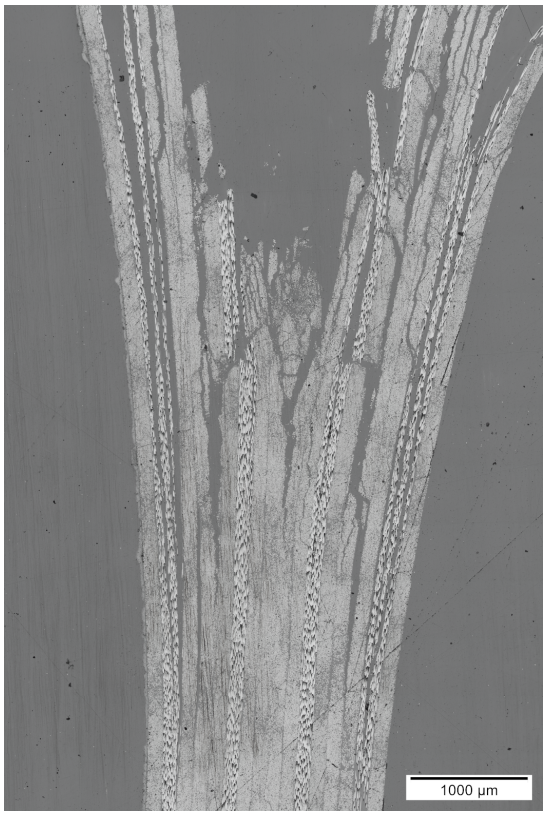

(b)

Fig. 6-12 Through-thickness microsection of TTT specimens (layup $(90/0/\pm 45)_{2s}$): (a) MR specimen 6 exhibiting the typical crushing failure modes and micro-scale damage patterns, (b) specimen tested at reduced HR impact velocity of 1.5 m/s [121].

in highly distorted elements, which may provoke error terminations. Other authors also highlighted this issue [93, 97].

The 1S model reaches maximal stresses in the range of the experimental scatter band; still, it should be noted that the level of the maximum values is sustained by the noise of the unfiltered curves. After an accurate initial prediction of the stress-strain response by the 1S model, stress drops to zero at approximately 6 mm displacement. The reduction is due to the brittle fracture of the specimen as the impactor approaches the fixture. Neither crushing stress nor SEA are, therefore, predicted correctly.

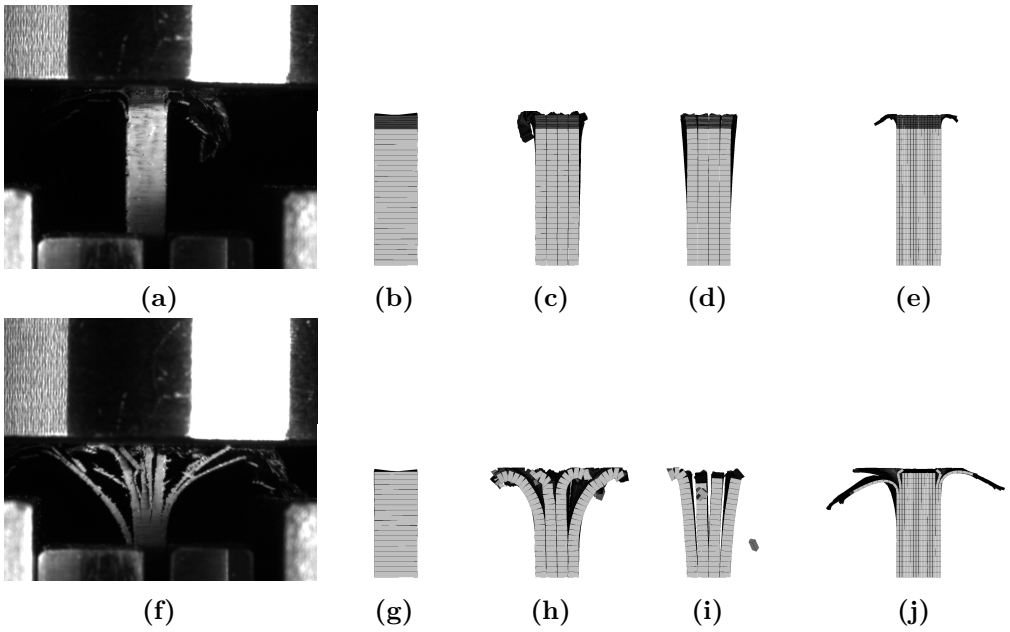

Fig. 6-13 MR failure patterns at 3 mm displacement of (a) specimen 6, (b) 1S, (c) 4S at original velocity (1mmps), (d) 4S at scaled velocity (1mps), and (e) 16S model. Failure patterns at 5 mm displacement of (f) specimen 6, (g) 1S, (h) 4S at original velocity, (i) 4S at scaled velocity, and (j) 16S model. Cohesives, impactor, and limit stop are removed in the models; shell thickness is shown.

The 4S variants exhibit different failure patterns and load levels from trigger initiation onward. As can be seen in Figure 6-13c and Figure 6-13h, the original-velocity variant (1mmps) is able to generate pronounced delaminations and fronds from the damaged material in the outer shells. This behavior is comparable to the experiments and yields stress peaks in the range of the experimental maximum. It also supports the above statement regarding the difference in the initiation stress between experiments and simulations since the load level of 4S_1mmps is higher than in 4S_1mps. Furthermore, variant 4S_1mmps can reproduce the load drop and the crushing stress level (65.0 MPa) along with the SEA (53.9 J/g), which are close to the experimental mean values.

The 16S_MR simulation exhibits a damage pattern similar to the experiments during the initiation phase with outward bending of outer plies (see Figure 6-13e). Still, the extent of delamination is underrated after the trigger phase has come to an end, as depicted in Figure 6-13j). The experimental stress maximum is almost reached (109.2 J/g). Moreover, the SEA is predicted well (58.7 J/g), whereas crushing stress is overestimated (76.5 MPa). The stress increase observed in the 4S simulation at original velocity – compared to scaled velocity – indicates that a 16S original-velocity variant could further improve the prediction. Unfortunately, such a simulation lies beyond the scope of this thesis since the corresponding 16S models would lead to HPC runtimes of more than 1,000 hours on 18 cores.

Figure 6-11c provides an additional overview of the SEAs in the experiments and simulations with a breakdown of the absorption mechanisms for the latter. As can be seen, the main part of the energy is absorbed as in-plane damage, followed by friction and delamination. In the 4S model, friction (29.4%) and delamination (2.1%) play a bigger role than in the other two models; friction accounts for 21.0% in 1S and 14.2% in 16S, delamination for a mere 0.7% in 16S. The ratio of the contributions per mechanism is well-aligned with data from literature studies on component level at higher loading rates [53, 55, 70, 107]. The simulation at initial velocity (1mmps) does not offer a correct distribution of the energies for each mechanism because their average exceeds the total energy. This behavior occurred, although the simulation was conducted with a model equivalent to the scaled-velocity run. Given the excessive runtime of the simulation, a more thorough analysis of this issue was outside the scope of this thesis. Thus, no energy breakdown is shown for this simulation.

6.2.2 High-rate domain

The stress-displacement and energy-displacement diagrams of the TTT HR crushing experiments and the three simulations are presented in Figure 6-14. The corresponding damage patterns of a typical experiment and the models within and after the trigger phase are given in Figure 6-15. In addition, Table 6-3 provides an overview of the maximum initiation stress, crushing stress, and SEAs for experiments and simulations. The experiments reached an average maximum initiation stress value of 97.1 MPa, an MCS of 55.3 MPa between 5 and 6.5 mm displacement, and an SEA of 51.5 J/g up to a displacement of 6.5 mm. CVs are in the range of 10% for all key figures. Initiation stress is reduced by approximately 20% compared to the MR value, whereas the crushing stress remains virtually unchanged. Since the crushed area of the HR specimens was completely disintegrated during the final deceleration of the impactor, no microsection could be created for this experimental

series. However, the microsection in Figure 6-12b from a sample tested at a reduced HR impact velocity of 1.5 m/s and already presented in the study of Pohl et al. can be used. The damage pattern mainly agrees with the MR pattern regarding the splaying failure in the outer specimen layers and the fragmentation failure in the specimen's core. Contrarily, the delaminations reach much deeper into the sample, leading to a V- instead of a Y-shaped cross-section.

The 1S and 4S variant initially coincide with the experimental stress increase, but exceed the maximum initiation and crushing stress along with the SEA. Neither of the variants can reproduce the failure mechanism correctly. The layers in the 4S model do not detach from each other even though interlaminar gaps emerge during crushing, as shown in Figure 6-15g. Thus, there is only a minor difference between the two variants. In the absence of delamination, SR-induced intralaminar property increases elevate the crushing stress level of both the 1S and 4S model compared to the MR domain. It should also be noted that the maximum displacements differ between the variants due to the "bullnose effect", which creates a positive fillet at the edges of shell elements (see Figure 6-16a). This virtual fillet with a radius of half the shell height triggers premature contact of the specimen edge with the impactor leading to a maximum displacement of more than 8 mm. The effect is most pronounced for the 1S models because they use the biggest shell thickness.

16S exhibits considerable delamination from the trigger phase on (see Figure 6-15d and Figure 6-15h). The initially one-sided detaching is observed in the experiment and simulation likewise. Delamination reduces the maximum initiation stress to 118.5 MPa when compared to the 4S model. This level is close to the experiments, as is the SEA (54.7 J/g). The load drop after the end of the trigger phase can be attributed to a systematic underestimation of the residual stiffness in *MAT_058 (see Equation 5-3). The incorrect prediction of the unloading behavior in the crushing process is a known deficiency of *MAT_058 and was first described by Xiao et al. [46]. The mainly load-bearing 0° layers partly buckle during crushing, which virtually interrupts load transmission in these layers (see Figure 6-16b). The premature buckling of the 16S TTT models aligns with the premature softening of the 16S OHC models, which was also traced back to the early failure of the 0° plies.

The 16S_HR models are suitable for evaluating the SR levels in the plies and the delamination planes. Figure 6-16c and Figure 6-16d show the fringe plots of occurring effective intralaminar and interlaminar SR, respectively. The plots exhibit local SRs of more than 5,000 1/s in the stable crushing phase, which is multiple times higher than the nominal SR (456 1/s). Intralaminar rates appear elevated in comparison to the rates in the delamination planes. The very localized strain field obscured by debris formation below the impactor did not allow a meaningful comparison of the numerical results to high-speed camera footage from the experiments.

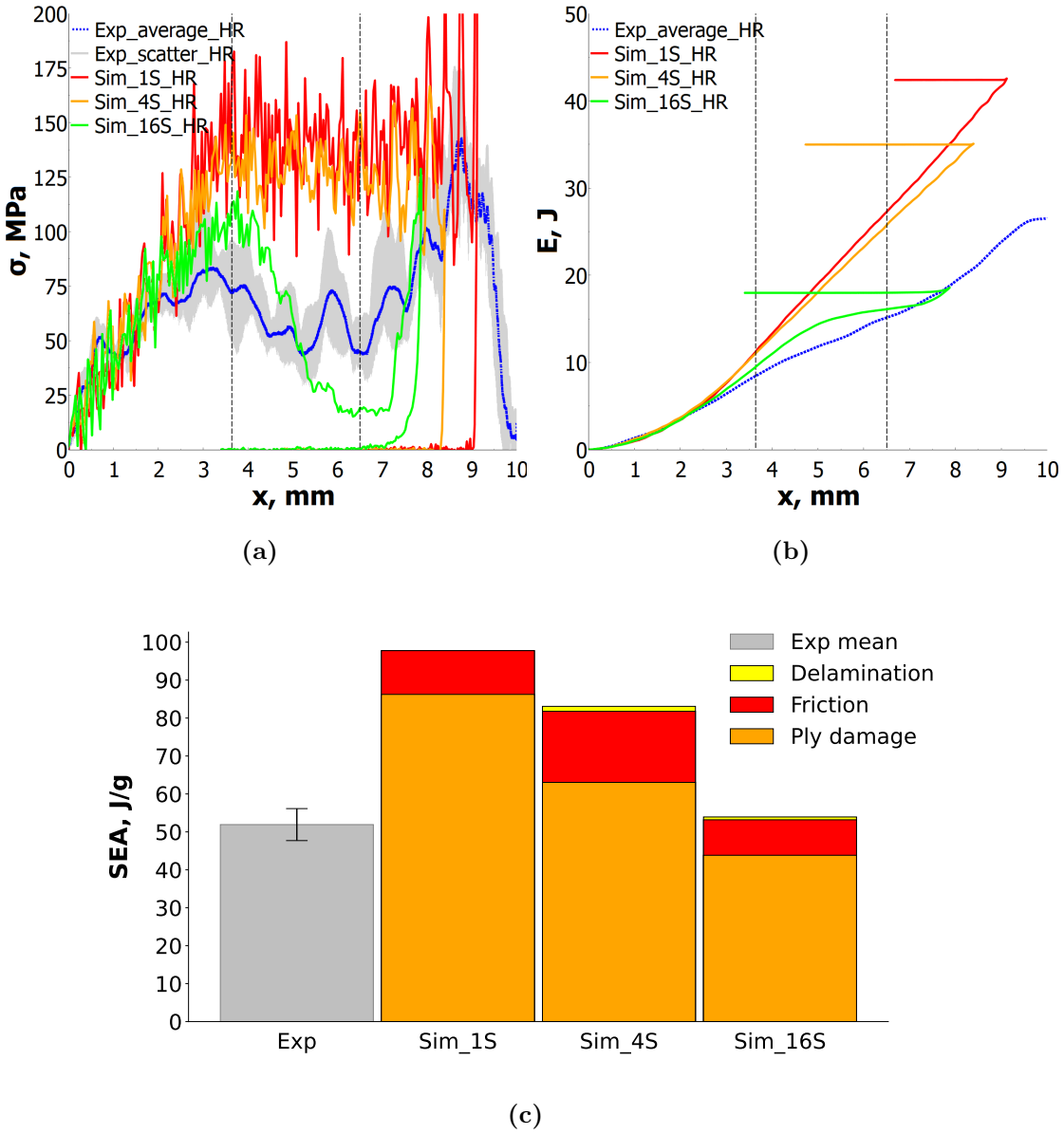

Fig. 6-14 (a) Comparison of stress-displacement average and scatter band from HR experiments with the corresponding numerical variants 1S, 4S, and 16S. Comparison of (b) the corresponding energy-displacement curves and (c) mean energy absorption and standard deviation from HR experiments and energy breakdowns for the numerical variants at 6.5 mm displacement. The vertical lines on the curve plots indicate the end of the trigger (3.6 mm) and the stable crushing length (6.5 mm).

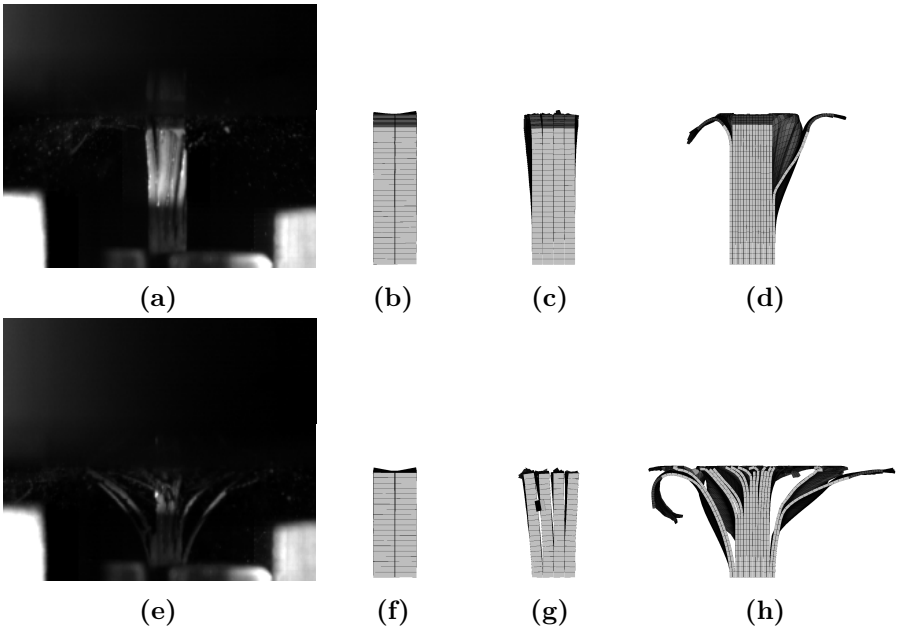

Fig. 6-15 HR failure patterns at 3 mm displacement of (a) specimen 7, (b) 1S, (c) 4S, and (d) 16S model. Failure patterns at 5 mm displacement of (e) specimen 7, (f) 1S, (g) 4S, and (h) 16S model. Cohesives, impactor, and limit stop are removed in the models; shell thickness is shown.

Figure 6-14c gives a breakdown of the absorption mechanisms for the simulations and an average value of the SEA in the experiments. As can be seen, delamination and friction only absorb a fraction of the energy, whereas intralaminar damage accounts for most energy dissipation. Again, in the 4S model, friction (22.6%) and delamination (1.6%) play a more prominent role than in the other two models, which absorb 11.8% (1S) and 17.3% (16S) by friction and 1.4% (16S) of the energy by ply debonding. The ratio of the contributions per mechanism agrees with literature values [53, 70, 107]. The rising loading rate is associated with a slight increase in the friction and delamination contributions for the 16S models. This phenomenon was also found by Chen et al., but it was more pronounced in their thick-walled composite tubes [55].

6.2.3 Additional numerical studies and summary assessment

Table 6-3 summarizes the results of the MR and HR TTT crushing experiments and simulations.

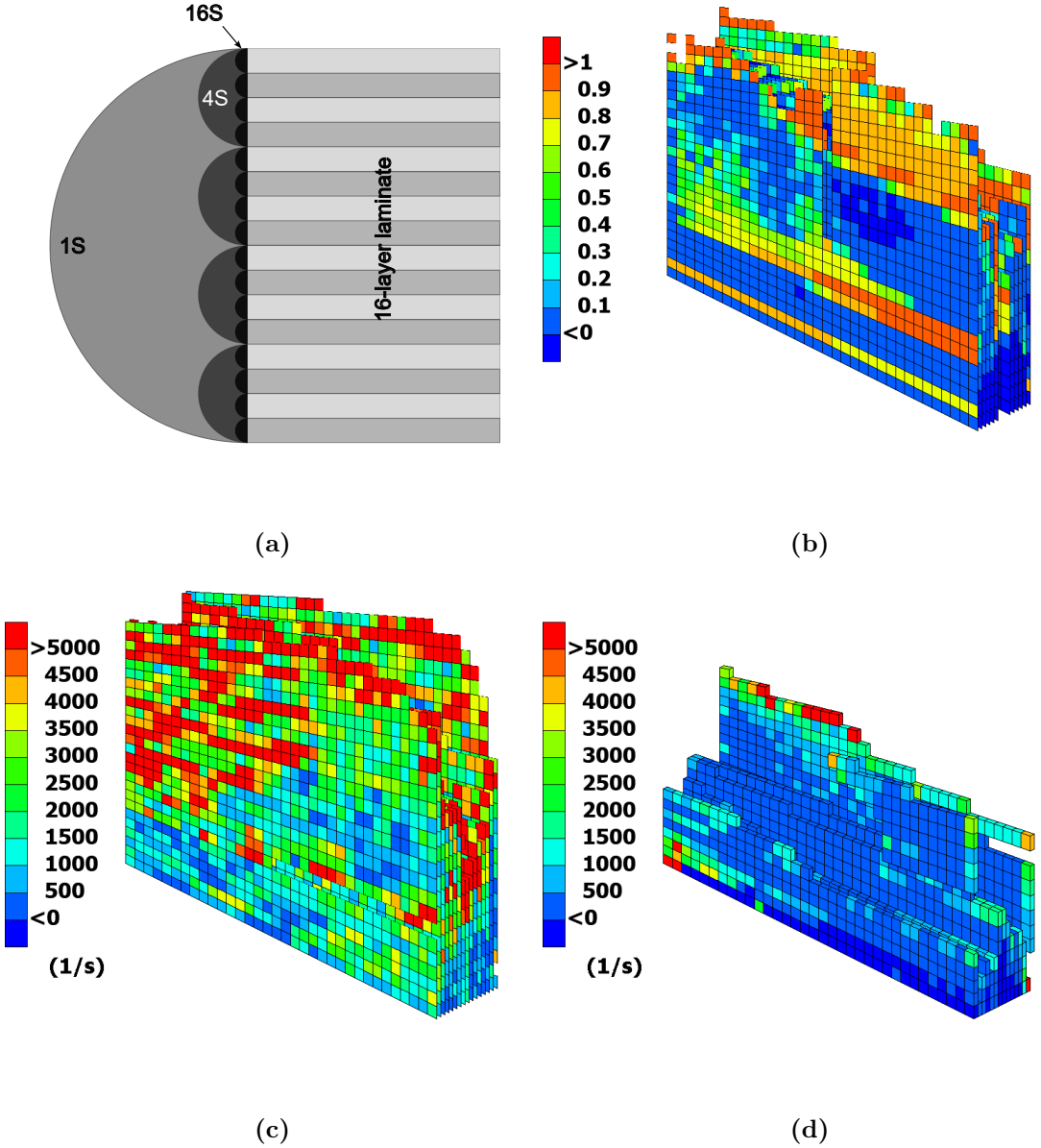

Fig. 6-16 (a) Representation of the "bullnose effect" in a schematic through-thickness section. (b) Isometric view onto 0° layers with damage variable in 0° direction at 6.5 mm displacement in 16S_HR model. The field outputs are shown on the undeformed mesh of the specimen without thickness representation for shell elements. Isometric view onto (c) intralaminar and (d) interlaminar SR field output at 1.5 mm displacement in 16S_HR model.

Tab. 6-3 Overview of maximum initiation stress, crushing stress, and SEA in TTT experiments and simulations (color code for deviation from experimental average values: <10% green, 10-15% yellow, 15-20% orange, >20% red).

Maximum initiation stress				
Sim/Exp[a]	Denomination	Value	Denomination	Value
Exp	MR Mean	118.6 MPa	HR Mean	97.1 MPa
Exp	MR STDV	11.6 MPa	HR STDV	12.5 MPa
Exp	MR CV	9.8%	HR CV	12.9%
Sim	1S_MR	118.3 MPa	1S_HR	187.0 MPa
Sim	4S_MR_1mmps	111.8 MPa	4S_HR	153.4 MPa
Sim	4S_MR_1mps	99.2 MPa	-	-
Sim	16S_MR	109.2 MPa	16S_HR	118.5 MPa
MCS[b]				
Sim/Exp	Denomination	Value	Denomination	Value
Exp	MR Mean	58.2 MPa	HR Mean	55.3 MPa
Exp	MR STDV	5.9 MPa	HR STDV	6.2 MPa
Exp	MR CV	10.1%	HR CV	11.3%
Sim	1S_MR	18.7 MPa	1S_HR	136.1 MPa
Sim	4S_MR_1mmps	65.0 MPa	4S_HR	124.3 MPa
Sim	4S_MR_1mps	76.8 MPa	-	-
Sim	16S_MR	76.5 MPa	16S_HR	27.8 MPa
SEA[c]				
Sim/Exp	Denomination	Value	Denomination	Value
Exp	MR Mean	63.6 J/g	HR Mean	51.5 J/g
Exp	MR STDV	3.5 J/g	HR STDV	3.8 J/g
Exp	MR CV	5.5%	HR CV	7.5%
Sim	1S_MR	39.2 J/g	1S_HR	92.7 J/g
Sim	4S_MR_1mmps	53.9 J/g	4S_HR	87.0 J/g
Sim	4S_MR_1mps	48.2 J/g	-	-
Sim	16S_MR	58.7 J/g	16S_HR	54.7 J/g

[a] Simulation/experiment

[b] Average value between 5 and 6.5 mm or maximum displacement

[c] Integrated value until 6.5 mm or maximum displacement

The runtimes for all TTT simulations are given in Table 6-4. The trend of the runtime increases from 1S to 16S is similar to the OHC simulations. The duration of the MR simulations is about 50% higher than for the HR simulations since the lower impact velocity prolongs the numerical runtime and thus counteracts the higher costs of the SR formulation. As already mentioned above, simulating the 4S_1mmps variant took about 1,500-fold as long as the 4S_1mps variant.

Tab. 6-4 Model size and runtime comparison for TTT crushing simulations (time step: 2.7E-8 for 1S/4S and 1.6E-8 for 16S).

MR	Elements	Runtime (s)
1S	1,834	289
4S_1mmps	4,486	638,600[a]
4S_1mps	4,486	449
16S	29,098	8,186
HR	**Elements**	**Runtime (s)**
1S	1,835	167
4S	4,487	220
16S	29,099	5,717

[a] Runtime normalized from 8 to 18 cores

The given models – above all 16S – facilitate further numerical evaluations. In the following, additional studies will be carried out on (a) the effect of the fixture and impactor simplification in the models, (b) the influence of the friction coefficient onto the crushing process, (c) the isolated contribution of the inter- and intralaminar SR dependencies and (d) the influence of intralaminar SR dependencies of elastic and damage properties on the material response.

The 4S model was used early to evaluate the chosen approach's validity to reduce the impactor geometry to a rigid plate and the fixture to a rigid body. Figure 6-17 shows that the results of the two models are virtually identical. The consistent model simplification is therefore justifiable.

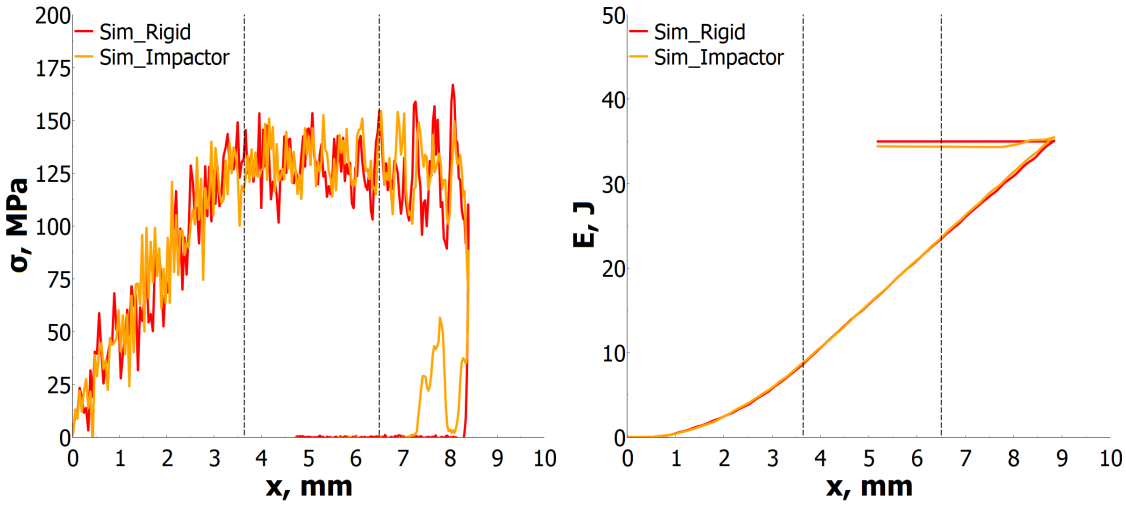

Fig. 6-17 (a) Comparison of stress-displacement response of 4S_HR with a reduced model (Rigid) and fully modeled fixture and impactor (Impactor). (b) Comparison of energy-displacement curves from the corresponding studies.

The diagrams in Figure 6-18 show that there is no clear trend in the influence of the friction coefficient onto the (crushing) stress level within the physically reasonable range reaching from 0.2 to 0.4: both variants yield comparable stress levels during the trigger phase and show only slight buckling in the 0° layers before the impactor reaches the limit stop. Therefore, the load drop reduces for both parameter variations compared to the 0.3 variant.

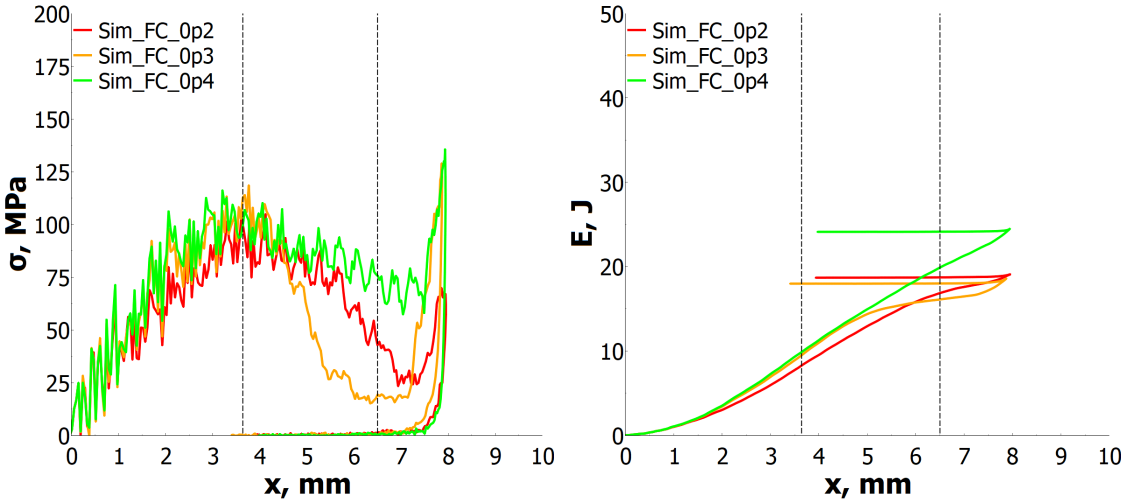

(a) (b)

Fig. 6-18 (a) Comparison of stress-displacement response of 16S_HR models with friction coefficient varied from 0.2 (FC_0p2) to 0.4 (FC_0p4). (b) Comparison of energy-displacement curves from the corresponding studies.

Figure 6-19 exhibits stress and energy against displacement for the study with selective activation of intra- (IL) and interlaminar (DEL) SR dependencies. During the trigger phase, the responses of the variants do not vary substantially, although the variants with in-plane SR dependency reach a slightly higher stress level (IL_on). After the trigger is used up in these models, a load drop occurs due to delamination comparable to the original 16_HR variant (see Figure 6-21a, Figure 6-21b, Figure 6-21e, and Figure 6-21f). The variants without in-plane SR dependency hardly show any delamination, as depicted in Figure 6-21c and Figure 6-21g. They yield an almost constantly high stress level after the end of the trigger is reached. Surprisingly, the intralaminar SR dependency promotes delamination, which in turn counteracts the positive effect of the in-plane property increases onto the stress level observed in the trigger phase.

To determine if the observed effect is caused by the SR sensitivity of elastic or damage ply characteristics, another study was carried out. As depicted in Figure 6-20a and Figure 6-20b, the SR-induced increase of the damage property values is responsible for the excessive delamination. While providing a higher initial load level,

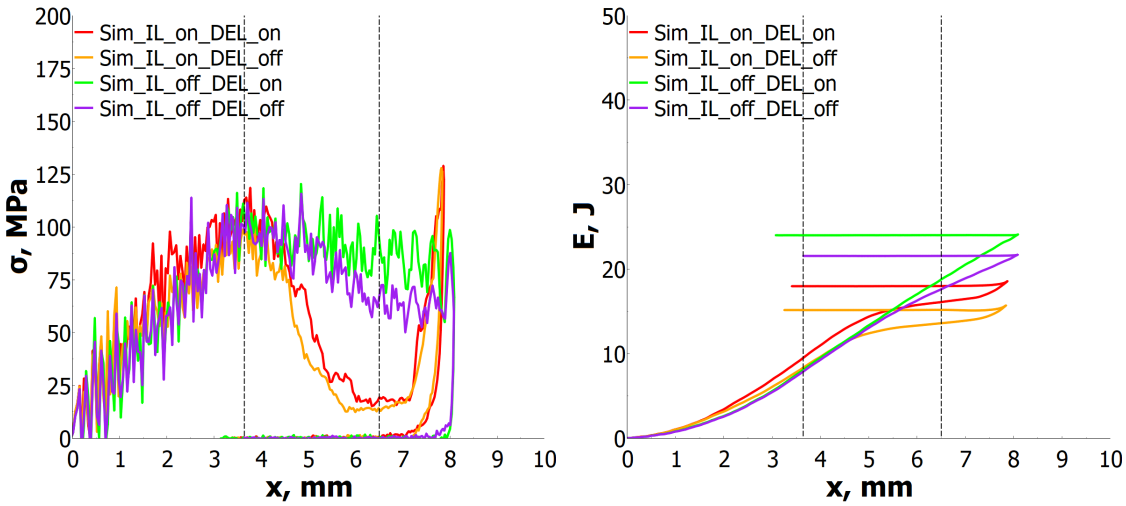

(a) (b)

Fig. 6-19 (a) Comparison of stress-displacement response of 16S_HR models with intralaminar (IL) and interlaminar (DEL) SR dependencies switched on or off. (b) Comparison of energy-displacement curves from the corresponding studies.

the exclusive activation of rate-sensitive damage properties lowers the maximum initiation and crushing stress. Out-of-plane buckling replaces in-plane crushing as the energetically favored failure mechanism as a result of increased intralaminar stresses and failure strains. Plies delaminate and buckle across the whole specimen following the trigger phase without even leaving a central ply column (see Figure 6-21d and Figure 6-21h). The damage formulation chosen for *MAT_058 could not be further broken down to separate the effects of strengths and FTs [107]. Also, it should be noted that the reported results refer to a short phase of stable crushing and that they could be valid for the present material and geometry only.

SSMs (1S), SLMs (4S), and DPMs (16S) were used to replicate the TTT crushing experiments. Probably due to the debris representation, all MR simulations systematically underestimate the initiation stress and SEA. Only 16S and a very runtime-costly 4S simulation at the original velocity are capable of achieving a stress-strain characteristic similar to the experiments. The failure pattern and the crushing stress are predicted correctly by these two variants. Additional studies on the element erosion strategy are recommended to investigate the deviation between scaled- and original-velocity models.

The correct representation of the delamination interfaces was even more critical in the HR simulations: 1S and 4S seriously overestimate the stress level, and even 16S exhibits a higher level than the experiments. Still, it becomes clear that the characteristics of the experiments can only be reproduced when delamination interfaces

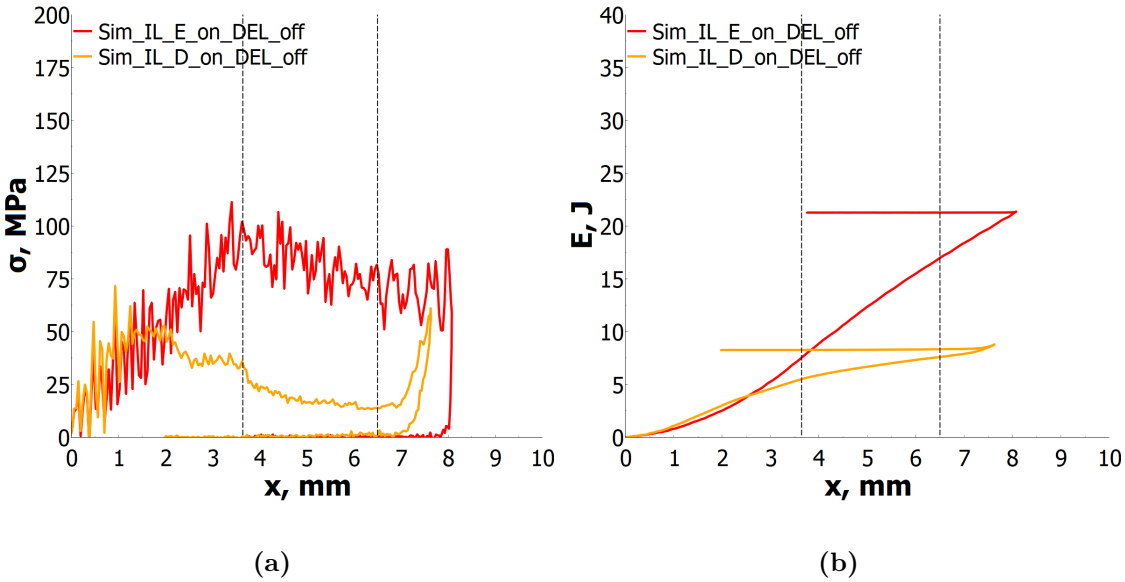

Fig. 6-20 (a) Comparison of stress-displacement response of 16S_HR models with intralaminar elastic (IL_E) and intralaminar damage properties (IL_D) SR dependencies switched on or off. (b) Comparison of energy-displacement curves from the corresponding studies.

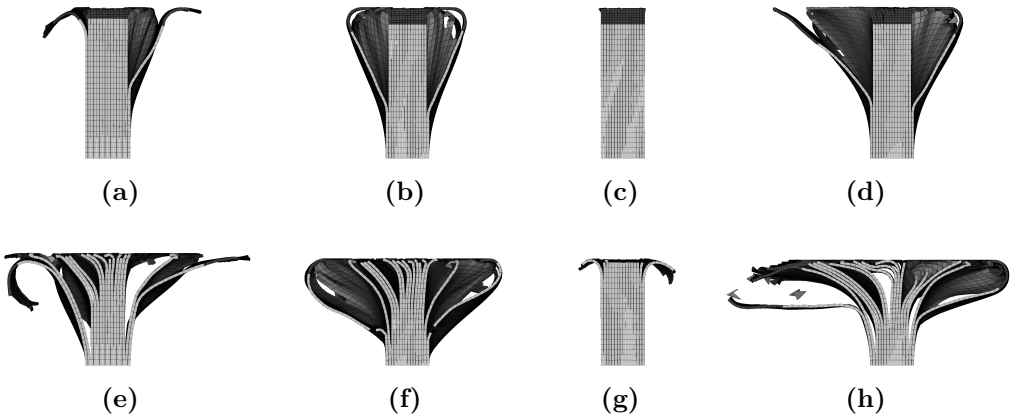

Fig. 6-21 Failure patterns of 16S_HR studies at 3 mm displacement with models including (a) all SR dependencies (IL_on_DEL_on), (b) intralaminar SR dependency (IL_on_DEL_off), (c) interlaminar SR dependency (IL_off_DEL_on), and (d) intralaminar damage property SR dependency (IL_D_on_DEL_off). (e)-(h) show the corresponding models at 5 mm displacement.

between every ply are taken into account. The missing plasticity formulation in *MAT_058 is seen as the main shortcoming to yield even better predictions of the damage behavior.

Numerical studies confirm the validity of the simplified TTT model. The global friction coefficient does not show an apparent influence on the stress-displacement behavior in the investigated range. On the other hand, two studies on the SR dependencies revealed that intralaminar rate sensitivities of damage properties increase the extent of delamination and reduce maximum loads. Further investigations are also advisable in this area.

6.3 Tube crushing experiments and simulations

6.3.1 Quasi-static domain

Figure 6-22a and Figure 6-22b present the stress and absorbed energy against displacement of the QS tube crushing experiments and simulations. Also, Figure 6-23 provides damage patterns of a typical experiment and the simulations. The overview of the maximum initiation forces, SSCSs, and MCSDs is given in Table 6-5. The available experimental curve reached an average maximum initiation force value of 73.7 kN, an SSCS of 77.4 J/g, and an MCSD of 5.0 kN.

None of the simulations can replicate the force level in the experiments. The huge difference can be associated with the failure patterns in the simulations. As shown in Figure 6-23d, large fronds formed during the experiment. Deviating from the tube length of 100 mm in the QS experiments, simulations were carried out with a uniform tube length of 200 mm for both QS and HR. As can be seen in Figure 6-23a, Figure 6-23b, Figure 6-23e, and Figure 6-23f, the scaled-up impact velocity in the 1S and 2S simulations promote premature deletion of highly distorted elements. Thus, fronds do not form during crushing, and too little load is introduced into the tubes. For the 16S_QS model, damaged shell elements remain available to the solution and build fronds. Still, the simulation does not reach the experimental load level because the interlaminar tensile strength, which was reduced to stabilize the crushing front, benefits delamination that, in turn, leads to buckling failure of the tube (see Figure 6-23c and Figure 6-23g). Subsequently, the performance figures in Table 6-5 indicate a poor predictive quality for all numerical QS models.

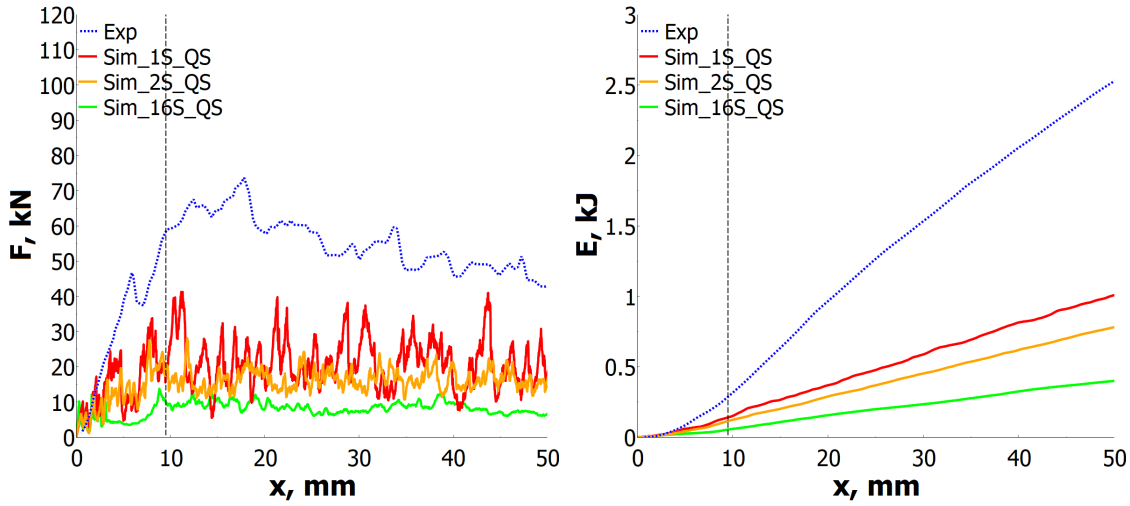

(a) (b)

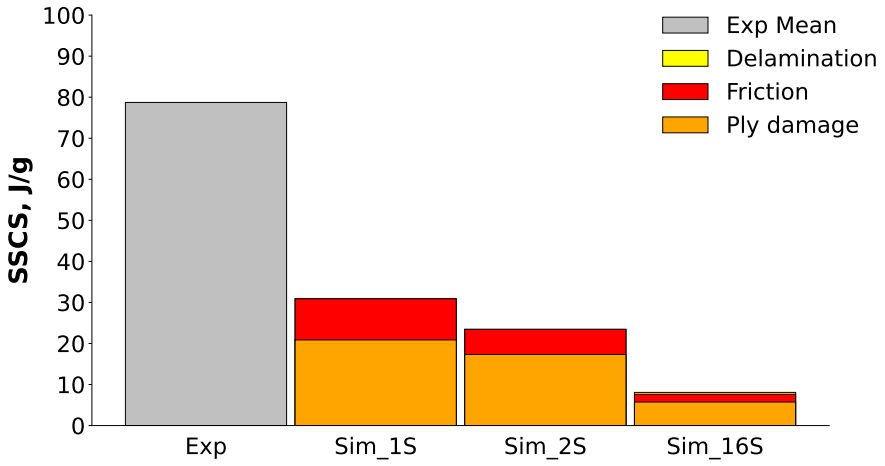

(c)

Fig. 6-22 (a) Comparison of stress-displacement average and scatter band from QS experiments with the corresponding numerical variants 1S, 2S, and 16S. Comparison of (b) the corresponding energy-displacement curves and (c) mean energy absorption and standard deviation from QS experiments and energy breakdowns for the evaluable numerical variants at 50 mm displacement. The vertical line in the curve plots indicates the end of the trigger length (9.5 mm).

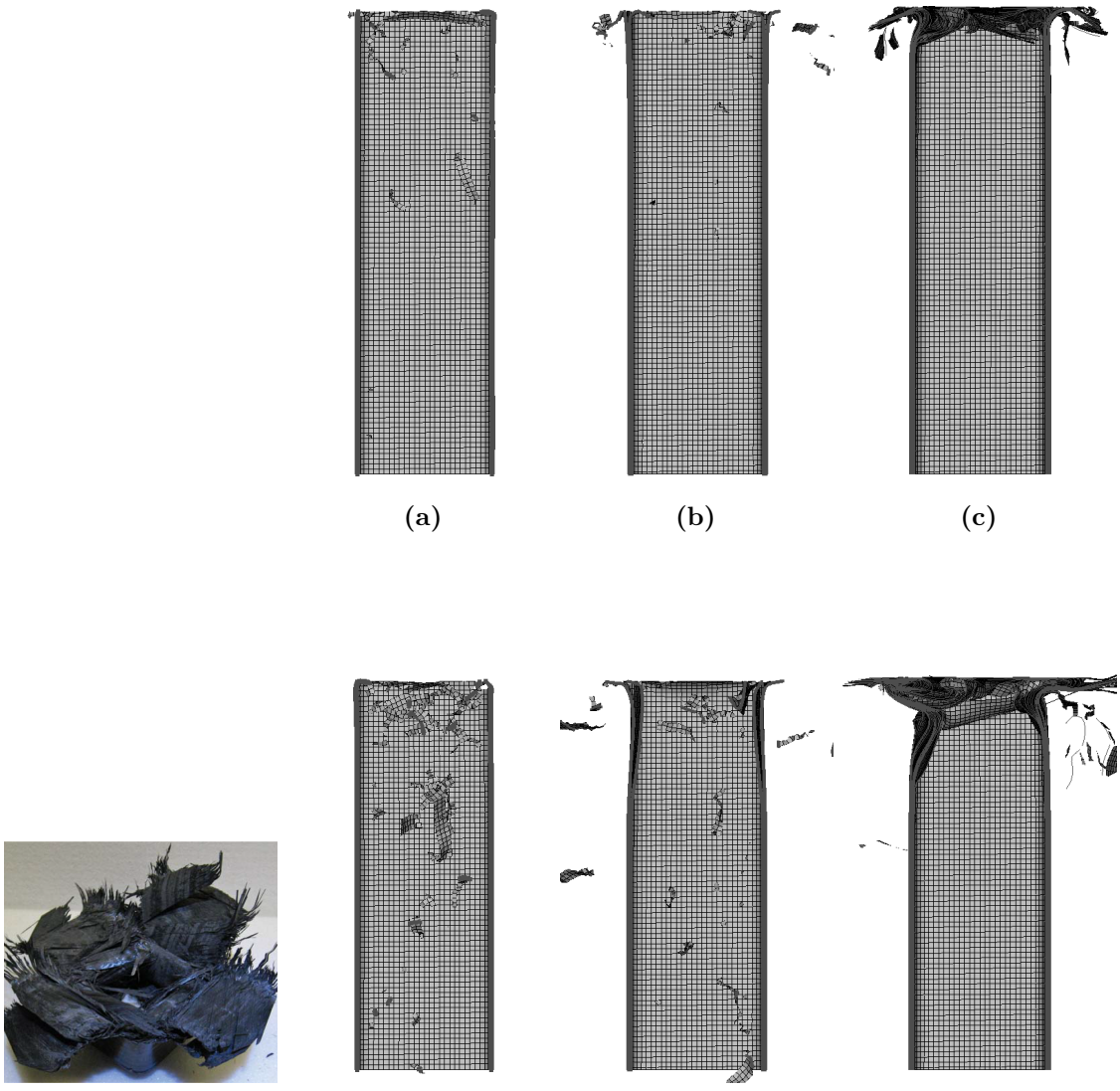

Fig. 6-23 Failure patterns of QS crushing experiment and simulations: (a) 1S, (b) 2S, and (c) 16S model cuts along the tube's longitudinal axis at 20 mm displacement. Subfigure (d) shows experiment 57B at 100 mm displacement, subfigures (e) to (g) show the 1S, 2S, and 16S model cuts at 50 mm displacement [124]. Cohesives and impactor are removed in the models; shell thickness is shown.

6.3.2 High-rate domain

The force-displacement and energy-displacement diagrams of the tube HR experiments and the three simulations are presented in Figure 6-24a and Figure 6-24b. The corresponding damage patterns of a typical experiment and the simulations within and after the trigger phase are given in Figure 6-25. In addition, Table 6-3 provides an overview of the maximum initiation force, SSCS, and MCSD for experiments and simulations. The experiments reached an average maximum initiation force value of 80.0 kN, an SSCS of 65.8 J/g, and an MCSD of 10.2 kN. CVs are lower than 10% except from the MCSD, which surpasses 30%. It should also be noted that the SSCS values in this thesis deviate from the values by Courteau. He did not report detailed input values for his calculations, e.g., volume measurements or each specimen's designated start of the stable crushing phase.

The 1S_HR model creates a maximum force that agrees well with the experimental value (84.0 kN). The SSCS is also close to the experimentally observed value (79.3 J/g), whereas the MCSD as a measure of the force oscillations during crushing is overestimated (18.3 kN). This overestimation occurs because the 1S model does not allow for the characteristic simultaneous inward and outward bending of the fronds, as already stated multiple times (see Figure 6-25b and Figure 6-25f).

The 2S_HR modeling approach yields a good agreement with the experiments regarding the maximum force (90.8 kN) and SSCS (78.9 J/g). Even though this model can replicate the splaying failure mode of the experiments over the whole crushing length (see Figure 6-25a, Figure 6-25c, Figure 6-25e, and Figure 6-25g), the extent of the force oscillations and therefore the MCSD is underestimated (3.7 kN). During the stable crushing phase, the model can also evaluate the occurring SRs in the damage zone. The fringe plots of the intralaminar and interlaminar SR fields show values of above 5,000 1/s (see Figure 6-26a and Figure 6-26b). These rates are again multiple times higher than the nominal value in the range of 30 1/s but compare well to the values observed in the TTT HR crushing models (see Figure 6-16c and Figure 6-16d).

The 16S_HR model fails to replicate any of the experimental crushing characteristics from the trigger phase onwards and produces buckling failure instead (see Figure 6-25d and Figure 6-25h). Again, this can be attributed to the out-of-plane tensile strength T_0, which had to be reduced by a factor of about 15 compared to the experimentally determined value. To further investigate the influence of T_0 and the applied mesh size, Section 6.3.3 contains an additional numerical study.

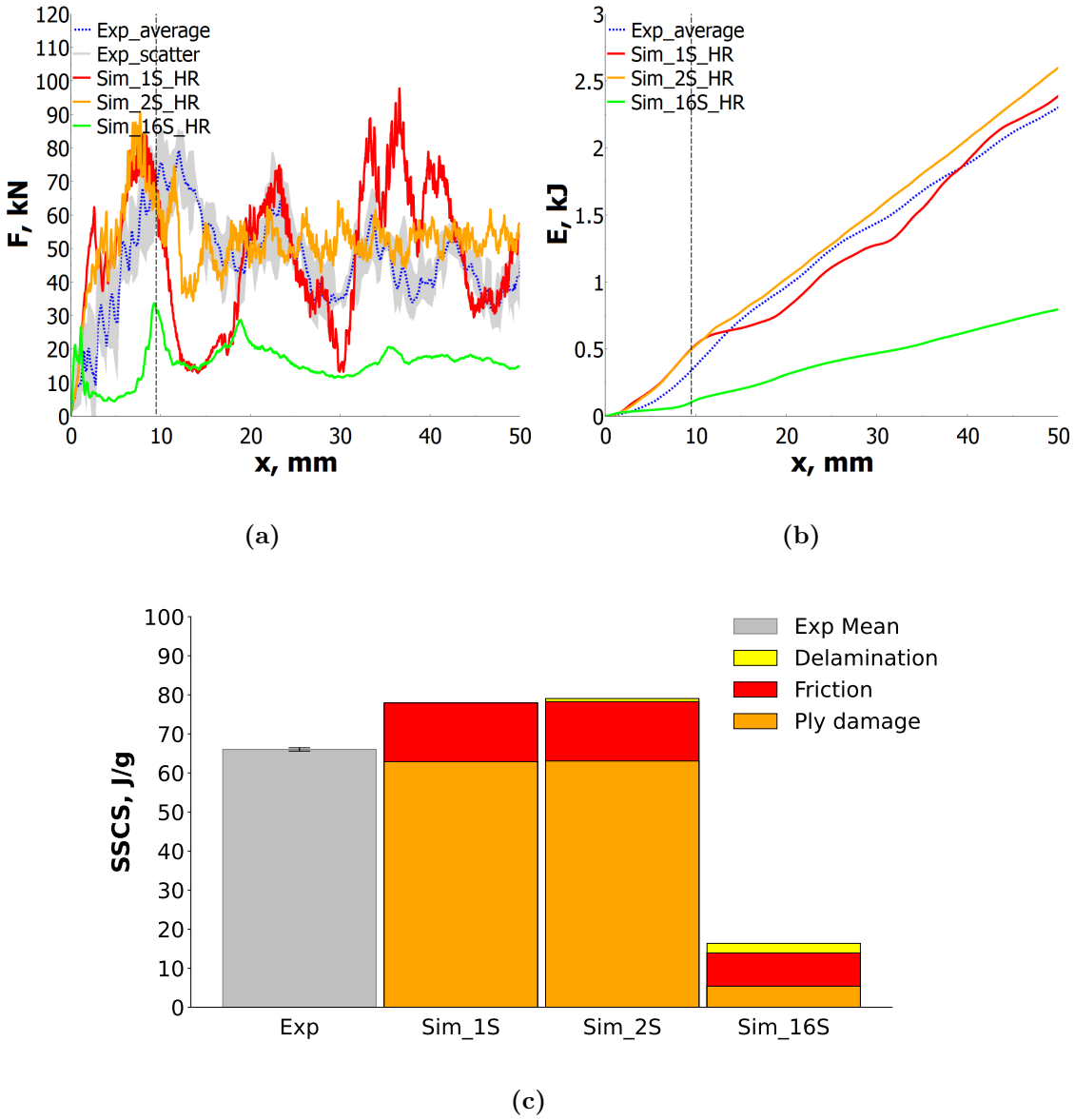

Fig. 6-24 (a) Comparison of stress-displacement average and scatter band from HR experiments with the corresponding numerical variants 1S, 2S, and 16S. Comparison of (b) the corresponding energy-displacement curves and (c) mean energy absorption and standard deviation from HR experiments and energy breakdowns for the evaluable numerical variants at 50 mm displacement. The vertical line in the curve plots indicates the end of the trigger length (9.5 mm).

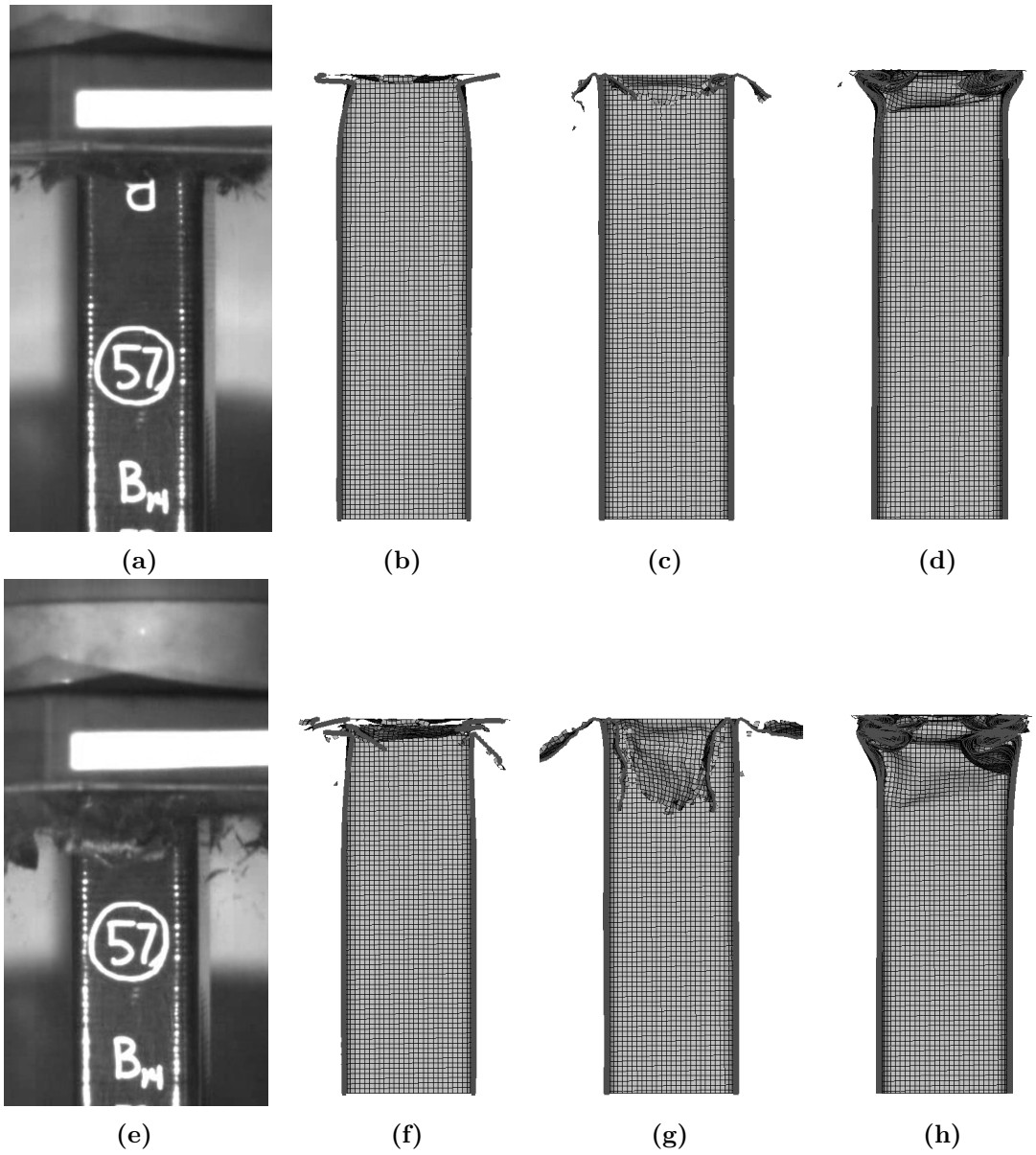

(a) **(b)** **(c)** **(d)**

(e) **(f)** **(g)** **(h)**

Fig. 6-25 Failure patterns of HR crushing experiment and simulations: failure pattern at 20 mm displacement in (a) 57B crushing experiment, (b) 1S, (c) 2S, and (d) 16S model cuts along the tube's longitudinal axis. Subfigures (e) to (h) show experiment 57B and the 1S, 2S, and 16S model cuts at 50 mm displacement [44]. Cohesives and impactor are removed in the models; shell thickness is shown.

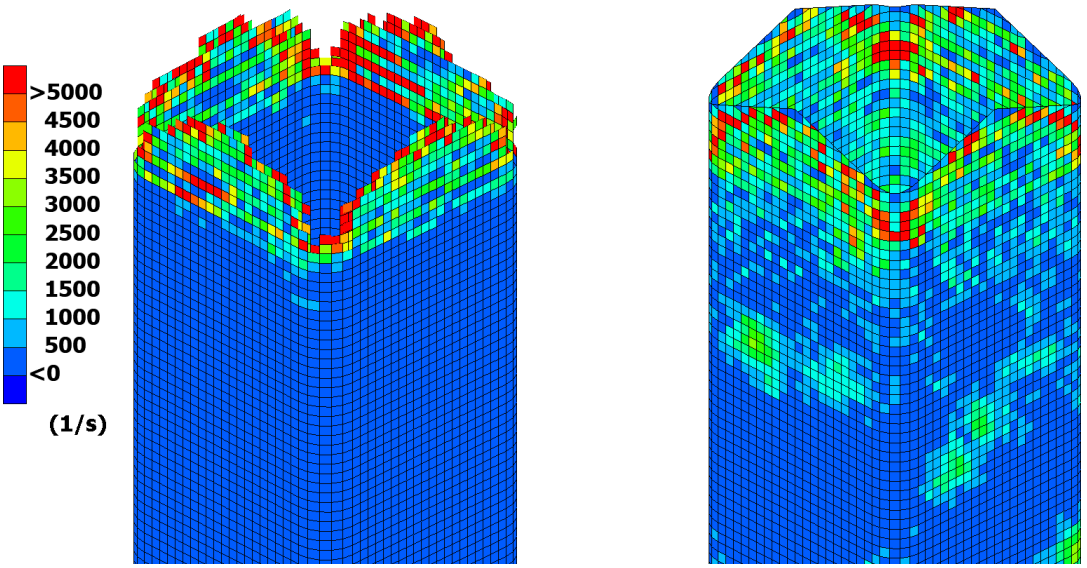

Fig. 6-26 (a) Isometric view onto (a) intralaminar and (b) interlaminar SR field in the 2S_HR model at 20 mm displacement and with a uniform color scale.

6.3.3 Additional numerical study and summary assessment

Table 6-5 summarizes the results of the QS and HR tube crushing experiments and simulations.

Tab. 6-5 Overview of maximum initiation force, SSCS, and MCSD for tube crushing experiments and simulations (color code for deviation from experimental average values: <10% green, 10-15% yellow, 15-20% orange, >20% red).

Maximum Initiation Force				
Sim/Exp[a]	Denomination	Value	Denomination	Value
Exp	QS Mean	73.7 kN	HR Mean	80.0 kN
Exp	QS STDV	-	HR STDV	7.3 kN
Exp	QS CV	-	HR CV	9.1%
Sim	1S_QS	41.3 kN	1S_HR	84.0 kN
Sim	2S_QS	28.2 kN	2S_HR	90.8 kN
Sim	16S_QS	13.8 kN	16S_HR	33.7 kN
SSCS				
Sim/Exp	Denomination	Value	Denomination	Value
Exp	QS Mean	77.4 J/g	HR Mean	65.8 J/g
Exp	QS STDV	-	HR STDV	0.6 J/g
Exp	QS CV	-	HR CV	1.0%
Sim	1S_QS	32.1 J/g	1S_HR	79.3 J/g
Sim	2S_QS	24.7 J/g	2S_HR	78.9 J/g

Sim	16S_QS	12.2 J/g	16S_HR	24.4 J/g
MCSD				
Sim/Exp	Denomination	Value	Denomination	Value
Exp	QS Mean	5.0 kN	HR Mean	10.2 kN
Exp	QS STDV	- kN	HR STDV	3.1 kN
Exp	QS CV	-	HR CV	30.1%
Sim	1S_QS	6.5 kN	1S_HR	18.3 kN
Sim	2S_QS	2.6 kN	2S_HR	3.7 kN
Sim	16S_QS	1.3 kN	16S_HR	2.5 kN

[a] Simulation/experiment

The runtimes for all tube crushing simulations are given in Table 6-6. The trend of the runtime increases from 1S to 16S are comparable to the OHC and TTT simulations. The duration of the QS simulations is up to 150% higher than for HR, since the lower impact velocity prolongs the numerical runtime and thus counteracts the higher costs of the SR formulation.

Tab. 6-6 Model size and runtime comparison for tube crushing simulations (time step: 1.2E-7).

QS	Elements	Runtime (s)
1S	12,328	3,155
2S	22,156	4,259
16S	147,420	75,271
HR	Elements	Runtime (s)
1S	12,328	1,497
2S	22,156	1,798
16S	147,420	29,835

As mentioned above, an additional simulation can illustrate the influence that the mesh size and the out-of-plane strength reduction have on the crushing response. To facilitate the comparison of a 2 mm mesh with a 0.3 mm mesh, the runtime-efficient TTT crushing coupons are used again. Figure 6-27 shows the TTT crushing geometries with the two purely rhomboid meshes. Figure 6-28a is the force-displacement diagram of the two variants. The 2 mm mesh variant cannot provide an accurate force response in the coupon-crushing model. The force level is already overestimated during the trigger load increase and subsequently drops to zero due to global delamination and one-sided buckling of all plies, as can be seen in Figure 6-28b and Figure 6-28c. This behavior resembles the failure pattern observed in the 16S crushing tubes (see Figure 6-28d).

FE models of different through-thickness discretization were used to predict the results of tube crushing experiments: SSMs (1S), SLMs (2S), and DPMs (16S). Due

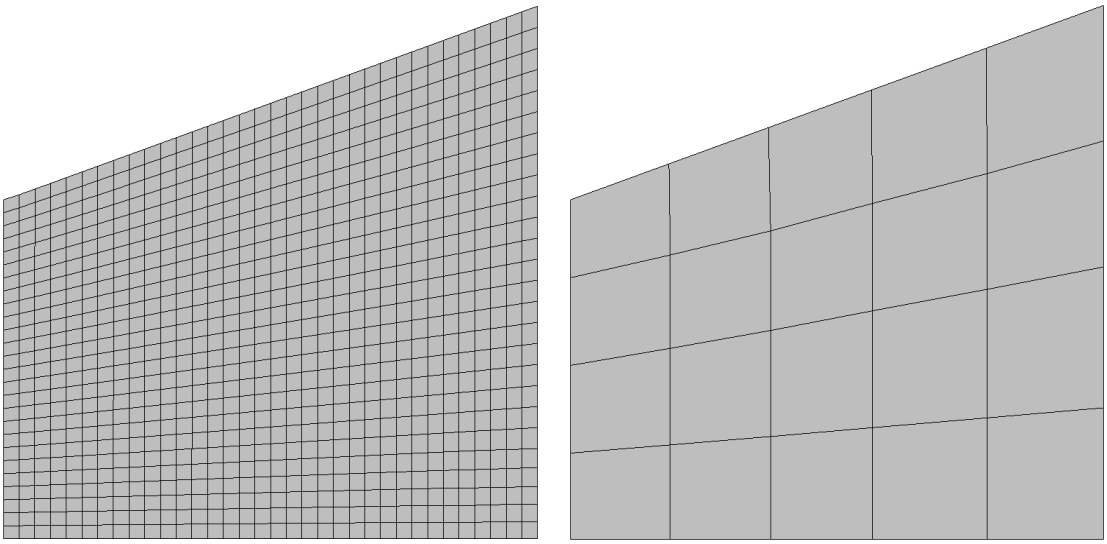

(a) (b)

Fig. 6-27 TTT crushing coupon geometries with (a) 0.3 mm mesh size and (b) 2 mm mesh size.

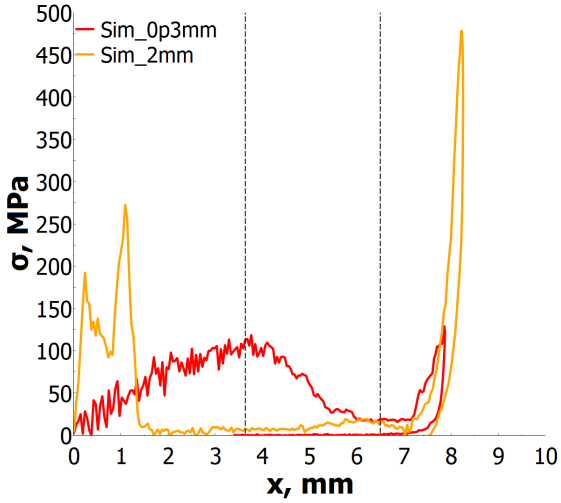

(a)

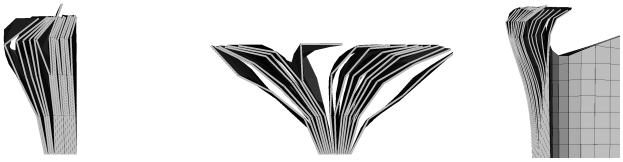

(b) (c) (d)

Fig. 6-28 (a) Stress-displacement curves of TTT crushing mesh size variants. Failure pattern of coupon geometry with 2 mm mesh size at (b) 1.5 mm displacement and (c) 3 mm displacement. (d) Section cut of crushing tube damage in the trigger area at 2.5 mm displacement.

to premature element erosion, none of the models is able to replicate crushing under QS loading. In the HR domain, SSM simulations produce high force fluctuations caused by their missing capability to reproduce splaying failure, whereas DPMs show unrealistic delamination failure. It can be stated that DPM crushing simulations using current CZMs can only be predictive in combination with sufficiently small elements, which do not require strength parameter reductions. Therefore, SLMs are the only models in this thesis that can correctly predict the failure mode and force level of a crushing tube under HR loading.

7 Conclusion

Fiber-reinforced plastics are often used in applications that require high specific stiffness and strength, e.g., wind turbines and aircraft. However, they can also be employed to make lightweight structures more crashworthy. Use cases comprise racing cars, helicopters, or aircraft of different categories. The envisaged high energy absorption capacities per mass when compared to metals can be reached thanks to crushing failure. As shown in Chapter 1, crushing is the destructive loading of composite profiles in the axial direction or with an off-axis exposure angle. It is the result of a combination of splaying and fragmentation failure caused by various failure mechanisms, such as fiber fracture or delamination. The failure mechanisms in a crushing structure show complex interactions and depend, among other things, on the properties of the constituent materials. The dependencies also include strain-rate-induced changes in the material response. Therefore, the design of crush-loaded absorber structures typically requires extensive and costly experimental campaigns. To improve the understanding of crushing and speed up the design of future composite applications, numerical methods such as finite element simulations are an attractive research subject. The research question for this doctoral thesis was therefore posed as follows:

Under which conditions can finite element models replicate composite crushing, and what role do strain-rate-induced property changes play for their predictive quality?

A literature review in Chapter 2 covered relevant studies on the simulation of 3D crushing components. Studies were clustered according to the through-thickness discretization of the applied models: single-shell models, stacked-laminate models, discrete-ply models, and multi-layered-ply models. Models with refined out-of-plane resolutions showed increased predictive capabilities because they were able to correctly predict ply debonding, which is essential to replicate splaying failure. In addition, a limited number of studies considering the influence of strain rates on the crushing process could be identified. Crushing of profile components is a superposition of the material response and the geometrical influence, which can lead to, e.g., ply tearing in corner sections. Flat coupon geometries can be investigated to minimize the influence of the geometry and the required material amount in experiments. Therefore, an overview of publications on the experimental and numerical evaluation of 2D crushing coupons was also given: Different designs of experimental setups were identified, whereby the specimen is either guided through a crushing fixture or clamped and crushed by an impactor. The literature review was concluded by an outline of publications that dealt with the simulation of coupon

crushing. It was found that only a few studies reported successful, physics-based predictions of the crushing behavior for flat coupon specimens.

In order to reach a high predictive quality with the numerical models, the most extensively studied fiber-reinforced plastic material, carbon/epoxy uni-directional IM7/8552 was selected for the evaluations. In Chapter 3, all relevant properties of the material system were collected and discussed with particular regard to the extrapolations of property values under elevated strain rates. Apart from tensile elasticity and strength in the longitudinal direction and the interlaminar fracture toughnesses, all material properties were considered strain-rate-dependent.

Chapter 4 outlined the experimental efforts of the present thesis along with experimental data taken from literature. Scaled-down open-hole compression specimens manufactured from IM7/8552 were tested on a universal testing machine and a split-Hopkinson bar system. The experiments facilitated the evaluation of a notched coupon geometry under quasi-static and high-rate loading. Subsequently, experiments with IM7/8552 triangular through-thickness trigger specimens based on a geometry from the literature were conducted on a universal testing machine and a drow-tower setup. Again, the specimens were tested under two loading rate regimes. Finally, data from IM7/8552 tube-crushing experiments with a quasi-isotropic layup and tulip trigger were taken from the literature. The available datasets comprised quasi-static experiments on a universal testing machine and high-rate experiments on a servo-hydraulic testing machine. Each of the three experimental series was evaluated based on three key figures, e.g., maximum stress, crushing stress, and specific energy absorption in the case of crushing specimens.

Chapter 5 started with the presentation of the commercial continuum damage model *MAT_058 implemented in the explicit finite element solver LS-DYNA. The model was selected due to its runtime efficiency and transferability to full-scale structures. Throughout the thesis, it was applied to model plies or ply stacks. Even though the formulation of the model has been used for many years, considering rate dependencies that were essential for the studies has only been possible recently. A novel framework was introduced, taking into account fracture toughnesses to increase the physical motivation of the formulation. Also, parameter and single-element studies were successfully conducted to rule out numerical influences on the simulation results. To be able to account for ply debonding, *MAT_240 corresponding with *CONTACT_..._TIEBREAK option 14 was selected. The underlying cohesive zone formulation is governed by a traction-separation law, which also facilitates the consideration of strain rate sensitivities. Extensive studies were carried out in constant comparison with experimental data to face the well-known mesh size sensitivity of cohesive zone models. The results of the final mode I and II delamination simulations showed excellent agreement with the experiments. Furthermore, the

modeling approaches for the three experimental geometries were presented: They comprised single-shell models, stacked-laminate models, and discrete-ply models each. Open-hole compression and Triangular through-thickness trigger specimens were meshed with fine quadrilateral elements of 0.3 mm length, whereas the tube geometry was meshed with a coarser 2.0 mm element length. Finally, additional settings and boundary conditions employed in the models were discussed.

Chapter 6 comprised the experimental and numerical results of the open-hole compression, triangular through-thickness trigger crushing, and tube crushing studies. The triangular through-thickness trigger experiments proved to be a cost-efficient alternative to high-speed crushing studies on the component level. Apart from the mean crushing stress deviation in the tube crushing experiments, none of the coefficients of variation exceeded a value of 15%. Thus, the experiments were considered a reliable database for validating the numerical models. A final overview of the numerical predictive capability of the simulations is presented in Table 7-1. For each model, the average value of the deviations between experiments and simulation was calculated from the three key figures. Thus, the Composite Materials Handbook-17 Crashworthiness Working Group's success criteria can be reapplied. The open-hole compression models mainly reach fair to excellent agreement with the experiments. Through-thickness model refinement leads to an improvement of the results. However, there is an intrinsic tendency of *MAT_058 to fail prematurely in the 0° plies, which deteriorates the predictive performance of the discrete-ply model. This early failure occurs because the material model lacks a consideration of plastic deformation. The triangular through-thickness trigger-crushing models are only able to reach a poor to fair predictive quality and show the same trend of improvement when better out-of-plane resolutions are employed. For the quasi-static models, deviations are mainly caused by the element erosion in LS-DYNA, which is inappropriate when scaled velocities are applied. Subsequently, an original-velocity stacked-laminate model produced the best prediction of the force-displacement characteristic and failure pattern. For the high-rate studies, the discrete-ply model provided the most accurate results. Similar to the open-hole compression simulations, deviations can be attributed to premature failure of the 0° plies. Throughout the tube crushing validation, all models showed poor performance. This inadequacy can be traced back to the element size, which affects the response of the cohesive zone model: To accurately predict the double-cantilever beam experiments with 2.0 mm element length, the out-of-plane tensile strength had to be reduced. This calibration promotes unphysical buckling failure of the tubes and was also replicated on the coupon level using a 2.0 mm triangular through-thickness trigger model.

Tab. 7-1 Overview of averaged correlation between experiments and simulation derived from the three key figures of each numerical model. The value can be seen as global success criterion for each model (color code for averaged deviation from experimental average values: <10% green, 10-15% yellow, 15-20% orange, >20% red).

Open-hole compression	quasi-static	high-rate
Single-shell model	77.7%	83.8%
Stacked-laminate model	88.0%	98.3%
Discrete-ply model	82.8%	90.2%
Triangular through-thickness trigger crushing	**quasi-static**	**high-rate**
Single-shell model	64.5%	49.3%
Stacked-laminate model[a]	89.5%[a]	55.7%
Discrete-ply model	86.8%	75.4%
Tube crushing	**quasi-static**	**high-rate**
Single-shell model	58.1%	78.0%
Stacked-laminate model	40.7%	69.3%
Discrete-ply model	20.2%	34.6%

[a] 4S_MR_1mmps

Based on the previous results and additional crushing studies, the following conclusions can be formulated in response to the research question:

- **Boundary conditions**: Neither the friction coefficient within a physically reasonable range nor the representation of the impactor show a clear influence on the crushing response in the present investigations.
- **Intralaminar modeling**: When compared to rectangular meshes, rhomboid meshes create a smoother and more realistic force response in crushing models. Unlike staggered stacked-laminate models [54, 60], the resulting geometrical discretizations are compatible with cohesive zone elements. The intralaminar element deletion scheme plays a huge role for the comparability of the numerical results with experiments – in particular for quasi-static models with scaled velocity. Great attention should be paid to the material model: the influence of the damage-softening law that was also described by another author, should be accounted for [45]. Here, a linear strain-softening definition could be the simplest yet accurate approach [131]. Furthermore, plastic deformation should be considered in the material formulation to facilitate correct replications of the residual stiffnesses [147].
- **Interlaminar modeling**: Debonding interfaces between laminate plies or ply stacks are a particularly sensitive influencing factor on the model behavior. The results indicate that physics-based material data should be included in the models. The mesh size should be reduced to an uncritical element

length to facilitate stable delamination behavior without the need to reduce interlaminar strength values, above all for crack opening mode I. Otherwise, novel methods can be employed that make the models more or completely mesh-size-independent [61, 140]. To receive a first estimate of the crushing behavior, single-shell models are recommended. However, genuinely predictive crushing simulations can only be obtained when every ply of a composite laminate is discretized during the crushing process.

- **Simulation runtimes**: Strain-rate-dependent material formulations lead to runtime increases of about 50% when identical loading velocities are applied. Furthermore, increase factors of 20 to 40 are observed over the evaluated geometries when discrete-ply models are used instead of single-shell models. Stacked-laminate models seem to provide a viable compromise even though calibration of interlaminar failure properties, e.g., conducted by Chen et al., should be subject to future studies [55].
- **Strain rate dependencies**: Strain rate sensitivities affect a variety of interacting mechanisms, such as delamination or matrix fracture, and can have a significant influence on the crushing behavior. In the numerical models, strain rate values above 5,000 1/s were observed during stable crushing for both the triangular through-thickness trigger and tube crushing simulation models. The triangular through-thickness trigger discrete-ply models show that the strain rate influence on the laminate level does not necessarily follow the expected ply-level increase of most property values. Instead, they suggest that rate-induced intralaminar property value increases promote interlaminar delamination. Still, it should be considered, that the present studies on coupon level refer to a short stable crushing length. Results of Feser, who also used IM7/8552, indicate that strain rate dependencies become less relevant during the stable crushing phase [45]. However, other authors reported decreased energy absorption capacities of their carbon fiber/epoxy materials at higher loading rates [8, 70]. Hence, the effect of strain-rate-dependent properties on composite crushing failure requires further investigation.

8 Outlook

As summarized in the conclusion, physics-motivated stacked-shell models of composite crushing presented in this thesis showed predictive results for small-scale specimens. Persisting deviations toward the experiments were attributed to limitations of the material model, the element deletion algorithm, and insufficient resolution of the interlaminar fracture process zone.

Apart from considering plastic behavior in the material models, as discussed in Chapter 7, further academic study in the field of crushing simulation should be dedicated to models with 3D damage formulation and homogenized solid element models. These models would facilitate the research of out-of-plane stresses and pretensioning on the crushing process which could not be covered with the 2D shell models in the present thesis. In addition, strain rate effects should be further investigated numerically on specimens with longer free crushing distances, e.g., with the crushing fixture proposed by Feraboli (see Figure 2-2b).

In experimental investigation, further efforts should be made to quantify interlaminar damage properties under high strain rates. More research needs to be done in this direction to improve existing experimental methods. For example, in the case of interlaminar fracture toughness characterization, it becomes challenging to reach high loading rates with standard specimens due to their size. Furthermore, research on innovative techniques to study the behavior of composites under very high strain rates seems to be a worthwhile research subject: In this thesis, observed strain rates in the range of 5,000 1/s resulting from a still moderate impact velocity of about 5 m/s exceeded the nominal values by a factor of more than 10. These strain rates are already beyond the values a typical split-Hopkinson bar system can reach.

The numerical framework applied in this thesis was set up to also be transferable to the LuFo CraCpit project. The project comprised all steps of the building block approach presented in Figure 1-3. After the fiber and resin materials had been selected in 2018, extensive testing of the composite material systems took place from 2019 until 2021. The campaign provided a detailed, open-access material database of three typical composites used in sailplane design, also covering strain rate sensitivities of the materials [148]. Other material data, e.g., for metals, foams, or adhesive joints, were taken from the literature. Built-in LS-DYNA material models were chosen, and several component experiments based on Omega-shaped hat profiles were conducted to validate the material response on a level of higher complexity. In the meantime, Akaflieg Munich developed a novel aerobatic sailplane concept. Based on the flight loads and an early-phase cockpit geometry, the concept was refined with crash simulations of the nose cone section. From 2020 on, a

modern crash-reinforced fuselage was manufactured in the workshop of Akaflieg. In parallel, a digital twin of the fuselage was created in LS-DYNA at TUM-LCC. The final model consisted of 1,200,000 elements, where all composite parts were meshed single-shell. This approach had proven its runtime efficiency and sufficient accuracy in the component validations. The model took about 88 hours to complete a simulated time of 450 ms on 28 Intel Xeon E5-2690 v3 (2.6 GHz) cores of Leibniz Supercomputing Center in Garching. To conclude this thesis, the model provides an opportunity to evaluate the influence of strain-rate-induced material changes on a full-scale composite structure. Therefore, the final crash model was rerun, neglecting strain rate dependencies in all composite materials (QS). Thus, the simulation time was reduced to approximately 70 hours.

The results of the crash test and the two simulations facilitate a comparison of the fuselage nose impact. Figure 8-1 shows that the maximum crushing deformations during the nose impact are very similar in both models and that they also resemble the experimental behavior. Still, a closer look at the impact front reveals that the structural response is slightly stiffer when strain rate effects are taken into account in the composite materials (HR). The stiffness increase adds around 30 mm to the minimum remaining nose length in the strain-rate-dependent model. As a result, the initial increase of the X- and Z-acceleration in the coordinate system of the inertial measurement unit is underestimated by the quasi-static model as can be seen in Figure 8-2. However, both models similarly underestimate the rebound of the nose cone, which again points to the incorrect residual stiffness due to the absence of plastic deformation in the applied material model. Overcoming this and the other modeling issues presented in this thesis will make composite crash simulations ever more predictive and can eventually facilitate the certification of structures based on numerical methods only.

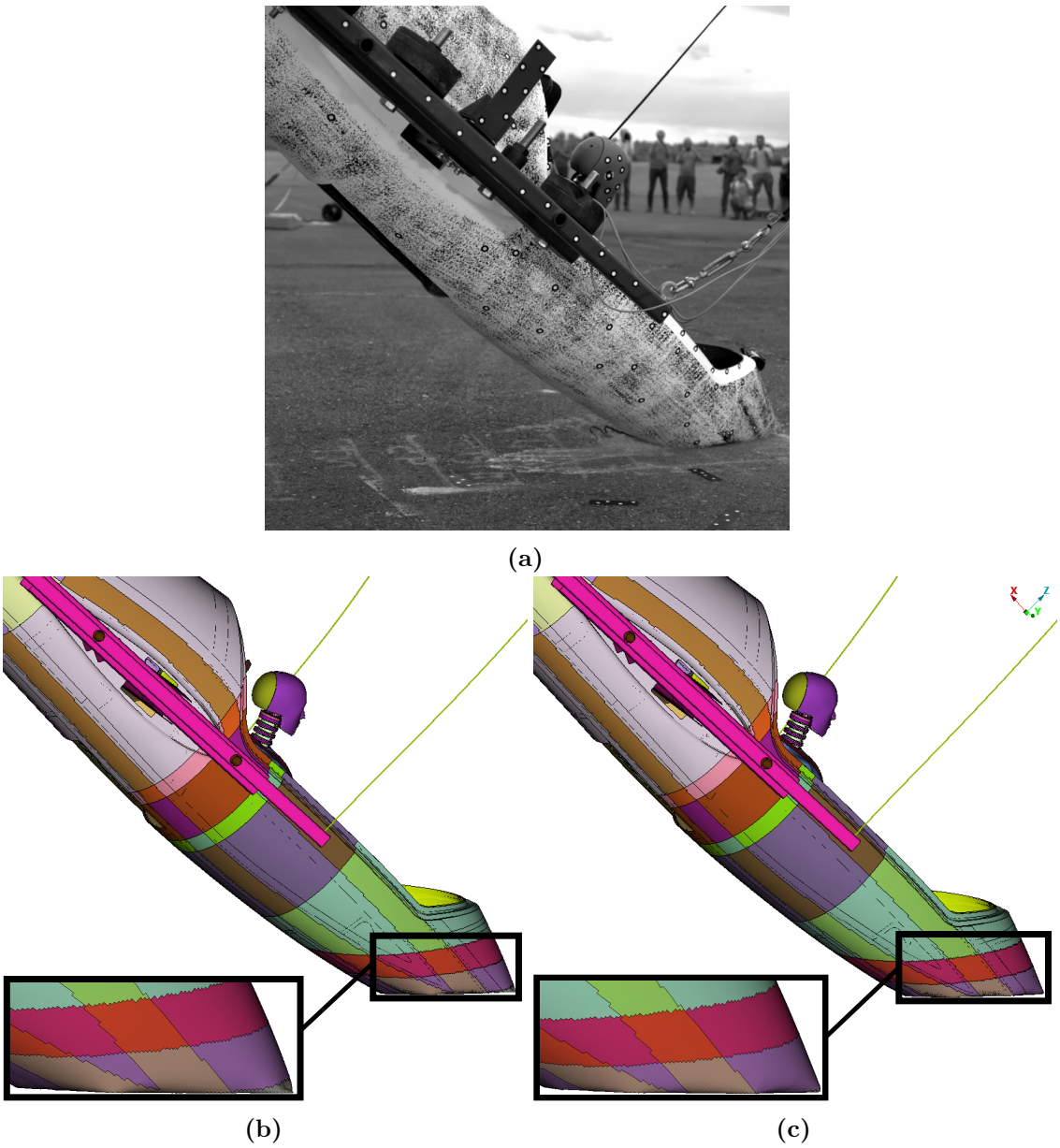

Fig. 8-1 (a) Maximum crushing deformation of the nose cone section during the CraCpit crash test 38 ms after the initial impact. Deformation in the corresponding model (b) with composite strain rate dependencies and (c) without composite strain rate dependencies.

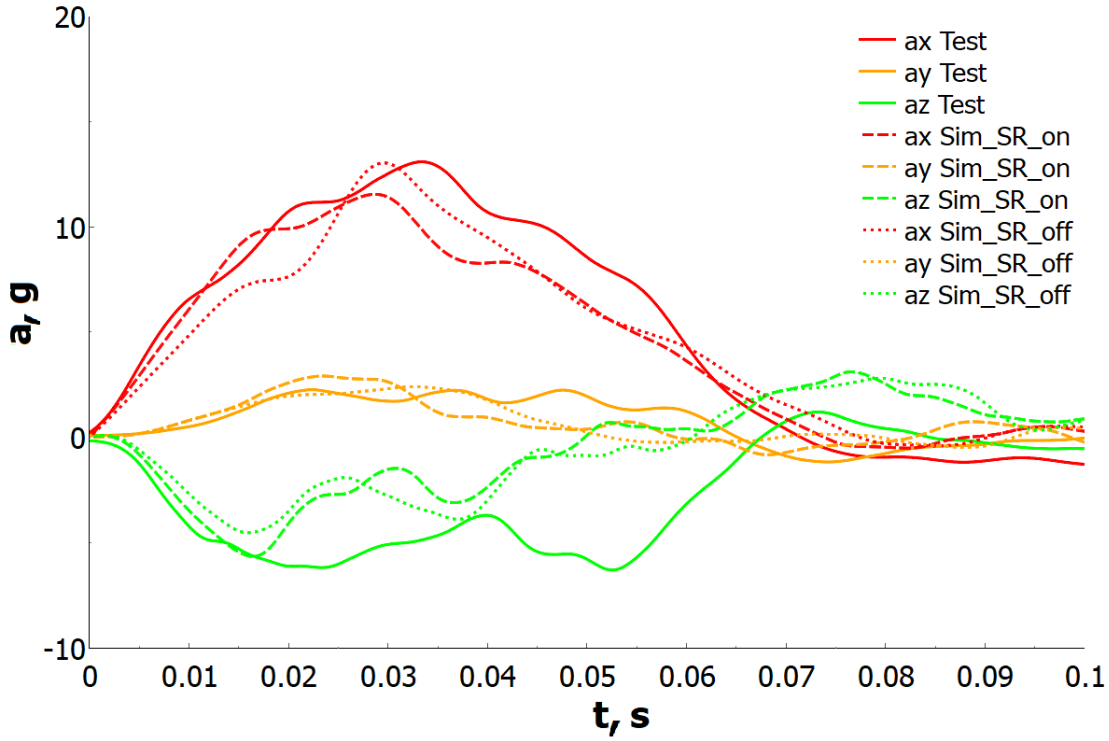

Fig. 8-2 Accelerations in X-, Y-, and Z-direction of the inertial measurement unit during the first 100 ms of the crash experiment (Test), simulation considering strain rate dependencies (Sim_SR_on), and simulation not considering strain rate dependencies (Sim_SR_off). The results were smoothened uniformly with a Butterworth 50 Hz filter [149].

Bibliography

[1] G. E. P. Box, "Science and Statistics," *Journal of the American Statistical Association*, vol. 71, no. 356, pp. 791–799, 1976. doi: 10.1080/01621459.1976.10480949

[2] Akaflieg Stuttgart, "fs24 – Phönix." [Online]. Available: https://akaflieg-stuttgart.de/projekte/fs24-phoenix/

[3] R. Kickert, "Dimensionierungsrichtwerte und Werkstoffkennwerte für den Festigkeitsnachweis von Faserverbundstrukturen im Segel- und Motorsegelflugzeugbau: Idaflieg Faserkatalog." 1988.

[4] Luftfahrt Bundesamt, "Richtlinien zur Führung des Festigkeitsnachweises für Bauteile aus Glasfaser- und Kohlenstofffaserverstärkten Kunststoffen von Segelflugzeugen und Motorseglern." 1991.

[5] European Union Aviation Safety Agency, "Certification specifications for sailplanes and powered sailplanes: CS-22," November 14 2003.

[6] S. Ramakrishna, H. Hamada, Z. Maekawa, and H. Sato, "Energy absorption behavior of carbon-fiber-reinforced thermoplastic composite tubes," *Journal of Thermoplastic Composite Materials*, vol. 8, no. 3, pp. 323–344, 1995. doi: 10.1177/089270579500800307

[7] C. Bisagni, G. Di Pietro, L. Fraschini, and D. Terletti, "Progressive crushing of fiber-reinforced composite structural components of a Formula One racing car," *Composite Structures*, vol. 68, no. 4, pp. 491–503, 2005. doi: 10.1016/j.compstruct.2004.04.015

[8] D. Dalli, L. F. Varandas, G. Catalanotti, S. Foster, and B. G. Falzon, "Assessing the current modelling approach for predicting the crashworthiness of Formula One composite structures," *Composites Part B: Engineering*, vol. 201, p. 108242, 2020. doi: 10.1016/j.compositesb.2020.108242

[9] J. K. Sen, "Designing for a crashworthy all-composite helicopter fuselage," *Journal of the American Helicopter Society*, pp. 56–66, 1987. doi: 10.4050/jahs.32.56

[10] M. A. McCarthy and J. F. M. Wiggenraad, "Numerical investigation of a crash test of a composite helicopter subfloor structure," *Composite Structures*, vol. 51, pp. 345–359, 2001. doi: 10.1016/S0263-8223(00)00150-1

[11] M. Guida, F. Marulo, and S. Abrate, "Advances in crash dynamics for aircraft safety," *Progress in Aerospace Sciences*, vol. 98, pp. 106–123, 2018. doi: 10.1016/j.paerosci.2018.03.008

[12] D. Siromani, "Crashworthy design and analysis of aircraft structures," PhD Thesis, Drexel University, Philadelphia, 2013.

[13] M. Waimer, M. H. Siemann, and T. Feser, "Simulation of CFRP components subjected to dynamic crash loads," *International Journal of Impact Engineering*, vol. 101, pp. 115–131, 2017. doi: 10.1016/j.ijimpeng.2016.11.011

[14] P. H. Thornton, J. J. Harwood, and P. Beardmore, "Fiber-reinforced plastic composites for energy absorption purposes," *Composites Science and Technology*, vol. 24, pp. 275–298, 1985. doi: 10.1016/0266-3538(85)90026-0

[15] D. H. Hull, "A unified approach to progressive crushing of fibre-reinforced composite tubes," *Composites Science and Technology*, vol. 40, no. 4, pp. 377–421, 1991. doi: 10.1016/0266-3538(91)90031-J

[16] G. L. Farley and R. M. Jones, "Crushing characteristics of continuous fiber-reinforced composite tubes," *Journal of Composite Materials*, vol. 26, pp. 37–50, 1992. doi: 10.1177/002199839202600103

[17] M. J. Czaplicki, Robertson Richard E., and P. H. Thornton, "Comparison of bevel and tulip triggered pultruded tubes for energy absorption," *Composites Science and Technology*, vol. 40, pp. 31–46, 1991. doi: 10.1016/0266-3538(91)90041-M

[18] A. Matzenmiller and K. Schweizerhof, "Crashworthiness analysis of composite structures. A first step with explicit time integration," in *Nonlinear computational mechanics: State of the art*, P. Wriggers and W. Wagner, Eds. Berlin: Springer, 1991.

[19] H. Koerber, "Mechanical response of advanced composites under high strain rates," PhD Thesis, University of Porto, Porto, 2010.

[20] H. Koerber and P. P. Camanho, "High strain rate characterisation of unidirectional carbon-epoxy IM7-8552 in longitudinal compression," *Composites Part A: Applied Science and Manufacturing*, vol. 42, no. 5, pp. 462–470, 2011. doi: 10.1016/j.compositesa.2011.01.002

[21] P. Kuhn, M. Ploeckl, and H. Koerber, "Experimental investigation of the failure envelope of unidirectional carbon-epoxy composite under high strain rate transverse and off-axis tensile loading," in *EPJ Web of Conferences*, EDP Sciences, Ed., vol. 94, 2015. doi: 10.1051/epjconf/20159401040

[22] M. Ploeckl, P. Kuhn, J. Grosser, M. Wolfahrt, and H. Koerber, "A dynamic test methodology for analyzing the strain-rate effect on the longitudinal compressive behavior of fiber-reinforced composites," *Composite Structures*, vol. 180, pp. 429–438, 2017. doi: 10.1016/j.compstruct.2017.08.048

[23] H. Koerber, P. Kuhn, M. Ploeckl, F. Otero, P.-W. Gerbaud, R. Rolfes, and P. P. Camanho, "Experimental characterization and constitutive modeling of the non-linear stress-strain behavior of unidirectional carbon-epoxy under high strain rate loading," *Advanced Modeling and Simulation in Engineering Sciences*, vol. 5, pp. 50–73, 2018. doi: 10.1186/s40323-018-0111-x

[24] J. Richeton, S. Ahzi, K. S. Vecchio, F. C. Jiang, and R. R. Adharapurapu, "Influence of temperature and strain rate on the mechanical behavior of three amorphous polymers: Characterization and modeling of the compressive yield stress," *International Journal of Solids and Structures*, vol. 43, no. 7-8, pp. 2318–2335, 2006. doi: 10.1016/j.ijsolstr.2005.06.040

[25] C. Bauwens-Crowet, "The compression yield behaviour of polymethyl methacrylate over a wide range of temperatures and strain-rates," *Journal of Materials Science*, vol. 8, no. 7, pp. 968–979, 1973. doi: 10.1007/BF00756628

[26] F. Rietsch and B. Bouette, "The compression yield behaviour of polycarbonate over a wide range of strain rates and temperatures," *European Polymer Journal*, vol. 26, no. 10, pp. 1071–1075, 1990. doi: 10.1016/0014-3057(90)90005-O

[27] X. Yuanming, J. Yuan, and B. Yang, "A statistical model and experimental study of the strain-rate dependence of the strength of fibres," *Composites Science and Technology*, vol. 52, no. 4, pp. 499–504, 1994. doi: 10.1016/0266-3538(94)90032-9

[28] Y. Wang and Y. Xia, "The effects of strain rate on the mechanical behaviour of kevlar fibre bundles: An experimental and theoretical study," *Composites Part A: Applied Science and Manufacturing*, vol. 29, no. 11, pp. 1411–1415, 1998. doi: 10.1016/S1359-835X(98)00038-4

[29] Y. Zhou, D. Jiang, and Y. Xia, "Tensile mechanical behavior of T300 and M40J fiber bundles at different strain rate," *Journal of Materials Science*, vol. 36, no. 4, pp. 919–922, 2001. doi: 10.1023/A:1004803202658

[30] M. Zhang, B. Jiang, C. Chen, D. Drummer, and Z. Zhai, "The effect of temperature and strain rate on the interfacial behavior of glass fiber reinforced polypropylene composites: a molecular dynamics study," *Polymers*, vol. 11, no. 11, pp. 1–18, 2019. doi: 10.3390/polym11111766

[31] European Union Aviation Safety Agency, "Notification of a proposal to issue a certification memorandum: Modelling & simulation - CS-25 structural certification specifications," July 14 2020.

[32] A. Berger, T. Pyttel, and F. Duddeck, "Crash simulation of wound composite tubes based on multi-level modelling," *International Journal of Crashworthiness*, vol. 20, no. 2, pp. 151–164, 2015. doi: 10.1080/13588265.2014.984487

[33] H. Böhm, J. Richter, J. Kim, G. Joo, H.-K. Jang, M. Jeong, A. Hornig, and M. Gude, "Glass-fiber mat/PA6 composite tubes subjected to dynamic axial crush loading—Experimental evaluation and high fidelity modeling of failure phenomena," *Composite Structures*, vol. 319, p. 117115, 2023. doi: 10.1016/j.compstruct.2023.117115

[34] Z. Hashin, "Failure criteria for unidirectional fiber composites," *Journal of Applied Mechanics*, vol. 47, pp. 329–334, 1980. doi: 10.1115/1.3153664

[35] C. J. McGregor, R. Vaziri, A. Poursartip, and X. Xiao, "Simulation of progressive damage development in braided composite tubes under axial compression," *Composites Part A: Applied Science and Manufacturing*, vol. 38, no. 11, pp. 2247–2259, 2007. doi: 10.1016/j.compositesa.2006.10.007

[36] K. V. Williams, R. Vaziri, and A. Poursartip, "A physically based continuum damage mechanics model for thin laminated composite structures," *International Journal of Solids and Structures*, vol. 40, no. 9, pp. 2267–2300, 2003. doi: 10.1016/S0020-7683(03)00016-7

[37] F.-K. Chang and K.-Y. Chang, "A progressive damage model for laminated composites containing stress concentrations," *Journal of Composite Materials*, vol. 21, no. 9, pp. 834–855, 1987. doi: 10.1177/002199838702100904

[38] S. W. Tsai and E. M. Wu, "A general theory of strength for anisotropic materials," *Journal of Composite Materials*, vol. 5, no. 1, pp. 58–80, 1971. doi: 10.1177/002199837100500106

[39] P. Feraboli, "Development of a corrugated test specimen for composite materials energy absorption," *Journal of Composite Materials*, vol. 42, no. 3, pp. 229–256, 2008. doi: 10.1177/0021998307086202

[40] P. Feraboli, B. Wade, F. Deleo, M. Rassaian, M. Higgins, and A. Byar, "LS-DYNA MAT54 modeling of the axial crushing of a composite tape sinusoidal specimen," *Composites Part A: Applied Science and Manufacturing*, vol. 42, no. 11, pp. 1809–1825, 2011. doi: 10.1016/j.compositesa.2011.08.004

[41] Massachusetts Institute of Technology, "CZone Analysis," 2021/09/10. [Online]. Available: https://abaqus-docs.mit.edu/2017/English/SIMACAEANLRefMap/simaanl-c-czoneanalysis.htm

[42] A. Cherniaev, C. Butcher, and J. Montesano, "Predicting the axial crush response of CFRP tubes using three damage-based constitutive models," *Thin-Walled Structures*, vol. 129, pp. 349–364, 2018. doi: 10.1016/j.tws.2018.05.003

[43] J. Reiner, T. Feser, M. Waimer, A. Poursartip, H. Voggenreiter, and R. Vaziri, "Axial crush simulation of composites using continuum damage mechanics: FE software and material model independent considerations," *Composites Part B: Engineering*, vol. 225, p. 109284, 2021. doi: 10.1016/j.compositesb.2021.109284

[44] Oak Ridge National Laboratory, "Crashworthiness of carbon fiber composites," 2021/09/10. [Online]. Available: https://energy.ornl.gov/CFCrush/rate_tests/rate_tests.cgi

[45] T. Feser, "Development of a simulation methodology to predict the energy absorption of composite structures under crush loading," PhD thesis, Universität Stuttgart, Deutsches Zentrum für Luft- und Raumfahrt, Stuttgart, 2022.

[46] X. Xiao, M. E. Botkin, and N. L. Johnson, "Axial crush simulation of braided carbon tubes using MAT58 in LS-DYNA," *Thin-Walled Structures*, vol. 47, no. 6-7, pp. 740–749, 2009. doi: 10.1016/j.tws.2008.12.004

[47] J. Huang and X. Wang, "Numerical and experimental investigations on the axial crushing response of composite tubes," *Composite Structures*, vol. 91, no. 2, pp. 222–228, 2009. doi: 10.1016/j.compstruct.2009.05.006

[48] D. Siromani, J. Awerbuch, and T.-M. Tan, "Finite element modeling of the crushing behavior of thin-walled CFRP tubes under axial compression," *Composites Part B: Engineering*, vol. 64, pp. 50–58, 2014. doi: 10.1016/j.compositesb.2014.04.008

[49] M. David and A. F. Johnson, "Effect of strain rate on the failure mechanisms and energy absorption in polymer composite elements under axial loading," *Composite Structures*, vol. 122, pp. 430–439, 2015. doi: 10.1016/j.compstruct.2014.11.010

[50] N. Feindler, "Charakterisierungs- und Simulationsmethodik zum Versagensverhalten energieabsorbierender Faserverbundstrukturen," PhD Thesis, Technical University of Munich, Munich, 2012.

[51] C. Reuter, K.-H. Sauerland, and T. Tröster, "Experimental and numerical crushing analysis of circular CFRP tubes under axial impact loading," *Composite Structures*, vol. 174, pp. 33–44, 2017. doi: 10.1016/j.compstruct.2017.04.052

[52] C. McGregor, R. Vaziri, and X. Xiao, "Finite element modelling of the progressive crushing of braided composite tubes under axial impact," *International Journal of Impact Engineering*, vol. 37, no. 6, pp. 662–672, 2010. doi: 10.1016/j.ijimpeng.2009.09.005

[53] C. McGregor, N. Zobeiry, R. Vaziri, A. Poursartip, and X. Xiao, "Calibration and validation of a continuum damage mechanics model in aid of axial crush simulation of braided composite tubes," *Composites Part A: Applied Science and Manufacturing*, vol. 95, pp. 208–219, 2017. doi: 10.1016/j.compositesa.2017.01.012

[54] J. Striewe, C. Reuter, K.-H. Sauerland, and T. Tröster, "Manufacturing and crashworthiness of fabric-reinforced thermoplastic composites," *Thin-Walled Structures*, vol. 123, pp. 501–508, 2018. doi: 10.1016/j.tws.2017.11.011

[55] D. Chen, X. Sun, B. Li, Y. Liu, T. Zhu, and S. Xiao, "On crashworthiness and energy-absorbing mechanisms of thick CFRP structures for railway vehicles," *Polymers*, vol. 14, no. 22, p. 4795, 2022. doi: 10.3390/polym14224795

[56] D. E. Sommer, D. Thomson, O. Falcó, G. Quino, H. Cui, and N. Petrinic, "Damage modelling of carbon fibre composite crush tubes: Numerical simulation and experimental validation of drop weight impact," *Composites Part A: Applied Science and Manufacturing*, vol. 160, p. 107033, 2022. doi: 10.1016/j.compositesa.2022.107033

[57] V. S. Sokolinsky, K. C. Indermuehle, and J. A. Hurtado, "Numerical simulation of the crushing process of a corrugated composite plate," *Composites Part A: Applied Science and Manufacturing*, vol. 42, no. 9, pp. 1119–1126, 2011. doi: 10.1016/j.compositesa.2011.04.017

[58] R. Matheis, B. Kuckhoff, L. Eckstein, and T. Gries, "Beitrag zum Fortschritt im Automobilleichtbau durch die Entwicklung von Crashabsorbern aus textilverstärkten Kunststoffen auf Basis geflochtener Preforms und deren Abbildung in der Simulation (Geflochtener FVK-Crashabsorber)," *FAT-Schriftenreihe*, vol. 246, 2013.

[59] B. P. Bussadori, K. Schuffenhauer, and A. Scattina, "Modelling of CFRP crushing structures in explicit crash analysis," *Composites Part B: Engineering*, vol. 60, pp. 725–735, 2014. doi: 10.1016/j.compositesb.2014.01.020

[60] Y. Ren, H. Jiang, B. Gao, and J. Xiang, "A progressive intraply material deterioration and delamination based failure model for the crashworthiness of fabric composite corrugated beam: Parameter sensitivity analysis," *Composites Part B: Engineering*, vol. 135, pp. 49–71, 2018. doi: 10.1016/j.compositesb.2017.09.072

[61] D. Karagiozova, P. B. Ataabadi, and M. Alves, "Finite element modeling of CFRP composite tubes under low velocity axial impact," *Polymer Composites*, vol. 42, no. 3, pp. 1543–1564, 2021. doi: 10.1002/pc.25923

[62] P. B. Ataabadi, D. Karagiozova, and M. Alves, "Finite element modeling of crushing of CFRP cylindrical tubes under low-velocity axial impact," *Composite Structures*, vol. 280, p. 114902, 2022. doi: 10.1016/j.compstruct.2021.114902

[63] ——, "Crushing and energy absorption mechanisms of carbon fiber-epoxy tubes under axial impact," *International Journal of Impact Engineering*, vol. 131, pp. 174–189, 2019. doi: 10.1016/j.ijimpeng.2019.03.006

[64] S. Costa, H. Zrida, R. Olsson, M. Herráez, and R. Östlund, "A unified physically-based finite deformation model for damage growth in composites," *Composites Part A: Applied Science and Manufacturing*, vol. 161, p. 107103, 2022. doi: 10.1016/j.compositesa.2022.107103

[65] P. Ladevèze, "A damage computational method for composite structures," *Computers & Structures*, vol. 44, no. 1-2, pp. 79–87, 1992. doi: 10.1016/0045-7949(92)90226-P

[66] P. Ladevèze, O. Allix, L. Gornet, D. Lévêque, and L. Perret, "A computational damage mechanics approach for laminates: Identification and comparison with experimental results," in *Studies in applied mechanics : Damage mechanics in engineering materials*, G. Z. Voyiadjis, J.-W. W. Ju, and J.-L. Chaboche, Eds. Elsevier, 1998, vol. 46, pp. 481–500. ISBN 0922-5382

[67] E. J. Pineda, "A novel multiscale physics-based progressive damage and failure modeling tool for advanced composite structures," PhD Thesis, University of Michigan, Ann Arbor, 2012.

[68] E. J. Pineda and A. M. Waas, "Numerical implementation of a multiple-ISV thermodynamically-based work potential theory for modeling progressive damage and failure in fiber-reinforced laminates," *International Journal of Fracture*, vol. 182, no. 1, pp. 93–122, 2013. doi: 10.1007/s10704-013-9860-1

[69] F. Rondina, M. P. Falaschetti, N. Zavatta, and L. Donati, "Numerical simulation of the compression crushing energy of carbon fiber-epoxy woven composite structures," *Composite Structures*, vol. 303, p. 116300, 2023. doi: 10.1016/j.compstruct.2022.116300

[70] D. Chen, X. Sun, S. Xiao, G. Yang, B. Yang, T. Zhu, and M. Wang, "On axial crushing behavior of double hat-shaped CFRP and GFRP structures," *Composite Structures*, p. 117117, 2023. doi: 10.1016/j.compstruct.2023.117117

[71] L. N. Chiu, B. G. Falzon, R. Boman, B. Chen, and W. Yan, "Finite element modelling of composite structures under crushing load," *Composite Structures*, vol. 131, pp. 215–228, 2015. doi: 10.1016/j.compstruct.2015.05.008

[72] L. N. Chiu, B. G. Falzon, B. Chen, and W. Yan, "Validation of a 3D damage model for predicting the response of composite structures under crushing loads," *Composite Structures*, vol. 147, pp. 65–73, 2016. doi: 10.1016/j.compstruct.2016.03.028

[73] W. Tan, B. G. Falzon, M. Price, and H. Liu, "The role of material characterisation in the crush modelling of thermoplastic composite structures," *Composite Structures*, vol. 153, pp. 914–927, 2016. doi: 10.1016/j.compstruct.2016.07.011

[74] W. Tan and B. G. Falzon, "Modelling the crush behaviour of thermoplastic composites," *Composites Science and Technology*, vol. 134, pp. 57–71, 2016. doi: 10.1016/j.compscitech.2016.07.015

[75] H. Liu, J. Zhou, Di Zhang, S. Li, and I. Giannopoulos, "Effects of contact friction and ply blocking on the crush behaviour of thin-walled composite structures: A numerical study," *Thin-Walled Structures*, vol. 182, p. 110214, 2023. doi: 10.1016/j.tws.2022.110214

[76] B. G. Falzon, "Computational modelling of the crushing of carbon fibre-reinforced polymer composites," *Philosophical transactions. Series A, Mathematical, physical, and engineering sciences*, vol. 380, no. 2232, p. 20210336, 2022. doi: 10.1098/rsta.2021.0336

[77] K. Wang, L. Zhao, H. Hong, and J. Zhang, "A strain-rate-dependent damage model for evaluating the low velocity impact induced damage of composite laminates," *Composite Structures*, vol. 201, pp. 995–1003, 2018. doi: 10.1016/j.compstruct.2018.06.046

[78] Y. J. Liu, Z. Jiang, and H. M. Wen, "Predicting impact induced delamination of FRP laminates," *International Journal of Impact Engineering*, vol. 137, p. 103436, 2020. doi: 10.1016/j.ijimpeng.2019.103436

[79] D.-H. Kim, S.-Y. Kang, H.-J. Kim, and H.-S. Kim, "Strain rate dependent mechanical behavior of glass fiber reinforced polypropylene composites and its effect on the performance of automotive bumper beam structure," *Composites Part B: Engineering*, vol. 166, pp. 483–496, 2019. doi: 10.1016/j.compositesb.2019.02.053

[80] J. A. Lavoie and J. Morton, "Design and application of a quasistatic crush test fixture for investigating scale effects in energy absorbing composite plates," 1993. [Online]. Available: https://ntrs.nasa.gov/citations/19940008590

[81] ——, "A crush test fixture for investigating energy absorption of flat composite plates," *Experimental Techniques*, vol. 18, no. 6, pp. 23–26, 1994. doi: 10.1111/j.1747-1567.1994.tb00316.x

[82] J. A. Lavoie and S. Kellas, "Dynamic crush tests of energy-absorbing laminated composite plates," *Composites Part A: Applied Science and Manufacturing*, vol. 27, no. 6, pp. 467–475, 1996. doi: 10.1016/1359-835X(95)00058-A

[83] L. Daniel, P. Hogg, and P. Curtis, "The relative effects of through-thickness properties and fibre orientation on energy absorption by continuous fibre composites," *Composites Part B: Engineering*, vol. 30, no. 3, pp. 257–266, 1999. doi: 10.1016/S1359-8368(98)00066-3

[84] S. Cauchi Savona and P. J. Hogg, "Effect of fracture toughness properties on the crushing of flat composite plates," *Composites Science and Technology*, vol. 66, no. 13, pp. 2317–2328, 2006. doi: 10.1016/j.compscitech.2005.11.038

[85] ——, "Investigation of plate geometry on the crushing of flat composite plates," *Composites Science and Technology*, vol. 66, no. 11-12, pp. 1639–1650, 2006. doi: 10.1016/j.compscitech.2005.11.011

[86] P. Feraboli, "Development of a modified flat-plate test specimen and fixture for composite materials crush energy absorption," *Journal of Composite Materials*, vol. 43, no. 19, pp. 1967–1990, 2009. doi: 10.1177/0021998309343025

[87] H. A. Israr, S. Rivallant, and J. J. Barrau, "Experimental investigation on mean crushing stress characterization of carbon–epoxy plies under compressive crushing mode," *Composite Structures*, vol. 96, pp. 357–364, 2013. doi: 10.1016/j.compstruct.2012.09.022

[88] A. V. Duong, S. Rivallant, J.-J. Barrau, C. Petiot, and B. Malherbe, "Influence of speed on the crushing behavior of composite plates," in *ACCM 7 – 7th Asian-Australasian Conference on Composite Materials*, 2010. [Online]. Available: https://hal.science/hal-01852293/

[89] J. Lausch, M. Takla, and H.-G. Schweiger, "Crush testing approach for flat-plate fibrous materials," *Composites Part B: Engineering*, vol. 200, p. 108333, 2020. doi: 10.1016/j.compositesb.2020.108333

[90] R. Gutkin and S. T. Pinho, "Combining damage and friction to model compressive damage growth in fibre-reinforced composites," *Journal of Composite Materials*, vol. 49, no. 20, pp. 2483–2495, 2015. doi: 10.1177/0021998314549614

[91] T. Bru, P. Waldenström, R. Gutkin, R. Olsson, and G. M. Vyas, "Development of a test method for evaluating the crushing behaviour of unidirectional laminates," *Journal of Composite Materials*, vol. 51, no. 29, pp. 4041–4051, 2017. doi: 10.1177/0021998317697811

[92] Y. Ma, S. Jin, and S. Zhang, "Effect of trigger on crashworthiness of unidirectional carbon fibre reinforced polyamide 6 composites," *Plastics, Rubber and Composites*, vol. 47, no. 5, pp. 208–220, 2018. doi: 10.1080/14658011.2018.1466502

[93] H. Liu, B. G. Falzon, and J. P. Dear, "An experimental and numerical study on the crush behaviour of hybrid unidirectional/woven carbon-fibre reinforced composite laminates," *International Journal of Mechanical Sciences*, vol. 164, p. 105160, 2019. doi: 10.1016/j.ijmecsci.2019.105160

[94] D. Guillon, S. Rivallant, J. J. Barrau, C. Petiot, P. Thevenet, and B. Malherbe, "Experimental and numerical study of the splaying mode crush of CFRP laminates," in *ICCM-17 - 17th International Conference on Composite Materials*, 2009. [Online]. Available: https://www.iccm-central.org/Proceedings/ICCM17proceedings/Themes/Behaviour/ENERGY%20ABSORB%20&%20CRASH/INT%20-%20ENERGY%20ABSO%20&%20CRASHW/IF11.1%20Guillon.pdf

[95] H. A. Israr, S. Rivallant, C. Bouvet, and J. J. Barrau, "Finite element simulation of 0°/90° CFRP laminated plates subjected to crushing using a free-face-crushing concept," *Composites Part A: Applied Science and Manufacturing*, vol. 62, pp. 16–25, 2014. doi: 10.1016/j.compositesa.2014.03.014

[96] F. Grotto, S. Rivallant, and C. Bouvet, "Development of a 3D finite element model at mesoscale for the crushing of unidirectional composites: Application to plates crushing," *Composite Structures*, vol. 287, p. 115346, 2022. doi: 10.1016/j.compstruct.2022.115346

[97] W. Tan, B. G. Falzon, and M. Price, "Predicting the crushing behaviour of composite material using high-fidelity finite element modelling," *International Journal of Crashworthiness*, vol. 20, no. 1, pp. 60–77, 2015. doi: 10.1080/13588265.2014.972122

[98] A. Puck and H. Schürmann, "Failure analysis of FRP laminates by means of physically based phenomenological models," *Composites Science and Technology*, vol. 58, no. 7, pp. 1045–1067, 1998. doi: 10.1016/S0266-3538(96)00140-6

[99] G. Catalanotti, P. P. Camanho, and A. T. Marques, "Three-dimensional failure criteria for fiber-reinforced laminates," *Composite Structures*, vol. 95, pp. 63–79, 2013. doi: 10.1016/j.compstruct.2012.07.016

[100] Z. Hashin and A. Rotem, "A fatigue failure criterion for fiber reinforced materials," *Journal of Composite Materials*, vol. 7, no. 4, pp. 448–464, 1973. doi: 10.1177/002199837300700404

[101] B. G. Falzon and P. Apruzzese, "Numerical analysis of intralaminar failure mechanisms in composite structures. Part II: Applications," *Composite Structures*, vol. 93, no. 2, pp. 1047–1053, 2011. doi: 10.1016/j.compstruct.2010.06.022

[102] M. C. Engül and N. Ersoy, "Energy absorption capability of carbon/epoxy composite laminates: A novel numerical approach," *Journal of Reinforced Plastics and Composites*, pp. 1262–1276, 2023. doi: 10.1177/07316844221150619

[103] R. S. Whitehead, C. R. Foreman, and K. Silva, "C-130 Advanced Technology Center wing box conceptual design/cost study," *FAA, Ninth DOD(NASA)FAA Conference on Fibrous Composites in Structural Design, Volume 1*, 1992. [Online]. Available: https://ntrs.nasa.gov/citations/19950022016

[104] D. Dumbacher, "Results of the DC-XA program," in *Space Programs and Technologies Conference*. Reston, Virginia: American Institute of Aeronautics and Astronautics, 1996. doi: 10.2514/6.1996-4317

[105] P. M. Wegner, J. M. Ganley, S. M. Huynrechts, and T. E. Meink, "Advanced grid stiffened composite payload shroud for the OSP launch vehicle," in *2000 IEEE Aerospace Conference*, vol. 4, 2000. doi: 10.1109/AERO.2000.878447 pp. 359–365.

[106] Hexcel Corporation, "HexPly 8552 product data sheet," 2016. [Online]. Available: https://www.hexcel.com/user_area/content_media/raw/HexPly_8552_eu_DataSheet.pdf

[107] C. Pohl, M. Toenjes, C. Liebold, M. Ploeckl, H. Koerber, L. Avila Gray, D. Colin, and K. Drechsler, "Numerical prediction of composite damage behavior: A modeling approach including the strain-rate-dependent material response," *Composite Structures*, vol. 292, p. 115628, 2022. doi: 10.1016/j.compstruct.2022.115628

[108] H. Koerber, J. Xavier, and P. P. Camanho, "High strain rate characterisation of unidirectional carbon-epoxy IM7-8552 in transverse compression and in-plane shear using digital image correlation," *Mechanics of Materials*, vol. 42, pp. 1004–1019, 2010. doi: 10.1016/j.mechmat.2010.09.003

[109] P. P. Camanho and M. Lambert, "A design methodology for mechanically fastened joints in laminated composite materials," *Composites Science and Technology*, vol. 66, pp. 3004–3020, 2006. doi: 10.1016/j.compscitech.2006.02.017

[110] J. Harding and L. M. Welsh, "A tensile testing technique for fibre-reinforced composites at impact rates of strain," *Journal of Materials Science*, vol. 18, pp. 1810–1826, 1983. doi: 10.1007/BF00542078

[111] H. M. Hsiao and I. M. Daniel, "Strain rate behavior of composite materials," *Composites Part B: Engineering*, vol. 29B, pp. 521–533, 1998. doi: 10.1016/S1359-8368(98)00008-0

[112] A. Makeev, G. Seon, Y. Nikishkov, and E. Lee, "Methods for assessment of interlaminar tensile strength of composite materials," *Journal of Composite Materials*, vol. 49, no. 7, pp. 783–794, 2015. doi: 10.1177/0021998314525979

[113] Y. He and A. Makeev, "Nonlinear shear behavior and interlaminar shear strength of unidirectional polymer matrix composites: a numerical study," *International Journal of Solids and Structures*, vol. 51, pp. 1263–1273, 2014. doi: 10.1016/j.ijsolstr.2013.12.014

[114] P. Kuhn, G. Catalanotti, J. Xavier, M. Ploeckl, and H. Koerber, "Determination of the crack resistance curve for intralaminar fiber tensile failure mode in polymer composites under high rate loading," *Composite Structures*, vol. 204, pp. 276–287, 2018. doi: 10.1016/j.compstruct.2018.07.039

[115] P. Kuhn, G. Catalanotti, J. Xavier, P. P. Camanho, and H. Koerber, "Fracture toughness and crack resistance curves for fiber compressive failure mode in polymer composites under high rate loading," *Composite Structures*, vol. 182, pp. 164–175, 2017. doi: 10.1016/j.compstruct.2017.09.040

[116] M. W. Czabaj and J. G. Ratcliffe, "Comparison of intralaminar and interlaminar mode-I fracture toughness of unidirectional IM7/8552 graphite/epoxy composite," *Composites Science and Technology*, vol. 89, pp. 15–23, 2013. doi: 10.1016/j.compscitech.2013.09.008

[117] S. A. Ponnusami, H. Cui, B. Erice, M. V. Pathan, and N. Petrinic, "A wedge-DCB test methodology to characterise high rate mode-I interlaminar fracture properties of fibre composites," in *EPJ Web of Conferences*, EDP Sciences, Ed., vol. 183, 2018. doi: 10.1051/epjconf/201818302052

[118] K. T. O'Brien, W. M. Johnston, and G. J. Toland, "Mode II interlaminar fracture toughness and fatigue characterization of a graphite epoxy composite material," 2010.

[119] M. Yasaee, G. Mohamed, A. Pellegrino, N. Petrinic, and S. R. Hallett, "Strain rate dependence of mode II delamination resistance in through thickness reinforced laminated composites," *International Journal of Impact Engineering*, vol. 107, pp. 1–11, 2017. doi: 10.1016/j.ijimpeng.2017.05.003

[120] P. Maimí, P. P. Camanho, J. A. Mayugo, and C. G. Dávila, "A continuum damage model for composite laminates: Part II – Computational implementation and validation," *Mechanics of Materials*, vol. 39, pp. 909–919, 2007. doi: 10.1016/j.mechmat.2007.03.006

[121] C. Pohl, H. Liu, D. Thomson, L. Avila Gray, D. E. Sommer, and N. Petrinic, "Dynamic crushing of composite coupons: An experimental and numerical study," *Journal of Composite Materials*, vol. 57, no. 26, pp. 4103–4121, 2023. doi: 10.1177/00219983231201997

[122] ASTM International, "Standard test method for determination of the mode II interlaminar fracture toughness of unidirectional fiber-reinforced polymer matrix composites," 2014.

[123] M. Bessa, "Meso-mechanical model of the structural integrity of advanced composite laminates," Master's thesis, University of Porto, Porto, 2010.

[124] M. A. Courteau, "Investigating the crashworthiness characteristics of carbon fiber/epoxy tubes," Master's thesis, University of Utah, Salt Lake City, 2011.

[125] A. Cherniaev, S. Pavlova, A. Pavlov, and V. Komarov, "Prediction of load-bearing capacity of composite parts with low-velocity impact damage: Identification of intra- and inter-ply constitutive models," *Applied Mechanics*, vol. 1, no. 1, pp. 59–78, 2020. doi: 10.3390/applmech1010005

[126] M. Holzapfel, G. Kopp, P. Adamski, H. Eisenhans, J. Christlein, and T. Hambrecht, "Numerische Nachbildung der Crashfront von faserverstärkten Strukturen mit Hilfe von Mehrschalen-modellen," in *6th LS-DYNA Forum*, 2007. [Online]. Available: https://www.dynamore.de/de/download/papers/forum07/material01/numerische-nachbildung-der-crashfront-von/@@download/file/D-I-03.pdf

[127] A. Matzenmiller, J. Lubliner, and R. L. Taylor, "A constitutive model for anisotropic damage in fiber-composites," *Mechanics of Materials*, vol. 20, pp. 125–152, 1995. doi: 10.1016/0167-6636(94)00053-0

[128] K. Schweizerhof, K. Weimar, T. Münz, and T. Rottner, "Crashworthiness analysis with enhanced composite material models in LS-Dyna - Merits and limits," in *5th International LS-DYNA User's Conference*, 1998.

[129] Livermore Software Technology Corporation, "Composite models," 2023/06/16. [Online]. Available: https://ftp.lstc.com/anonymous/outgoing/support/FAQ_kw/composites/mat58

[130] Z. P. Bažant and B. H. Oh, "Crack band theory for fracture of concrete," *Materials and Structures*, vol. 16, pp. 155–177, 1983. doi: 10.1007/BF02486267

[131] J. Xue and K. Kirane, "Effect of the shape of the softening damage law on the predicted tensile fracturing and energy dissipation in textile composites," *International Journal of Damage Mechanics*, vol. 30, no. 5, pp. 786–822, 2021. doi: 10.1177/1056789520986849

[132] Livermore Software Technology Corporation, "LS-DYNA keyword user's manual: Volume I: 09/24/21 (r:14186) LS-DYNA R13," 2023/06/16. [Online]. Available: https://ftp.lstc.com/anonymous/outgoing/jday/manuals/LS-DYNA_Manual_Volume_I_R13.pdf

[133] ——, "LS-DYNA keyword user's manual: Volume II material models: 05/18/22 (r:14717) LS-DYNA R13," 2023/06/16. [Online]. Available: https://ftp.lstc.com/anonymous/outgoing/jday/manuals/LS-DYNA_Manual_Volume_II_R13.pdf

[134] S. Marzi, O. Hesebeck, M. Brede, and F. Kleiner, "A rate-dependent, elasto-plastic cohesive zone mixed-mode model for crash analysis of adhesively bonded joints," in *7th European LS-DYNA Conference*, 2009. [Online]. Available: https://www.dynamore.de/en/downloads/papers/09-conference/papers/B-VI-02.pdf

[135] E. Smith, "The failure of a strain-softening material: I. Analytical approach for a double cantilever beam specimen," *Theoretical and Applied Fracture Mechanics*, vol. 11, no. 1, pp. 59–64, 1989. doi: 10.1016/0167-8442(89)90026-8

[136] R. Massabò and B. N. Cox, "Concepts for bridged mode II delamination cracks," *Journal of the Mechanics and Physics of Solids*, vol. 47, no. 6, pp. 1265–1300, 1999. doi: 10.1016/S0022-5096(98)00107-0

[137] M. L. Falk, A. Needleman, and J. R. Rice, "A critical evaluation of cohesive zone models of dynamic fracture," *Journal de Physique IV*, vol. 11, no. PR5, pp. Pr5–43–Pr5–50, 2001. doi: 10.1051/jp4:2001506

[138] N. Moës and T. Belytschko, "Extended finite element method for cohesive crack growth," *Engineering Fracture Mechanics*, vol. 69, no. 7, pp. 813–833, 2002. doi: 10.1016/S0013-7944(01)00128-X

[139] A. Turon, C. G. Dávila, P. P. Camanho, and J. Costa, "An engineering solution for mesh size effects in the simulation of delamination using cohesive zone models," *Engineering Fracture Mechanics*, vol. 74, pp. 1665–1682, 2007. doi: 10.1016/j.engfracmech.2006.08.025

[140] P. M. Daniel, J. Främby, M. Fagerström, and P. Maimí, "An efficient ERR-cohesive method for the modelling of delamination propagation with large elements," *Composites Part A: Applied Science and Manufacturing*, vol. 167, p. 107423, 2023. doi: 10.1016/j.compositesa.2022.107423

[141] ASTM International, "Standard test method for mode I interlaminar fracture toughness of unidirectional fiber-reinforced polymer matrix composites," 2013.

[142] ——, "Standard test method for open-hole compressive strength of polymer matrix composite laminates," 2014.

[143] A. Møberg, M. K. Budzik, and H. M. Jensen, "Growth from initial to self-similar shape of an interface crack front," *International Journal of Adhesion and Adhesives*, vol. 83, pp. 59–68, 2018. doi: 10.1016/j.ijadhadh.2018.02.013

[144] B. Justusson, M. Molitor, J. Schaefer, S. L. Liguore, V. Ranatunga, and M. Pigazzini, "The use of LS-DYNA MAT299 for accurate prediction of impact damage in composite structures," in *AIAA Scitech 2021 Forum*, 2021. doi: 10.2514/6.2021-1624

[145] S. J. DeTeresa, L. M. Allison, B. J. Cunningham, D. C. Freeman, M. D. Saculla, R. J. Sanchez, and S. W. Winchester, "Experimental results in support of simulating progressive crush in carbon-fiber textile composites," 2001.

[146] J. Schön, "Coefficient of friction of composite delamination surfaces," *Wear*, vol. 237, pp. 77–89, 2000. doi: 10.1016/S0043-1648(99)00315-4

[147] D. M. Thomson, B. Erice, H. Cui, J. Hoffmann, J. Wiegand, and N. Petrinic, "A Puck-based localisation plane theory for rate- and pressure-dependent constitutive modelling of unidirectional fibre-reinforced polymers," *Composite Structures*, vol. 184, pp. 299–305, 2018. doi: 10.1016/j.compstruct.2017.09.088

[148] C. Pohl, "Übersicht Materialkennwerte LuFo-Projekt CraCpit," 2022.

[149] S. Butterworth, "On the theory of filter amplifiers," *Experimental Wireless & the Wireless Engineer*, pp. 536–541, 1930. [Online]. Available: https://www.changpuak.ch/electronics/downloads/on_the_theory_of_filter_amplifiers.pdf

[150] Z. Suo, G. Bao, B. Fan, and T. C. Wang, "Orthotropy rescaling and implications for fracture in composites," *International Journal of Solids and Structures*, vol. 28, no. 2, pp. 235–248, 1991. doi: 10.1016/0020-7683(91)90208-w

[151] ASTM International, "Test method for compressive properties of polymer matrix composite materials using a combined loading compression (CLC) test fixture," West Conshohocken, PA, 2009.

A Appendix

A.1 Adaption of crack opening mode I intralaminar fracture toughness values

The mode I energy release rate G_{I} for a composite is given as follows [150]:

$$G_I = \frac{1}{E} \cdot \sqrt{\frac{1+\rho}{2}} \cdot K_I^2 \tag{A-1}$$

where E is the laminate Young's modulus, ρ is a dimensionless elastic parameter, and K_{I} is the mode I stress intensity factor depending on the geometry. Kuhn et al. [115] determined laminate Young's moduli for their $(0/90)_{8s}$ layup using unnotched compressive specimens. They reported values of 67,449 MPa (QS) and 67,126 MPa (HR). However, the Young's modulus can also be determined from the literature values for $E_{11,\mathrm{C}}$ and $E_{22,\mathrm{C}}$ applying the rule of mixture. This approach yields values of about 81,589 MPa (QS) and 82,253 MPa (HR), which are 20% higher than the ones reported by Kuhn et al. The deviation between the value sets can be attributed to fiber misalignments in the compression specimens. Since the literature values appear more reliable, the $G_{11\mathrm{c,C}}$ FTs were recalculated and provided reduced values of 83.9 N/mm (QS) and 135.1 N/mm (HR).

A.2 Analytical buckling evaluation of OHC specimens

Specimens with a thickness of 2 mm, width of 9 mm, and unsupported length of 9 mm were used based on ASTM D6484/D6484M [122]. Bessa's results facilitated a buckling evaluation [123]: Linearly extrapolating his open-hole strengths, the quasi-static OHC strength $S_{\mathrm{OHC,QS}}$ was estimated by 388.2 MPa. The dynamic OHC strength $S_{\mathrm{OHC,HR}}$ at 100 1/s was extrapolated with Equation 3-2, yielding 514.8 MPa. The bending modulus $E_{\mathrm{QI,B,QS}}$ for a QI layup was estimated as balanced linear combination of the compressive and tensile modulus via the Classical Laminate Theory. For QS loading, a modulus of 66,622 MPa was determined from the values in Table 3-1. Again the values were also dynamically extrapolated where necessary using Equation 3-1 and providing a flexural modulus $E_{\mathrm{QI,B,HR}}$ of 67,179 MPa at 100 1/s. Buckling criticality was evaluated with the criterion from ASTM D6641/D6641M [151]:

$$t_{lam} \geq \frac{l}{0.9069 \cdot \sqrt{(1 - \frac{1.2 \cdot S_{OHC}}{G_{23}}) \cdot \frac{E_{QI,B}}{S_{OHC}}}} \tag{A-2}$$

The shear modulus G_{23} was conservatively preferred to shear modulus G_{13} and assumed SR-insensitive. Finally, for both strain rate regimes, the selected laminate thickness t_{lam} of 2 mm could be declared uncritical to buckling with required minimal laminate thicknesses of 0.82 mm (QS) and 0.98 mm (HR).

A.3 Design of coupon crushing specimens

A preliminary coupon design study was conducted with early-stage SLMs to evaluate the buckling risk and the crushing response of different specimen concepts. Also, the free crushing length after the trigger end should be maximized. A bevel trigger (BT) and the triangular through-thickness triggers (TTT) were investigated along with different specimen lengths and TTT trigger angles (cf. Figure 4-2a). Figure A-1a shows the stress-displacement curves of the simulations. Furthermore, Figure A-1b shows the BT model. Due to the early-phase rectangular mesh, the model responses are noisy during the initiation phase. Still, it can be seen that the TTT model with a trigger angle of 20° and specimen length of 10 mm provided the most stable force level without a buckling tendency. Therefore, this setup was selected as geometry for all further investigations.

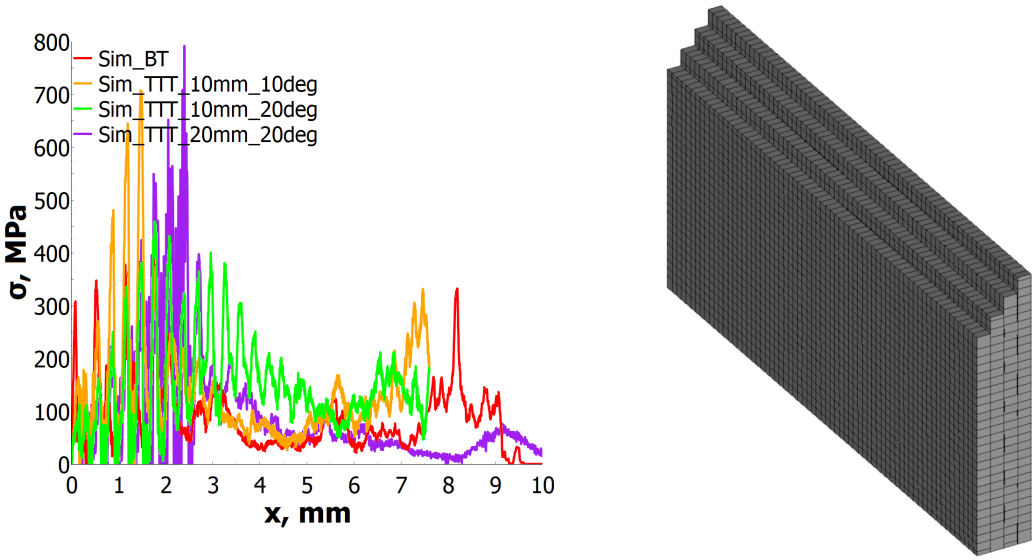

(a) **(b)**

Fig. A-1 (a) Stress-displacement diagram of coupon crushing pre-study with varying triggers, specimen lengths and trigger angles. (b) Isometric view of BT model.

A.4 Technical drawings of coupon fixture with force transducer

The fixture for the coupon specimens including a force transducer was designed in close cooperation with the Impact Engineering Laboratory of University of Oxford. As can be seen in Figure A-2, the fixture comprises a Kistler 9343A load cell, that is mounted on a base plate with an adapter bolt. A clamp is used to fixate the specimen not shown in the drawing. Also, the force transducer is protected against bending and overloading by a support guide and two sliders.

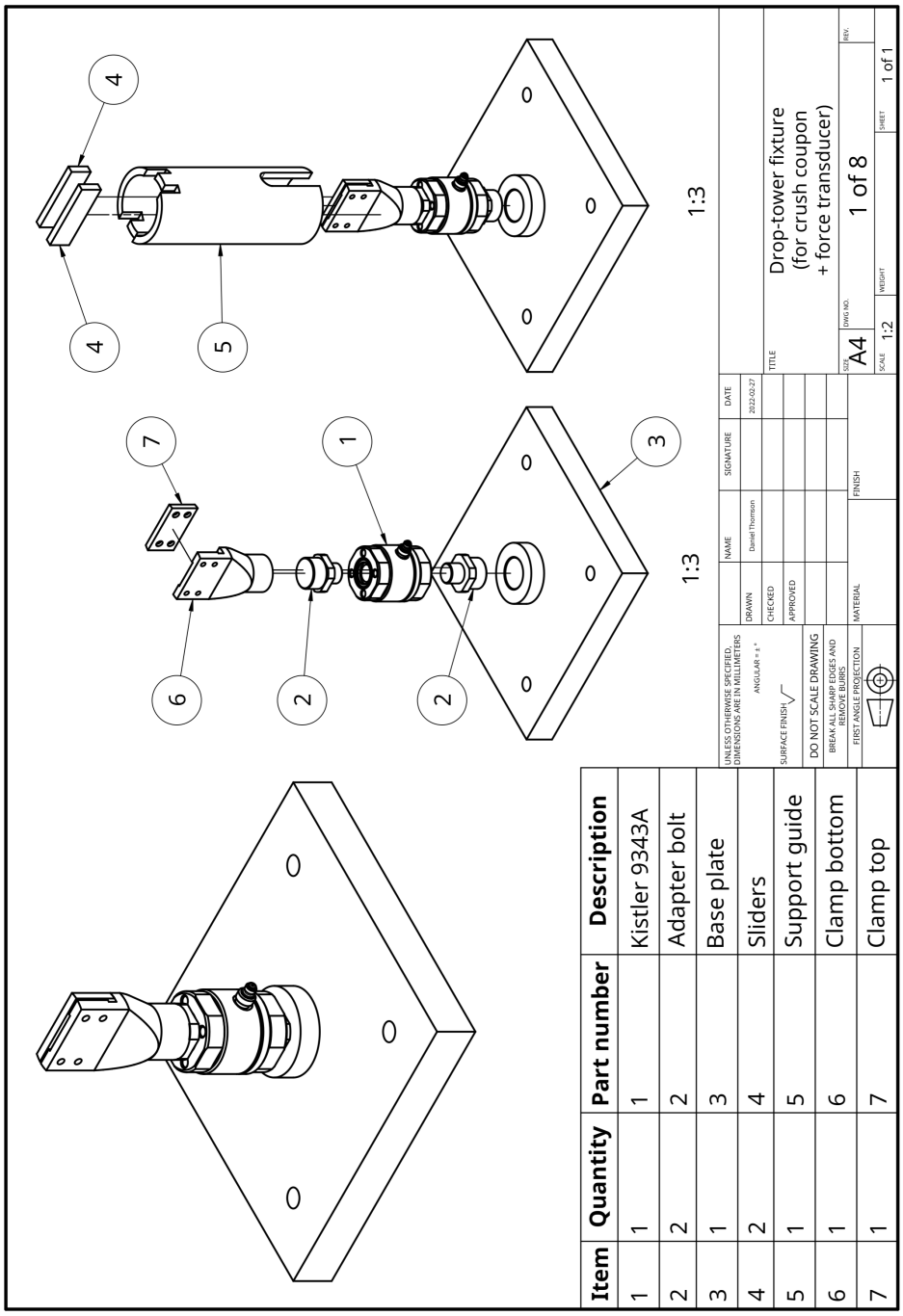

Fig. A-2 Exploded drawing of the experimental fixture, including the force transducer.

A.5 Exemplary IM7/8552 material cards

Figure A-1 provides an exemplary IM7/8552 *MAT_058 QS material card for 2 mm element size without curve definitions.

```
*MAT_LAMINATED_COMPOSITE_FABRIC_TITLE
MAT_058_IM7_8552_2mm_QS
$#     mid        ro        ea        eb      (ec)      prba      tau1    gamma1
         1   1.57E-9    154486      8930       0.0     0.019      80.0         0
$#     gab       gbc       gca    slimt1    slimc1    slimt2    slimc2     slims
      5068      2977      5068     0.248     0.207      0.05      0.05       1.0
$#    aopt     tsize     erods      soft        fs      epsf      epsr      tsmd
       0.0       0.0      -0.2       1.0      -1.0       0.0       0.0       0.9
$#      xp        yp        zp        a1        a2        a3      prca      prcb
       0.0       0.0       0.0       0.0       0.0       0.0     0.019       0.5
$#      v1        v2        v3        d1        d2        d3      beta
       0.0       0.0       0.0       0.0       0.0       0.0       0.0
$#    e11c      e11t      e22c      e22t       gms
         0         0         0         0    0.0447
$#      xc        xt        yc        yt        sc
      1454      2724       255        62      99.9
$#    lcxc      lcxt      lcyc      lcyt      lcsc     lctau     lcgam        dt
         0         0         0         0         0         0         0         0
$#  lce11c    lce11t    lce22c    lce22t     lcgms     lcefs
         0         0         0         0         0         0
```

Fig. A-1 QS *MAT_058 material card of IM7/8552 for 2 mm element size as LS-DYNA Ascii input.

Figure A-2 provides an exemplary material card for the CZM implementation of IM7/8552 with *MAT_240, 2 mm element size, and in the QS domain. The interlaminar strength properties T_0 and S_0 correspond to $S_{33,\mathrm{T,QS}}$ and $S_{13,\mathrm{QS}}$, whereas $G_{1\mathrm{C\_0}}$ and $G_{2\mathrm{C\_0}}$ correspond to $G_{33\mathrm{c,T,QS}}$ and $G_{13\mathrm{c,QS}}$, respectively.

```
*MAT_COHESIVE_MIXED_MODE_ELASTOPLASTIC_RATE_TITLE
MAT_240_IM7_8552_2mm_QS
$#     mid        ro     roflg   intfail      emod      gmod     thick    inicrt
         2   1.57E-9       0.0        1.     8691.     2977.         0         0
$#   g1c_0   g1c_inf   edot_g1        t0        t1    edot_t       fg1     lcg1c
      0.28       0.0       0.0         7       0.0       0.0       0.0         0
$#   g2c_0   g2c_inf   edot_g2        s0        s1    edot_s       fg2     lcg2c
       1.6       0.0       0.0      95.8       0.0       0.0       0.0         0
```

Fig. A-2 QS implementation of *MAT_240 material card of IM7/8552 for 2 mm element size as LS-DYNA Ascii input.

Figure A-3 provides an exemplary material card for the CZM implementation of IM7/8552 with TIEBREAK contact, 2 mm element size, and in the QS domain.

Figure A-4 provides an exemplary material card for the CZM implementation of IM7/8552 with *MAT_240, 2 mm element size, and in the HR domain.

```
*CONTACT_AUTOMATIC_ONE_WAY_SURFACE_TO_SURFACE_TIEBREAK_ID
$       id                                                                  name
3         TIEBREAK_IM7_8552_2mm_QS
$     ssid      msid     stype    mstype    sboxid    mboxid       spr       mpr
          1         2         3         3         0         0         1         0
$       fs        fd        dc        vc       vdc    penchk        bt        dt
        0.        0.        0.        0.       20.         0        0.     1.E20
$      sfs       sfm       sst       mst      sfst      sfmt       fsf       vsf
        1.        1.     0.585     0.585        1.        1.        1.        1.
$   option      nfls      sfls     param    eraten    erates     ct2cn        cn
         14       0.0       0.0       0.0        0.        0.        0.        0.
$    g1c_0   g1c_inf   edot_g1        t0        t1    edot_t       fg1     lcg1c
      0.28       0.0       0.0         7        0.        0.       0.0         0
$    g2c_0   g2c_inf   edot_g2        s0        s1    edot_s       fg2     lcg2c
       1.6       0.0       0.0      95.8        0.        0.       0.0         0
```

Fig. A-3 QS implementation of a TIEBREAK contact definition of IM7/8552 for 2 mm element size and shell distance of 0.5 mm as LS-DYNA Ascii input.

```
*MAT_COHESIVE_MIXED_MODE_ELASTOPLASTIC_RATE_TITLE
MAT_240_IM7_8552_2mm_HR
$#     mid        ro     roflg   intfail      emod      gmod     thick    inicrt
         2   1.57E-9       0.0        1.     8691.     2977.         0         0
$#   g1c_0   g1c_inf   edot_g1        t0        t1    edot_t       fg1     lcg1c
     0.201       0.0       0.0        -7     0.103     2.174       0.0         0
$#   g2c_0   g2c_inf   edot_g2        s0        s1    edot_s       fg2     lcg2c
     0.773       0.0       0.0     -95.8     1.408     2.174       0.0         0
```

Fig. A-4 HR implementation of *MAT_240 material card of IM7/8552 for 2 mm element size as LS-DYNA Ascii input.

A.6 Composite Materials Handbook-17 Crashworthiness Working Group simulation success criteria

The simulation quality criteria defined by the CMH-17 CWG were adopted and combined with a traffic-light color code [144]:

- Excellent: model deviates from the experimental average by less than 10%
- Good: model deviates from the experimental average within 10% to 15%
- Fair: model deviates from the experimental average within 15% to 20%
- Poor: model deviates from the experimental average by more than 20%

B Publications

As part of the research activities for this thesis, the following journal papers and conference contributions were published:

Peer-reviewed journal publications

[J1] C. Pohl, M. Toenjes, C. Liebold, M. Ploeckl, H. Koerber, L. Avila Gray, D. Colin, and K. Drechsler, "Numerical prediction of composite damage behavior: A modeling approach including the strain-rate-dependent material response," *Composite Structures*, vol. 292, p. 115628, 2022. doi: 10.1016/j.compstruct.2022.115628

[J2] C. Pohl, H. Liu, D. Thomson, L. Avila Gray, D. E. Sommer, and N. Petrinic, "Dynamic crushing of composite coupons: An experimental and numerical study," *Journal of Composite Materials*, vol. 57, no. 26, pp. 4103–4121, 2023. doi: 10.1177/00219983231201997

Conference publications

[C1] C. Pohl, "Numerical prediction of the crash behavior for composites," in *SAMPE Germany*, 2021.

[C2] C. Pohl, H. Liu, D. E. Sommer, D. Thomson, and N. Petrinic, "Comparison of different numerical modelling techniques to evaluate high-speed crushing behaviour of fibre-reinforced composites," in *18th European Mechanics of Materials Conference*, 2022.

[C3] C. Pohl, M. Hofmann, S. Schmauss, and J. Loewe, "Numerical validation of a sailplane fuselage crash test," in *16th LS-DYNA Forum*, 2022.

[C4] C. Pohl, "Forschung an Sicherheitscockpits für Kleinflugzeuge," in *9. Fachkongress Composite Simulation*, 2022.

Invited seminar presentation

[P1] C. Pohl, M. Hofmann, S. Schmauss, and J. Loewe, "Validierung der Crashsimulation eines Segelflugzeugrumpfes in LS-DYNA," Ulm, November 10 2022.

C Supervised student theses

During my employment at the TUM-LCC, I supervised or co-supervised the following student theses:

Bachelor's theses

[B1] C. Kudla, "Auslegung und Detailkonstruktion des Rumpfes des Hochleistungs-Segelkunstflugzeugs Mü32," Bachelor's thesis, Technical University of Munich, Munich, 2019.

[B2] J. A. Gallego Diosa, "Integration des crashrelevanten Crushing-Verhaltens von Composites in bestehende LS-Dyna-Materialkarten," Bachelor's thesis, Technical University of Munich, Munich, 2019.

[B3] M. Hofmann, "Auslegung und Optimierung einer CFK-Felge für ein Formula Student Fahrzeug," Bachelor's thesis, Technical University of Munich, Munich, 2019.

[B4] M. Korn, "Optimierung von Sandwichkernmaterialien aus gelofteten rCF-Vliesstoffen," Bachelor's thesis, Technical University of Munich, Fraunhofer IGCV, Munich, 2019.

[B5] F. Kargl, "Modellaufbau einer Segelflugzeug-Rumpfstruktur zur FEM-Simulation in LS-DYNA," Bachelor's thesis, Technical University of Munich, Munich, 2019.

[B6] E. S. Hartoyo, "Konzeptioneller Vergleich zwischen 2D- und 2½D-Ablage mit Randfixierung für die Herstellung von endlosfaserverstärkten thermoplastischen Stacks," Bachelor's thesis, Technical University of Munich, Fraunhofer IGCV, Munich, 2019.

[B7] T. Pieper, "Literaturrecherche zum Ermüdungsverhalten von Faserverbundstrukturen unter mechanischer Belastung," Bachelor's thesis, Technical University of Munich, Munich, 2020.

[B8] J. Loewe, "Konzeptionierung eines Crashtests an einer Segelflugzeugrumpfstruktur," Bachelor's thesis, Technical University of Munich, Munich, 2021.

[B9] R. Michaelis, "Charakterisierung und Simulation des Delaminationsverhaltens von Composites zur Verbesserung der Schädigungsprognose unter Crashbelastung," Bachelor's thesis, Technical University of Munich, Munich, 2021.

[B10] M. Koenigbaur, "Validierung von Composite Materialkarten unter der Verwendung von 3-Punkt-Biege- und Crushingversuchen," Bachelor's thesis, Technical University of Munich, Munich, 2022.

Semester theses

[S1] J. Hoffelner, "Recherche zur Belastbarkeit des Menschen unter Crashlastfällen und Ableitung von Sicherheitsanforderungen an eine Segelflugzeug-Rumpfstruktur," Semester thesis, Technical University of Munich, Munich, 2019.

[S2] K. Kossarev, "Vergleichende Untersuchung von LS-DYNA-Materialmodellen für die Modellierung von Composite-Werkstoffen unter Crash-Belastung," Semester thesis, Technical University of Munich, Munich, 2019.

[S3] S. Mazaduryan, "Untersuchung von Materialmodellen für Metalle und Schäume zur Crash-Simulation in LS-DYNA," Semester thesis, Technical University of Munich, Munich, 2019.

[S4] M. Toenjes, "Konzeptionierung und FEM-Simulation einer Prinzipgeometrie zur Validierung von Faserverbund- und Adhäsivmaterialkarten," Semester thesis, Technical University of Munich, Munich, 2019.

[S5] C. Lange, "Virtuelle Bewertung von Lastfallszenarien an einer Segelflugzeug-Rumpfstruktur in LS-DYNA," Semester thesis, Technical University of Munich, Munich, 2020.

[S6] M. Korn, "Thermoplastische Reaktiv-Pultrusion von Hybrid-Profilstrukturen," Semester thesis, Technical University of Munich, Fraunhofer IGCV, Munich, 2020.

[S7] M. Hofmann, "Modellierung und FEM-Simulation des Crashs einer Segelflugzeug-Rumpfstruktur in LS-DYNA," Semester thesis, Technical University of Munich, Munich, 2021.

[S8] A. Ravindranatha, "Passive safety in gliders: virtual integration and analysis of a dummy model under crash impact," Semester thesis, Rosenheim University of Applied Sciences, Technical University of Munich, Munich, 2021.

[S9] T. Pieper, "Erweiterung und Validierung von Faserverbund-Materialkarten zur simulativen Beschreibung des Crushingverhaltens," Semester thesis, Technical University of Munich, Munich, 2021.

Master's theses

[M1] C. Cornejo Runge, "Experimentelle und simulative Bestimmung der Open-Hole-Festigkeiten von UD-Carbon-Epoxy Composite Laminaten bei statischer und hochdynamischer Belastungsgeschwindigkeit," Master's thesis, Technical University of Munich, Munich, 2018.

[M2] M. H. Izzudin Al Mudzakir, “A comparative assessment of different cohesive zone models for crashworthiness evaluation in LS-Dyna,” Master’s thesis, Technical University of Munich, Munich, 2019.

[M3] S. Norouzi, “Evaluation of strain-rate-dependent shear behavior of fiber-reinforced composite materials,” Master’s thesis, Technical University of Munich, Munich, 2019.

[M4] M. Toenjes, “Konzeptionierung und Optimierung einer Fahrzeugseiten-schwellerstruktur in Faserverbundbauweise mittels FE-Simulation,” Master’s thesis, Technical University of Munich, EDAG Engineering GmbH, Munich, 2020.

[M5] K. Jeberien, “Entwicklung und FEM-gestützte Optimierung eines Energieab-sorberkonzepts für Segelflugzeuge zur Steigerung der Unfalltauglichkeit,” Master’s thesis, Technical University of Munich, Munich, 2021.

[M6] M. Korn, “Entwicklung eines Werkzeugkonzeptes für die Schmelzpultrusion von aramidvliesverstärkten Thermoplastprofilen,” Master’s thesis, Technical University of Munich, Fraunhofer IGCV, Munich, 2021.

[M7] C. Lange, “Numerische Untersuchung eines neuartigen Materials für Penetra-torgefechtsköpfe im Überschallbereich,” Master’s thesis, Technical University of Munich, TDW GmbH, Munich, 2021.

[M8] C. Fabry, “Aufbau und Validierung eines FEM-Modells einer Hubschrauber-sitzschale aus Verbundwerkstoffen nach dem Building-Block-Approach,” Mas-ter’s thesis, Technical University of Munich, B/E Aerospace Fischer GmbH, Munich, 2022.

[M9] M. Hofmann, “Validierung des Finite-Elemente-Modells eines Segelflugzeugs an einem Gesamtstruktur-Crashtest,” Master’s thesis, Technical University of Munich, Munich, 2022.

[M10] T. Pieper, “Erweiterung und Evaluation eines Betriebsfestigkeitskonzepts für die simulative Lebensdauerbewertung von Faser-Kunststoff-Verbunden,” Master’s thesis, Technical University of Munich, IABG mbH, Munich, 2023.

Parts of the following theses contributed to the present doctoral thesis: [B1, B2], [B5], [B8 - B10], [S1 - S5], [S7 - S9], [M1, M2], [M4, M5], [M9].